Instabilities in the flow over a spinning disk at angle of attack

Thesis by
Marcus Kuok Kuan Lee

In Partial Fulfillment of the Requirements for the
Degree of
Doctorate of Philosophy

CALIFORNIA INSTITUTE OF TECHNOLOGY
Pasadena, California

2022
Defended August 17th, 2021

Marcus Kuok Kuan Lee
ORCID: 0000-0003-3972-843X

ACKNOWLEDGEMENTS

Throughout my graduate school journey, I have grown a lot both inside and outside of research, all thanks to the many incredible people that I have met along the way. I could not imagine the past several years without their support, guidance, and friendship.

First of all, I would like to thank my advisors, *Tim Colonius* and *Beverley McKeon*. I am incredibly lucky to have not just one, but two amazing advisors who have supported me through many challenges and continue to inspire me both intellectually and personally. Tim, thank you for your unconditional support and kindness over the years. I am grateful that you challenged my ideas and made sure they held up to the toughest criticism. Thank you for humoring me with my many questions on writing, teaching and DEI as well. Your thoughtfulness and insight extend endlessly, and I am grateful that you shared that with me. While you have helped me grow a lot over the past six years, you have also shown me new horizons I have yet to reach and left me with a burning desire to continue improving myself. Beverley, thank you for your compassionate mentorship and guidance. I always leave our meetings with so many new questions to answer, but also feeling more confident in approaching them. You are a phenomenal role model both in research and beyond. I have learnt a lot from your thoughtful teaching methods and your perspective on DEI work. I know your methods and teachings will continue to inform how I approach new challenges.

I would also like to thank my committee members, *Guillaume Blanquart* and *Mory Gharib*. Guillaume, thank you for always bringing a smile to my face when we run into each other in Gates-Thomas. I am grateful for your questions and insight both in and outside of research that always help push the limits of my imagination. Professor Gharib, thank you for your time serving on my thesis committee. I am always excited to hear about the research from your group, and I am honored to be able to share my research with you and have your insights into my work.

I would like to thank the Computational Flow Physics Group members who I shared my graduate school experience with and made for a fun and lively group: *Oliver Schmidt*, *George Rigas*, *Gianmarco Mengaldo*, *Kevin Schmidmayer*, *Benedikt Dorschner*, *Lennart Schneiders*, *Mauro Rodriguez*, *Spencer Bryngelson*, *Shunxiang Cao*, *Sebastian Liska*, *Andres Goza*, *Kazuki Maeda*, *Phillipe Tosi*, *André da Silva*, *Ke Yu*, *Ethan Pickering*, *Jean-Sebastian Spratt*, *Ben Steven*s, *Kyle Cook*, *Liam Heidt*,

Omar Kamal, *Wei Hou*, *Qifan Wu*, and *José Chreim*. I am particularly grateful to Sebastian, who wrote the incredible IBLGF code that I use in this thesis. Thank you as well to Ke, for the fun times working on IBLGF together. Finally, thank you to Benedikt for your patient mentorship.

I am grateful to the many friends I have met both at Caltech and beyond, who have given me cherished memories. I am especially grateful for *Karena Cai*, *Richard Cheng*, *Zoila Jurado*, *Hyeongchan Jo*, and *Linus Eng* for the countless meals and philosophical conversations. I also could not have imagined a better MCE cohort with whom to share many fun times both inside and outside of Gates-Thomas. I am incredibly grateful to *Jonathan Nguyen*, *Oscar Ngo*, *Nada Hin*, *Leighton Whee*, *Leon Anh*, *Soe Thein*, *Jake Vo*, *Robi Bucayo*, *Austin Wang*, and *Jeff Chen*, for the many meals and trips we have shared. Thanks for bringing me out of my Caltech bubble! *Tori Lee*, thanks for sharing your unyielding passion for helping others and teaching me how to do the same. *Matt Diep*, thank you for always knowing the right words to say to cheer me up, inspiring me to grow as a person, and for the many Zoom work sessions that helped keep me going. *Peter Run*, thanks for being my running buddy and keeping me grounded. *Allan Kwok*, *Kha Ly*, and *Wesley Yiin*, thanks for the many meaningful conversations and laughter. I would also like to thank my fellow Malaysians at Caltech, *Yoke Peng Leong*, *Voon Lai*, *Cynthia Chai*, *Ying Shi Teh*, *Linus Eng,* and *Shu Fay Ung*, who gave me a home away from home and with whom I have enjoyed many cooking adventures and board game nights. Thank you, *Brooks Fu*, for taking me to eat great food in SGV and helping me to navigate grad school. Thanks to *Kuo Lee*, *Aiko Hualda*, *Josh Lee*, *Sumaytee Kasemchit*, *Dat Ho*, and *Steven Kuoch* for helping me to explore LA and beyond! I am also grateful for my friends and "Frands" from Princeton, *Jean Choi*, *Li Ting Ooi*, *Rishita Patlolla*, *Sunny Patel*, *Will Tso*, *Yolanda Yeh*, *Yuem Park*, *Jessica Liang*, and *Briana Liu*, whose continued friendship has been a great source of strength, even before my Caltech journey.

There are many staff at Caltech that make it such an amazing place. I would like to thank *Holly Golcher*, *Mikaela Laite*, and *Lynn Seymour* for supporting the research group and MCE, and always making sure everything went smoothly. It has been such a pleasure to work with each of you, and those experiences have taught me much about planning events, budgeting, and general organization. I don't know what I or the department would do without you. I would also like to thank *Jenn Weaver* and *Cassandra Horii* at the CTLO, who helped me discover my passion

for teaching. Thank you to *Hanna Song*, *Erin-Kate Escobar*, *Taso Dimitriadis*, and *Monique Thomas* at the CCID for creating such a welcoming and informative space on campus. Thank you to *Grace Ho* and *Denise Lin* for your many words of wisdom. I have learnt so much from you that I will continue to carry with me moving forward!

Last but not least, I would like to thank my family: *Mummy*, *Daddy*, *Jie Jie*, and *Karan Shah*. Although we are oceans apart, I can always share my achievements and struggles with you. You have always believed in me and provided your unconditional support. My ability to persevere is in large part thanks to you.

ABSTRACT

Micro air vehicles (MAVs) face stability issues, especially as they continue to decrease in size. A spinning disk is inherently robust to external disturbances due to its spin stabilization, and therefore is a potential design for stable MAV flight. However, controlled flight of a spinning disk requires a detailed understanding of the underlying flow structures that determine the aerodynamic behavior. A spinning disk acts to rotate and propel nearby flow tangentially outwards, while drawing in fluid from above. In this way, spin acts as an additional source of both angular and linear momentum from the disk's surface, which can alter the wake structure significantly. In this thesis, we explore how spin affects the aerodynamic forces on a disk and characterize several instabilities that occur. To this end, we use the immersed-boundary Lattice Green's function (IBLGF) method to simulate flow over a spinning disk at angle of attack for Reynolds numbers of $O(10^2)$ and tip-speed ratios (non-dimensional spin rate) up to 3.

At these Reynolds numbers, the steady flow first undergoes a bifurcation associated with wake instability, giving rise to vortex shedding. Increasing tip-speed ratio leads to monotonic increases in both lift and drag, although the lift-to-drag ratio remains fairly constant. We also identify several distinct wake regimes, including a region of vortex-shedding suppression, and the appearance of a distinct corkscrew-like short-wavelength instability in the advancing tip vortex. To understand the mechanism leading to suppression of vortex shedding, we study the streamlines and vortex lines in the wake. We show that the vorticity produced by the spinning disk strengthens the tip vortices, inducing a spanwise flow in the trailing edge vortex sheet. This helps to dissipate the vorticity, which in turn prevents roll up and thus suppresses vortex shedding. For the short-wavelength instability, we use spectral proper orthogonal decomposition (SPOD) to identify the most energetic modes and compare it to elliptic instabilities seen in counter-rotating vortex pairs with axial flow. The addition of vorticity from the disk rotation significantly alters the circulation and axial velocity in the tip vortices, giving rise to elliptic instability despite its absence in the non-spinning case. We also observe lock-in between the frequency of the elliptic instability and twice the spin frequency, indicating that disk rotation acts as an additional forcing for the elliptic instability. Many of these phenomena are consistent with observations in high Reynolds number studies and for other bluff body geometries. As a result, the mechanisms proposed here may

serve as a basis for understanding and predicting the changing wake structures in more complex flow configurations.

TABLE OF CONTENTS

LIST OF ILLUSTRATIONS

Number *Page*

LIST OF TABLES

Number *Page*

Chapter 1

INTRODUCTION

1.1 Motivation: Spinning disks as micro air vehicles

Micro air vehicles (MAVs) face stability issues in the presence of gusty winds, especially as their size is scaled down (Pines and Bohorquez, 2006). Several authors have studied spinning-disk flight and suggested its application to MAV design (Potts and Crowther, 2002; Lorenz, 2007; Stilley and Carstens, 1972). An example of spinning disks is the recreational Frisbee, which leverages spin-stabilization to achieve robust flight when subject to environmental disturbances (Potts and Crowther, 2002). In addition to the spin dynamics, a spinning disk in an otherwise quiescent fluid rotates and propels fluid outward near the disk surface, drawing in fluid towards the disk surface from above, creating a swirling flow towards the disk. This means that the disk injects both linear and angular momentum into the flow, modulating properties in the wake. Beyond spinning disk flight applications, wall-flush-mounted rotating disks (Ricco and Hahn, 2013) and rotating rings (Olivucci, Ricco, and Aghdam, 2019) in turbulent channel-flow configurations can reduce drag by up to 20%. Munday and Taira (2018) applied a similar concept using swirling jets, which also inject linear and angular momentum into the flow, to suppress flow separation. These provide examples where rotating disks can potentially be used in flow control.

However, applications in flight and flow control require a thorough understanding of the effect that spin has on the spinning-disk aerodynamics, instabilities and wake structures. Despite these applications, flows over spinning disks have not been thoroughly investigated, perhaps owing to the large parameter space spanned by three main non-dimensional parameters: Reynolds number, Re, angle of attack, α and tip-speed ratio (TSR), λ. We define the Reynolds number as

$$Re = \frac{\rho U D}{\mu}, \tag{1.1}$$

where ρ is the fluid density, U is the freestream velocity, D is the disk diameter, and μ is the dynamic viscosity. The tip-speed ratio (TSR) is the ratio between the disk-edge velocity and the freestream velocity, and can be written as

$$\lambda = \frac{\Omega R}{U}, \tag{1.2}$$

where Ω is the disk angular velocity around its axis of rotational symmetry, and R is the disk radius. Further parameters are associated with the disk's cross section including an aspect ratio $\chi = D/t_d$, where t_d is the thickness, for the case of a rectangular cross section; camber, for a curved disk (e.g. a Frisbee); and edge shape/rim. We can also define a rotational Reynolds number $Re_omega = \rho\omega RD/\mu = \lambda Re$ using the disk edge velocity instead of the incoming flow velocity. This measure of rotation remains valid for $U = 0$, unlike λ. Note that for the simulations in this thesis, we model the disk as an infinitely-thin disk using a single layer of immersed boundary points, with some caveats that are discussed in section 2.3.5. Each of these parameters acts as a bifurcation parameter in the flow, leading to a complex and multi-dimensional space of flow regimes. The flow configuration and parameters are depicted schematically in figure 1.1.

In this study, we focus on $Re = O(10^2)$, where the flow initially bifurcates. While this regime is not typically reached even for the smallest MAV, instabilities clearly identified in this regime may persist to high Reynolds number, albeit modulated by further bifurcations and ultimately the emergence of turbulence. Such behavior is common to many bluff-body and aerodynamic flows, for example the vortex shedding first occurring in two-dimensional flow over a bluff body at $Re \approx 50$ persists in this way as $Re \to \infty$. In addition, as a canonical flow, a spinning disk at these low Re may be applicable to other applications, for example as wall-flush-mounted actuators flow drag reduction as mentioned above (Ricco and Hahn, 2013; Olivucci, Ricco, and Aghdam, 2019). Although these observations are made for turbulent flows at much higher Reynolds numbers than those considered in this study, some of the large-scale flow features share similarities, including the induced wall-normal flow towards the rotating disk and the outward radial flow near the disk surface (Olivucci, Ricco, and Aghdam, 2019). The ability of the rotating disk to inject linear and angular momentum into the flow with a net-zero mass flux may be desirable for flow-control applications, as this allows for the generation of a various distributions of spanwise and streamwise velocity perturbations when using multiple rotating disks (Keefe, 1997; Keefe, 1998).

1.2 Experimental studies of flow over Frisbee-like spinning disks

Past studies of spinning-disk flight at angle of attack consist of experimental studies of Frisbee-like geometries with camber and rims, performed at $Re = O(10^5)$ to match realistic Frisbee-flight Reynolds numbers. Potts and Crowther (2001; 2002) experimentally investigated spinning-disk flight at $Re = O(10^5)$, $-10° < \alpha < 30°$

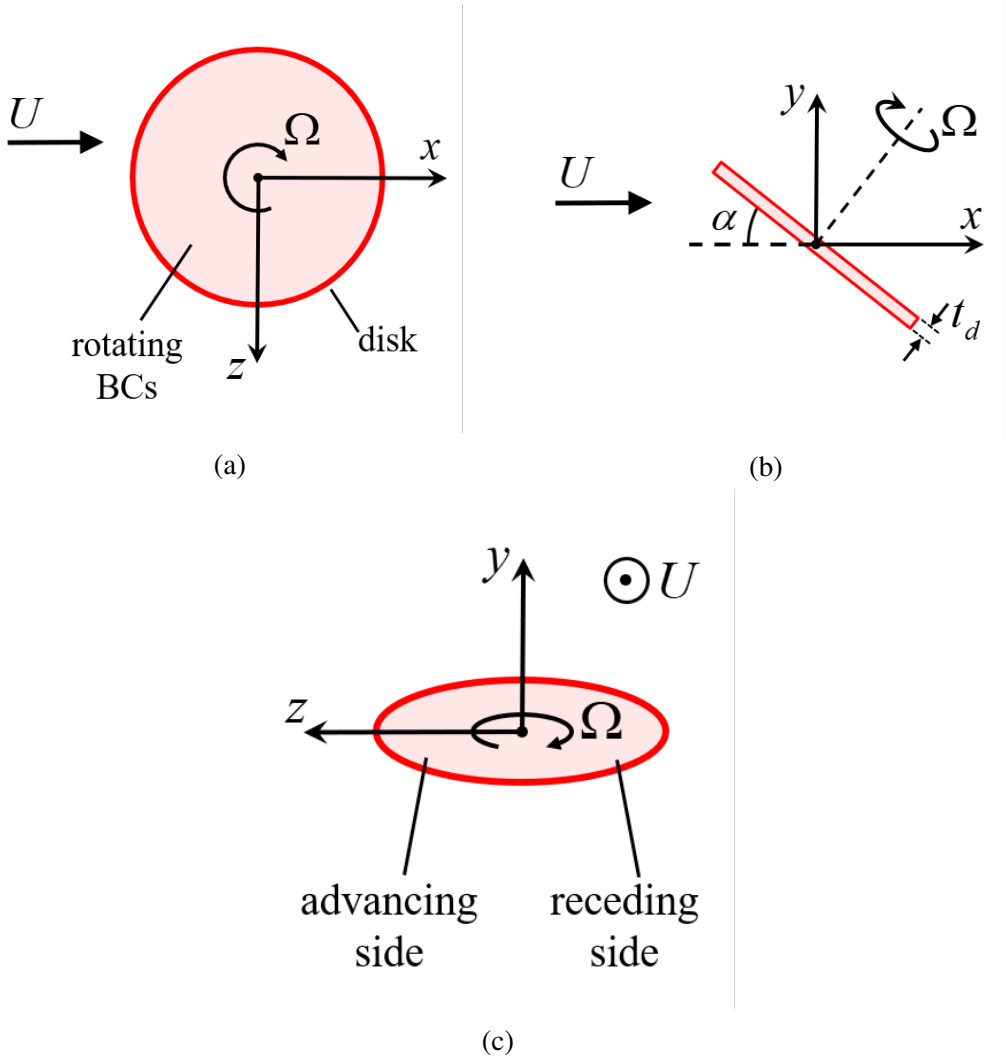

Figure 1.1: Schematic of setup for (a) top view, (b) side view and (c) upstream view. The freestream velocity, U, is in the positive x direction.

and $0 \leq \lambda \leq 1.04$, reporting various aerodynamic and moment coefficient data for a Frisbee-like geometry. They found a negligible effect of spin on lift and drag (2001), but found that spin has some effect on pitching moment, rolling moment and side force coefficients (2002). Early studies of thick cylindrical disks ($2 < \chi < 3$) by Stilley and Carstens (1972) similarly found that for $\lambda < 1$, spin has a negligible effect on lift and drag coefficients. Potts (2005) compared aerodynamic forces and moments for various Frisbee- and discus-like disk geometries. For TSRs above $\lambda = 1$ and up to $\lambda = 3.46$, Potts (2005) found that lift and drag could increase significantly across a broad range of angles of attack from $-10°$ to $\alpha = 30°$ ($\Delta C_L \approx 0.5$ and $\Delta C_D \approx 0.2$). Potts and Crowther (2002) include some aerodynamic data for the non-spinning flat disk against angle of attack, showing that lift and drag are lower

compared to Frisbees which have a rim. However, the lift-to-drag ratio has been shown to be higher for the flat disk compared to the Frisbee, motivating more investigation into rimless disks for flight purposes (Yasuda, 1999; Lorenz, 2007).

Some investigations into the wake structure at $Re = O(10^5)$ have also been performed. Higuchi et al. (2000) used PIV of flow over a cambered disk with a rim to determine the circulation in the tip vortices and found that spin ($\lambda = 0.8$) could both increase or decrease circulation depending on the angle of attack. Using smoke visualization of a Frisbee, Nakamura and Fukamachi (1991) observed that spin values of $\lambda = 2.26$ significantly strengthened the tip vortices and increased downwash in the wake, leading them to conclude that spin enhances lift. Overall these studies suggest limited to no effect on lift and drag for $\lambda < 1$, but potentially large increases for $\lambda > 1$.

Studies of inclined spinning disks have been restricted to high-Reynolds-number flows for cambered disks with rims, and have been limited in their ability to examine and visualize flow structures due to the complex, unsteady, 3D nature of the flow. As a result, it is still unclear how spin affects the vortical structures and instabilities present in wake, especially those originating as bifurcations at low Reynolds numbers. We turn to the more extensive literature on flow over non-spinning disks and spinning disks in quiescent flow to extract some helpful background on some of the expected flow regimes present for the combined spinning and translating disk.

1.3 Flow over non-spinning flat disks

The majority of studies on flow over disks have been conducted for flow normal to a non-spinning disk ($\alpha = 90°$). Several features of the resulting bifurcations with respect to Reynolds number persist for inclined flow as well. For flow normal to a thin disk ($\chi > 10$), Chrust, Bouchet, and Dusek (2010) summarize the different bifurcations and resulting flow stages. As Re increases, the six stages are (i) steady axisymmetric, (ii) steady planar-symmetric, (iii) periodic vortex shedding with non-zero mean lift and loss of reflectional symmetry, (iv) periodic shedding with zero-mean lift, (v) quasi-periodic shedding with a low frequency modulation, and (vi) chaotic. Disk thickness can affect critical numbers and slightly modify the intermediary stages (Meliga, Chomaz, and Sipp, 2009; Auguste, Fabre, and Magnaudet, 2010).

Calvert (1967) was the first to look at the inclined disk, investigating the periodicity of the vortex shedding. Frequency, pressure, and velocity in the wake measurements

were performed for $Re = O(10^4)$ while smoke visualization captured the vortex shedding at Reynolds numbers between 500 and 1,000. From there, experimental work by Humphries and Vincent (1976) for $2,000 < Re < 40,000$ studied the base pressure and circulation bubble length as a function of angle of attack.

More recent studies by Chrust, Dauteuille, et al. (2015), Tian et al. (2017) and Gao et al. (2018) closely examined the bifurcations for the inclined disk as angle of attack is varied. Increasing angle of attack leads to many similar flow stages as seen with normal flow, namely (i) steady planar-symmetric flow, (ii) periodic vortex shedding, (iii) quasi-periodic shedding with low-frequency modulation (PSL) and (iv) symmetry-breaking chaotic flow (Tian et al., 2017; Gao et al., 2018; Chrust, Dauteuille, et al., 2015). Inclination immediately breaks axisymmetry and gives a preferred alignment for vortex shedding (Chrust, Dauteuille, et al., 2015). The first bifurcation is a Hopf bifurcation that maintains spanwise-planar symmetry and transitions the flow from a steady state to a periodic wake with hairpin-vortex shedding from the trailing edge (Chrust, Dauteuille, et al., 2015). Chrust, Dauteuille, et al. (2015) mapped the critical Reynolds number of this Hopf bifurcation for $40° < \alpha < 90°$. Tian et al. (2017) identified further wake regimes that exist for different angles of attack at $Re = 500$. With increasing angle of attack, the flow transitions from steady, to periodic vortex shedding, to periodic with low-frequency modulation, to quasi-periodic, and finally to chaotic. The periodic state with low-frequency modulation (PSL) regime corresponds to a strengthening and weakening of the vortices shed from the disk, reflected in the growing and lessening amplitude of lift and pressure signals. Gao et al. (2018) conducted a thorough Re-α parameter study for $50 < Re < 300$ and $10° < \alpha < 90°$, mapping out the boundaries between these flow regimes. Overall, increasing angle of attack and increasing Reynolds number lead the flow from steady to the chaotic state, passing through different stages in the intermediate periodic states depending on the exact configuration (Tian et al., 2017; Gao et al., 2018).

Chrust, Dauteuille, et al. (2015) also compared the infinitely thin disk ($\chi = \infty$) to a case with a finite thickness ($\chi = 6$) and showed that for high angles of attack ($\alpha \gtrapprox 50°$), increased thickness delays the Hopf bifurcation to higher Reynolds numbers. However, this effect seems to reverse for low angles of attack ($\alpha \lessapprox 40°$), with thicker disks reducing the critical Reynolds number instead (Chrust, Dauteuille, et al., 2015; Gao et al., 2018).

Overall, these inclined disk studies are extensions of studies of the normal flow case

($\alpha = 90°$), and they focus primarily on high angles of attack ($\alpha \geq 30°$). While these studies serve as a good basis for comparison, for flight purposes, we are ultimately interested in lower angles of attack up to about 30° for optimal lift-to-drag ratio.

1.4 Spinning disks in quiescent flow

Flow over spinning disks in quiescent flow have been extensively studied, starting with von Kármán (1921), who developed a similarity solution for flow over an infinite spinning disk, with some corrections by Cochran (1934). The disk rotation propels fluid tangentially outward near the disk surface and thus pulls in fluid from above the disk to replace it. This results in a swirling downward flow towards the disk surface, which will play an important role in how the added linear and angular momentum interacts with the rest of the flow for the translating case. For sufficiently high TSRs, motion induced by spin dominates and the infinite disk solution represents a reasonable approximation over the finite disk despite edge effects, even when subjected to a parallel flow (aus der Wiesche, 2002). For more moderate TSRs, the infinite disk similarity solution can serve as a qualitative description of the flow for the finite disk.

1.5 Contributions and outline

In this thesis, we perform perform direct numerical simulations of the three-dimesional, incompressible Navier-Stokes equations to explore the flow regimes for the spinning disk at angle of attack. We vary TSR, Reynolds number, and angle of attack, and analyze the changing wake structure in an attempt to uncover the mechanisms leading to these bifurcations. We consider TSRs up to $\lambda = 3$, focusing on the Re and α parameter space around the first bifurcations from steady flow.

The numerical formulation used to simulate the flow is further detailed and validated in Chapter 2. In Chapter 3, we investigate the aerodynamic forces and wake structures as TSR is increased up to three and identify vortex-shedding suppression and a short-wavelength instability. In Chapter 4, we further explore the stabilizing effect of spin on the vortex-shedding instability, and use streamline and vortex line visualizations to understand the underlying mechanism. Next, in Chapter 5 we characterize the distinct short-wavelength instability that appears at higher tip speed ratios, and use spectral orthogonal decomposition (SPOD) to isolate the most energetic modes and compare them to elliptic instabilities. Finally, we summarize our findings and present ideas for future work in Chapter 6.

Chapter 2

COMPUTATIONAL METHODOLOGY AND SETUP

2.1 Governing equations and numerical method

To simulate flow over a spinning disk, we use the IBLGF (Immersed Boundary Lattice Green's Function) method to solve the 3D incompressible Navier-Stokes equations on a formally infinite domain (Liska and Colonius, 2017). The method utilizes a standard second-order staggered-mesh finite-volume scheme, which, owing to the unbounded domain, leads to a number of useful commutative properties that in turn lead to discrete conservation properties, provable stability, and an efficient solution algorithm. The no-slip boundary condition at the immersed boundary (IB) points is enforced implicitly at each step using a projection method. The associated Poisson equation is inverted, using the LGF, to predict the pressure in a finite, adaptive region defined by a source that is nonzero only where the vorticity is nonzero, which in practice means that it exceeds a certain user-defined threshold value, ϵ. Extensive details on the IBLGF formulation as well as extensive validation for grid resolution, Δx; temporal discretization, Δt; domain adaption threshold, ϵ; and IB point spacing, Δs, are given by Liska and Colonius (2014; 2016; 2017).

The IBLGF method handles arbitrarily accelerating bodies by using an accelerating reference frame that moves with the body. This results in zero velocity at large distances. However, for a rotating body, this also results in a long downstream grid that rotates as the body rotates, requiring small time-steps in order to satisfy CFL conditions. For the present disk geometry, we take advantage of the disk's axisymmetry, which means that any rigid-body rotation about the axis of rotational symmetry does not change the space occupied by the disk. This allows us to specify velocities on the IB points that are consistent with its rigid-body rotation. This is far more computationally efficient, as the highest relative velocity in the flow now scales with $U(1+\lambda)$ on the advancing side of the disk. In summary, the disk translation is performed by translating the reference frame with the body, while the disk rotation is handled by rigid-body boundary conditions on the immersed surface. Note that the immersed surface does not translate relative to the flow grid. Physically, this corresponds to a disk moving through quiescent flow, such that fluid velocity far from the body is zero.

In continuous form, the governing equations and boundary conditions are given by

$$\frac{\partial \mathbf{u}}{\partial t} + (\mathbf{u} \cdot \nabla)\,\mathbf{u} = -\nabla p + \frac{1}{\mathrm{Re}}\nabla^2 \mathbf{u} + \int_{\Xi(t)} \mathbf{f}_\Xi(\xi, t)\delta(\mathbf{X}(\xi, t) - \mathbf{x})d\xi, \tag{2.1}$$

$$\nabla \cdot \mathbf{u} = 0, \tag{2.2}$$

$$\int_{\mathbb{R}^3} \mathbf{u}(\mathbf{x}, t)\delta(\mathbf{x} - \mathbf{X}(\xi, t))d\mathbf{x} = \mathbf{u}_\Xi(\xi, t), \tag{2.3}$$

where $\mathbf{u}(\mathbf{x}, t)$ is the fluid velocity and p is the pressure. The immersed surface is parameterized by ξ, and $\mathbf{u}_\Xi(\xi, t)$ is the velocity across its surface. Equation 2.3 represents the no-slip condition on the immersed surface, with $\mathbf{f}_\Xi(\xi, t)$ denoting the force density that is computed such that $\mathbf{u}(\mathbf{x}, t)$ satisfies this condition, with $\delta(\mathbf{X}(\xi, t) - \mathbf{x})$ as the delta function that regularizes the force onto the flow grid. These equations are solved on an unbounded domain, resulting in a decaying far-field boundary condition given by $\mathbf{u}(\mathbf{x}, t) \to 0$ as $|\mathbf{x}| \to \infty$.

2.2 Numerical setup

Figure 1.1 shows the top, side and upstream views of the simulation setup. The computational grid is fixed relative to the IB points. Disk spin is about the disk axis of axisymmetry, defined as the y-axis for $\alpha = 0°$, with positive rotation ($\lambda > 0$) in the clockwise direction when viewed from above. Angle of attack is introduced by rotating the flow vector relative to the grid. Throughout this thesis, the freestream flow is in the positive x direction. For spinning cases, where $\lambda > 0$, one side of the disk is advancing into the flow while the other side of the disk is receding away from the flow, named the advancing side and receding side, respectively, as seen in the upstream view in figure 1.1c. Note that although figure 1.1b denotes some finite thickness, we model the disk as infinitely thin using a single layer of IB points. In spite of this, by the nature of the regularization of the IB forces onto the flow grid, there will be an apparent thickness, which will be discussed in more detail in 2.3.5.

2.3 Convergence studies

While the IBLGF method has been verified and subjected to convergence tests extensively by Liska and Colonius (2017), it is necessary to select an appropriate resolution for the current studies. In this section, we describe the four resolution parameters: grid resolution, Δx; temporal discretization, Δt; IB point spacing, Δs; and domain adaption threshold, ϵ. For each, we conduct a series of tests to confirm the convergence and then select a value to use in the production simulations. We evaluate the convergence of the disk aerodynamic forces for these resolution

parameters for simulations at $Re = 500$ and $\alpha = 25°$. The lift, drag, and side force coefficients are defined by

$$C_L = \frac{F_L}{\frac{1}{2}\rho U^2 S}, \quad C_D = \frac{F_D}{\frac{1}{2}\rho U^2 S}, \quad \text{and} \quad C_S = \frac{F_S}{\frac{1}{2}\rho U^2 S}, \tag{2.4}$$

respectively, where F_L, F_D, and F_S are the corresponding dimensional forces in the y, x, and z directions, respectively, ρ is the fluid density, and $S = \pi R^2$ is the disk planform area. The rolling, pitching, and yawing moment coefficient are defined by

$$C_{MR} = \frac{M_R}{\frac{1}{2}\rho U^2 S D}, \quad C_{MP} = \frac{M_P}{\frac{1}{2}\rho U^2 S D}, \quad \text{and} \quad C_{MY} = \frac{M_Y}{\frac{1}{2}\rho U^2 S D}, \tag{2.5}$$

respectively, where M_R, M_P, and M_Y are the corresponding dimensional moments. These moments are defined relative to the disk geometry. Note that computational length and velocity scales in the code are non-dimensionalized by the disk diameter, D, and the freestream velocity, U, respectively.

2.3.1 Grid spacing, Δx

Grid resolution comparisons by Liska and Colonius (2017) for flow over the flat plate at $Re = 300$ and $\alpha = 30°$ showed a 4% difference in mean force coefficients for $\Delta x/D = 0.025$ when compared to finer resolution simulations with $\Delta x/D = 0.015$. To resolve the flow to a similar accuracy for different Reynolds numbers, we maintain the value of $(\Delta x/D)Re^{1/2}$ within the same range, based on the expected $O(Re^{-1/2})$ scaling of the laminar boundary layer thickness (Liska and Colonius, 2017). Therefore, we select a nominal grid resolution of $\Delta x/D = 0.012$ for simulations at $Re = 500$, which gives approximately the same $(\Delta x/D)Re^{1/2}$ value as for the fine case in the verification studies by Liska and Colonius (2017). This gives approximately 83 grid points across the disk diameter.

To confirm the convergence at this grid resolution we compare force coefficients between the base resolution, $\Delta x/D = 0.012$ and a finer resolution, $\Delta x/D = 0.009$. The resulting mean lift and drag coefficients and their fluctuations are shown in table 2.1 for both $\lambda = 0$ (cases A1-3) and $\lambda = 3$ (cases B1-3). Cases A1 and B1 use the base resolution ($\Delta x/D = 0.012$), while cases AII and BII use the fine grid resolution ($\Delta = 0.09$). Note that for smaller grid spacing, the fractional adaptive threshold, ϵ, is scaled such that the absolute adaptive threshold, ϵ_{abs}, is held constant, because the maximum vorticity in the flow increases as the finer grid resolves flow closer to the disk surface, where vorticity is greatest. This means that between cases A1/B1 and A2/B2, ϵ_{abs} is roughly constant.

Case	λ	$\Delta x/D$	$\Delta tU/D$	ϵ	$\overline{C_L}$	$\overline{C_D}$	ΔC_L	ΔC_D
A1	0	0.012	0.004	5×10^{-4}	0.565	0.376	0.013	0.003
A2	0	0.009	0.003	3.6×10^{-4}	0.578	0.374	0.010	0.002
A3	0	0.012	0.004	5×10^{-5}	0.561	0.374	0.015	0.003
B1	3	0.012	0.001	5×10^{-4}	0.863	0.525	0.079	0.020
B2	3	0.009	0.00075	3.6×10^{-4}	0.874	0.523	0.026	0.008
B3	3	0.012	0.001	5×10^{-5}	0.866	0.526	0.079	0.020
C1	0	0.012	0.003	5×10^{-4}	0.565	0.376	0.013	0.003
C2	0	0.012	0.004	5×10^{-4}	0.565	0.376	0.013	0.003
C3	0	0.012	0.005	5×10^{-4}	0.567	0.378	0.013	0.003

Table 2.1: Time-averaged lift $\overline{C_L}$ and drag $\overline{C_D}$ coefficients with different spatial resolutions, $\Delta x/D$, time step, Δt and adaptive threshold, ϵ. All simulations are performed at $Re = 500$ and $\alpha = 25°$. Cases A1-3 and C1-3 are at $\lambda = 0$ and cases B1-3 are at $\lambda = 3$. Cases A1, B1, and C2 correspond to the base resolution used for the remaining data presented. Cases A2 and B2 are at a lower (more accurate) adaptive threshold while cases A3 and B3 are at a finer mesh resolution. Cases C1-3 differ only by the time step value.

For the non-spinning case, results are well converged for $\Delta x/D = 0.012$ (case A1). Mean lift values are within 3% of those for the fine case $\Delta x/D = 0.009$ (case A2). The increased resolution leads to about a 20% decrease in lift oscillation amplitude, denoting a weakening of vortex shedding. This discrepancy is in the third decimal place. For the case of $\lambda = 3$, we see that the difference in mean lift is less than 2% between the two resolutions (cases B1 and B2). The discrepancy is mostly in the fluctuation amplitudes, ΔC_L and ΔC_D, which vary in the second decimal place (table 2.1). These error levels are in line with those from Liska and Colonius (2017), except for larger variations in the coefficient fluctuations at $\lambda = 3$. We note that the flat-plate convergence studies also show a decrease in fluctuation amplitude for increasing grid resolution (Liska and Colonius, 2017).

To understand the discrepancy in the signal fluctuations, we analyze the power spectral density of the lift signals. Figure 2.1 shows the PSD for these two different grid resolutions, allowing us to differentiate between the frequency peaks that contribute to the lift fluctuations. While the base grid-resolution case is dominated by a peak at $St \approx 0.5$, associated with vortex shedding, the energy for the same peak is about three orders of magnitude lower in the finer case. Both have peaks at a frequency $St \approx 1.4$, which we will later see corresponds to a short-wavelength, elliptic insta-

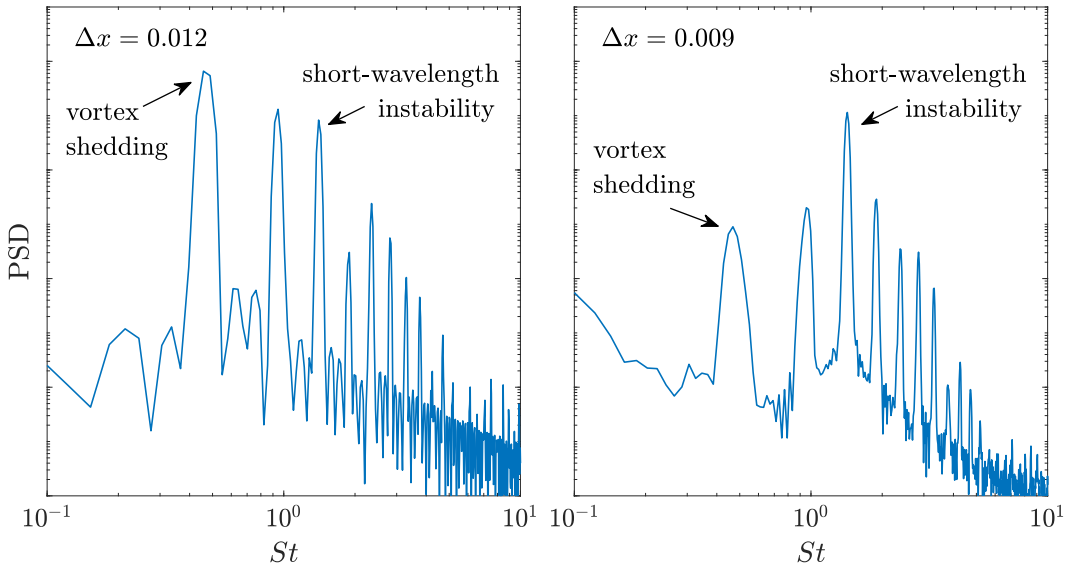

Figure 2.1: PSD for $Re = 500$, $\alpha = 25°$ and $\lambda = 3$ for grid resolutions of $\Delta x/D = 0.012$ (left) and $\Delta x/D = 0.009$ (right). The Nyquist frequencies are $St = 500$ and $St = 667$, respectively. Note that y-axes are logarithmic. Frequency bin size differs between the two plots.

bility. The energy, integrated from the PSD, of the $St = 1.4$ peaks are within 5% for both resolutions. This indicates that the discrepancy in lift fluctuation is accounted for by the difference in vortex-shedding magnitude, while the energy of the short-wavelength instability is preserved. We elaborate on this point in section 2.3.5, where we discuss the effect of disk thickness on the vortex-shedding bifurcation point.

2.3.2 Time step, Δt

For all simulations, the time step is scaled based on the maximum relative disk-edge velocity to freestream velocity using $\Delta t < \frac{\Delta x}{3} U(1+\lambda)$, which ensures that the CFL number never exceeds one during the simulation. In practice, consistent with Liska and Colonius (2017), the CFL number remains below 0.6 in the long-time simulation after reaching a maximum of around 0.9 for the early time steps. For time steps satisfying the CFL condition, lift and drag values are converged to at least the third decimal place (see cases C1-3 in table 2.1. This is a result of the second-order accuracy of the viscous integrating factor (IF) half-explicit Runge-Kutta (HERK) time integration scheme used (Liska and Colonius, 2017).

2.3.3 Immersed boundary point spacing, Δs

As mentioned in section 2.1, the infinitely-thin disk geometry is represented by a single layer of immersed-boundary points. These are generated using Distmesh, an unstructured-mesh generator developed by Persson and Strang (2004). Distmesh treats the IB points as a 2D lattice of unstructured points connected with spring edges. The mesh-point positions are relaxed using a force-based smoothing method, optimizing for uniform point spacing, while conforming to the circular disk shape. As a result, the IB spacing is not uniform across all points but follows some distribution with up to ±20% from the mean spacing. Figure 2.2 shows three different example IB spacing distributions.

The distribution of IB point spacing in the disk mesh has implications for computational accuracy. Simulations by Goza and Colonius (2017) and Kallemov et al. (2016) showed that $\Delta s/\Delta x < 2$ is sufficient to ensure body impermeability. In addition, Liska and Colonius (2017) showed that $\Delta s/\Delta x > 1$ leads to an acceptable condition number for the Schur complement operator used to solve the IB formulation. When $\Delta s/\Delta x \lessapprox 1$, the discrete Schur complement operator can become non-singular leading to numerical instability (Liska and Colonius, 2017). We test the convergence of the lift coefficient with different IB spacing and find that our results are consistent with these claims. Figure 2.2 shows the distribution of IB point spacing for different average IB point spacing, $\overline{\Delta s}$. Figure 2.3 shows the mean lift coefficient for different average IB point spacing. For IB spacing distributions that satisfy $1 < \Delta s/\Delta x < 2$, mean lift values vary only in the third decimal place. For IB distributions where some IB spacing fall beyond the acceptable limits, we see that mean lift value start to differ to the second decimal place. Therefore, we ensure that all IB point spacing throughout the mesh are restricted to the range $1 < \Delta s/\Delta x < 2$. Specifically, we use $\overline{\Delta s}/\Delta x \approx 1.6$ to minimize the number of IB points, and thus the computational cost, without sacrificing accuracy. Figure 2.2 shows that the resulting distribution allows all the grid spacing to comfortably satisfy $1 < \Delta s/\Delta x < 2$. The disk IB point geometry for $\Delta x/D = 0.012$ contains 2585 IB points and can be seen in figure A.1.

2.3.4 Adaptive domain threshold parameter, ϵ

The computational domain adapts to regions of the grid that contain non-negligible amounts of vorticity and/or the source term in the Poisson equation (Liska and Colonius, 2016). Specifically, the adaptive threshold, ϵ, is a fractional parameter based on the maximum vorticity magnitude seen in the entire computational domain,

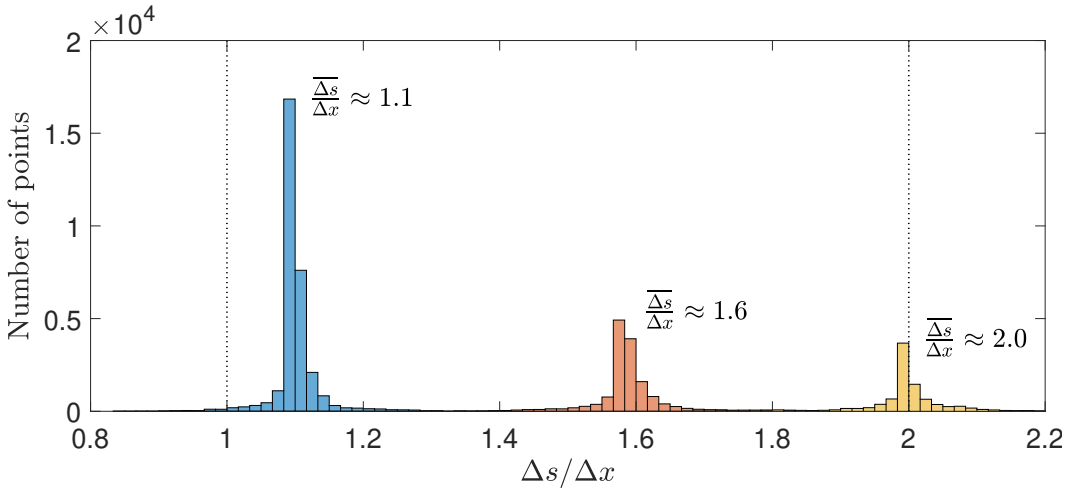

Figure 2.2: Histogram of IB point spacing for meshes with three different average IB point spacing.

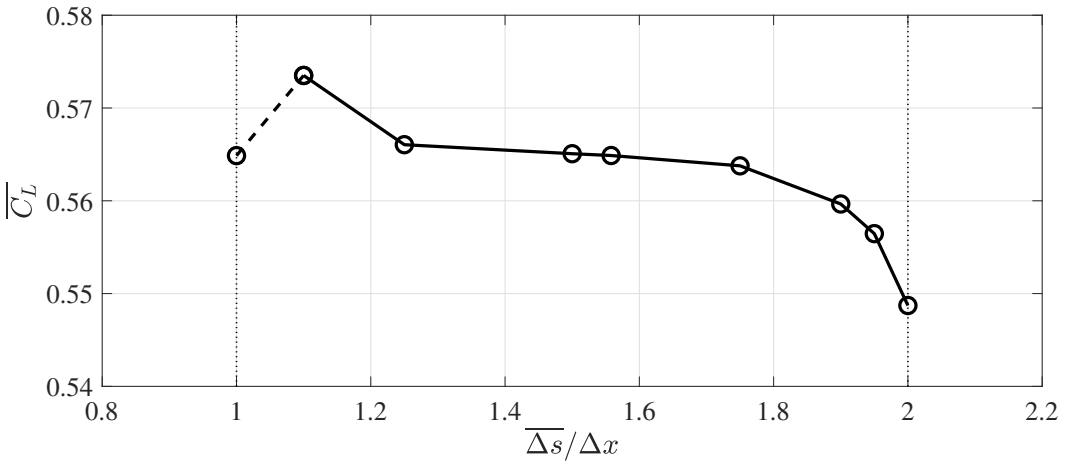

Figure 2.3: Mean lift coefficient against average IB point spacing for $Re = 500$, $\alpha = 25°$, and $\lambda = 0$. The dashed line for $\overline{\Delta s}/\Delta x < 1.1$ indicates that numerical stability is poor and the simulations are ill-conditioned and may not converge. Note that the simulation performed with $\overline{\Delta s}/\Delta x = 1.05$ did not converge.

and determines the amount of domain truncation. For example, for the vorticity term, the domain adapts to include regions of the flow that satisfy:

$$||\omega|| \geq \epsilon_{abs} = \epsilon \max_{\mathcal{D}} ||\omega||, \tag{2.6}$$

where ω is the vorticity vector, ϵ_{abs} denotes the absolute threshold value for the smallest vorticity magnitude values tracked, and $\mathcal{D}$ denotes the computational grid. In practice, $0 < \epsilon < 1$ where $\epsilon = 0$ means the computational grid would extend infinitely (adaption to all values of vorticity). For simulations in this thesis, we use $\epsilon = 5 \times 10^{-4}$, matching studies by Liska and Colonius (2017).

In table 2.1, we compare time-averaged lift and drag coefficients for the base adaptive threshold at $\epsilon = 5 \times 10^{-4}$ and a finer adaptive threshold at $\epsilon = 5 \times 10^{-5}$. Comparing aerodynamic coefficients for $\lambda = 0$ (cases A1 and A3) and $\lambda = 3$ (cases B1 and B3) shows that the mean values and their fluctuations show excellent agreement for a tenfold difference in adaptive threshold, with differences only observed in the third decimal place. This agreement continues for $\Delta x/D = 0.009$ as well. Note that the noise levels in the aerodynamic signals scales approximately linearly with the adaptive threshold due to the discrete addition and removal of computational blocks as the domain adapts. For steady signals at $\Delta x/D = 0.012$, the noise level in lift is at most ± 0.001 for $\epsilon = 5 \times 10^{-4}$ and decreases to ± 0.0001 for $\epsilon = 5 \times 10^{-5}$.

2.3.5 Effect of thickness on the vortex shedding bifurcation

While the effect of thickness is not formally explored in this thesis, we take a moment to discuss its potential effects on the simulation results, as it may account for the discrepancy in lift fluctuations with changing grid resolution presented in section 2.3.1. Disk thickness has been shown to change the value of critical points of disk flow bifurcation and even the nature of the bifurcation (Chrust, Dauteuille, et al., 2015; Gao et al., 2018; Meliga, Chomaz, and Sipp, 2009; Auguste, Fabre, and Magnaudet, 2010).

While we model the disk using a single layer of IB points, the regularization of the IB forces onto the flow grid using a delta function results in a narrow strip of grid points surrounding the IB points over which the disk surface forcing influences the flow directly. Figure 2.4 is a schematic of the regularization of the IB forces from the IB points. Note that the magnitude of the IB forcing falls off with the distance from the IB points, following the delta function profile. While not directly equivalent to a physical disk thickness, this results in an apparent thickness for the disk. Specifically, we use a smoothed 3-point delta function which has a support

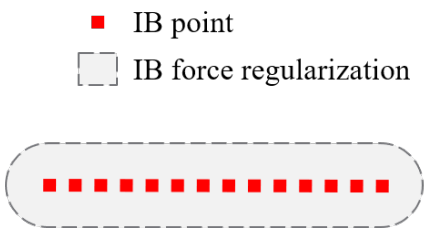

Figure 2.4: Schematic of the IB points and the effective thickness due to the regularization of IB forces onto the grid.

of up to two grid points in either direction (Yang et al., 2009; Roma, Peskin, and Berger, 1999). As a result, the apparent disk thickness scales with the grid spacing, resulting in a thinner disk for finer resolutions. For $\Delta x/D = 0.012$, this gives an approximate upper limit of the apparent thickness of $t_d = 0.048$ (or aspect ratio $\chi \approx 21$). For the finer resolution $\Delta x/D = 0.009$, the apparent thickness is at most $t_d = 0.036$ ($\chi \approx 28$).

This makes it challenging to fully separate the effects of thickness and grid resolution since they vary together by the nature of the IB method. However, the changing force coefficient fluctuations with changing grid resolution observed in section 2.3.1 are consistent with the trends seen in the literature for the effect of thickness. As mentioned in section 1.3, for $\alpha < 40°$, a higher disk aspect ratio (thinner disk) increases the critical Reynolds number at which the vortex-shedding bifurcation occurs, i.e. it stabilizes the flow. For reference, at $\alpha = 30°$, Chrust, Dauteuille, et al. (2015) find a critical Reynolds number of $Re_c = 267$ for a thick disk ($\chi = 6$), while Gao et al. (2018) determine $Re_c = 377$ for a thin disk ($\chi = 50$). For the current method, we estimate $Re_c \approx 320$ for $\alpha = 30°$ and $\chi \approx 21$ (estimated in section 2.4.2), which falls accordingly between the thick and thin disk cases. While the data on thickness effects at low angles of attack is sparse and involves comparisons between multiple studies, this trend suggests that for the current simulations, as the grid spacing and apparent IB thickness decrease, the critical Reynolds number will increase, stabilizing the flow.

Consistent with this effect, we observe decreased lift and drag fluctuation amplitudes as the grid spacing decreases for both $\lambda = 0$ and $\lambda = 3$ (table 2.1). As a side note, Liska and Colonius (2017) also observe modest decreases in the lift and drag fluctuations with decreasing grid spacing, possibly due to thickness effects on vortex shedding as well. At $Re = 500$ and $\lambda = 0$, the critical angle of attack is roughly

24.3° (estimated in section 2.4.2). Therefore, for simulations at $\alpha = 25°$ which are very close to the critical point, we can expect the vortex shedding and resulting lift and drag fluctuation amplitudes to be particularly sensitive to thickness effects or potential underresolution. In section 2.3.1, for $\lambda = 3$, the PSD analysis between the base and fine resolution cases showed that vortex shedding was significantly weakened in the fine case, with little effect on the strength of the short-wavelength instability. We expect the elliptic instability, which is an instability in the tip vortices, to be relatively independent of changing thickness as it depends primarily on the tip-vortex parameters rather than on the exact geometry of the disk. However, we do recognize that the decrease in vortex-shedding strength is much larger at $\lambda = 3$ than at $\lambda = 0$, so we do not rule out that there may be some underresolution at play as well for high TSRs. Potential underresolution would depend on the effect of spin on the boundary layer thickness to be resolved. While the boundary layer caused by a rotating disk (in quiescent flow) is significantly larger than that for a traditional flat plate laminar boundary layer, the rotating disk boundary layer continues to decrease with increasing TSR and may decrease the grid spacing required to accurately resolve the flow close to the disk.

In summary, thickness effects seem to account for decreasing vortex-shedding strength, which is consistent with results in the literature, though there may also be some degree of underresolution at high TSRs. In production runs for this work, we use a resolution of $\Delta x/D = 0.012$ which represents an apparent thickness of $t_d = 0.048$ or aspect ratio of $\chi = 21$. This is slightly underresolved for the purposes of representing an infinitely thin disk, but allows us to explore high TSRs that would otherwise be far more computationally intensive. This allows us to explore new flow regimes that appear and understand the mechanisms behind them. The limitation in accurately defining and maintaining a thickness for the disk means that there remains uncertainty in the precise bifurcation parameters and aerodynamic forces and moments, specifically with respect to the actual thickness. However, we maintain that the key trends and flow features are preserved with the chosen resolution.

2.4 Comparisons with previous simulations for the non-spinning disk

In this section we verify our results by comparing aerodynamic forces and critical points with past DNS results for non-spinning disks by Chrust, Dauteuille, et al. (2015), Tian et al. (2017), and Gao et al. (2018). These studies focus on high angles of attack $\alpha > 30°$. In order to overlap with some of these results, we make comparisons over the range $30° < \alpha < 60°$. Unfortunately, we are not aware of any

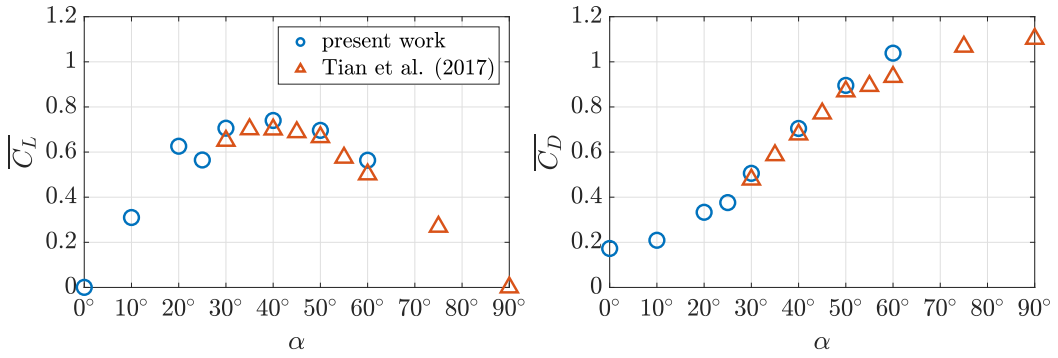

(a) (b)

Figure 2.5: Time-averaged lift and drag coefficients for the non-spinning disk at $Re = 500$. The signal length for computing time-averages is at least 170 tU/D for unsteady cases, leading to standard error values at most $2 \cdot 10^{-4}$. The standard error is largest for the quasi-periodic and chaotic cases at higher angles of attack.

spinning disk cases to compare to for a flat disk at these Reynolds numbers.

2.4.1 Aerodynamic force comparisons

In figure 2.5, we compare mean lift and drag values for $Re = 500$ and $\lambda = 0$ over a range of angles of attack to those reported by Tian et al. (2017). Good agreement is observed with discrepancies ranging from 3% to 12% for both lift and drag values. We observe a small dip in C_L of about 0.06 units from $\alpha = 20°$ to $\alpha = 25°$. This is greater than the error estimate (±0.01 units) so we expect it to be a physical observation. This coincides with the transition from steady flow to vortex shedding. This dip may be associated with this transition in the wake stability or also a symptom of the flow's sensitivity close the critical point, as we will find that $\alpha_c = 24.3°$ (section 2.4.2). Direct comparisons to circular disk flows are not available. However, Taira, Dickson, et al., 2007 observed a similar dip at the same angle of attack for two-dimensional flow over a flat plate at $Re = 100$. On the other hand, Taira and Colonius (2009) did not observe a dip in lift coefficient for three-dimensional flow over a rectangular flat plate for aspect ratios from one to four.

2.4.2 Critical Reynolds number comparisons

Chrust, Dauteuille, et al. (2015) and Gao et al. (2018) determined the critical Reynolds number for the first (Hopf) bifurcation for a range of angles of attack. To compare to their results, we estimate the critical Reynolds number by making use of the fact that near a supercritical Hopf bifurcation, the peak-to-peak amplitude of the

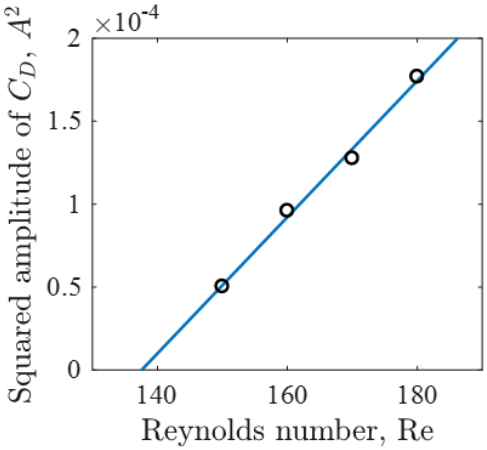

Figure 2.6: Drag amplitude squared against Reynolds number for $\alpha = 50°$. The solid line is a linear regression whose x-intercept marks Re_c.

oscillation, A, is directly proportional to the square root of the degree of criticality of the bifurcation parameter (Ghaddar et al., 1986; Pereira and Sousa, 1993). Using, for example, the drag coefficient, let $A = \max(C_D) - \min(C_D)$, which according to the theory is given by

$$A^2 = B\,(Re - Re_c)\,, \tag{2.7}$$

where B is a constant of proportionality. By measuring A^2 at several supercritical values of Re, and performing a regression to determine m, we efficiently obtain the resulting Re_c by measuring the intercept. We can likewise use the angle of attack as the bifurcation parameter in which case the degree of criticality is $\alpha - \alpha_c$. Figure 2.6 shows a sample extrapolation to estimate the critical Reynolds number at $\alpha = 50°$. A similar extrapolation approach is used to obtain estimates of the critical Strouhal number, $St_c = f_c D/U$, where f_c is the dimensional frequency.

In figure 2.7, we compare the values we obtain for critical Reynolds number, Re_c, and critical Strouhal number, St_c, as a function of angle of attack to values reported in the literature for various disk aspect ratios in the range $6 \leq \chi \leq \infty$ by Chrust, Dauteuille, et al. (2015) and Gao et al. (2018). The values show great agreement, particularly at high angles of attack. For low angles of attack, the critical Reynolds number varies with the disk aspect ratio. For $\alpha = 30°$, $Re_c = 320$ for the present work for an estimated aspect ratio $\chi \approx 21$. This falls between the values from Gao et al. (2018) for the thin disk ($Re_c = 377$ for $\chi = 50$) and from Chrust, Dauteuille, et al. (2015) for the thick disk ($Re_c = 267$ for $\chi = 6$). By comparing these cases, we see that a thicker disk results in a lower critical Reynolds number for $\alpha < 40°$, but higher critical Reynolds number for $\alpha > 40°$. These results are consistent with

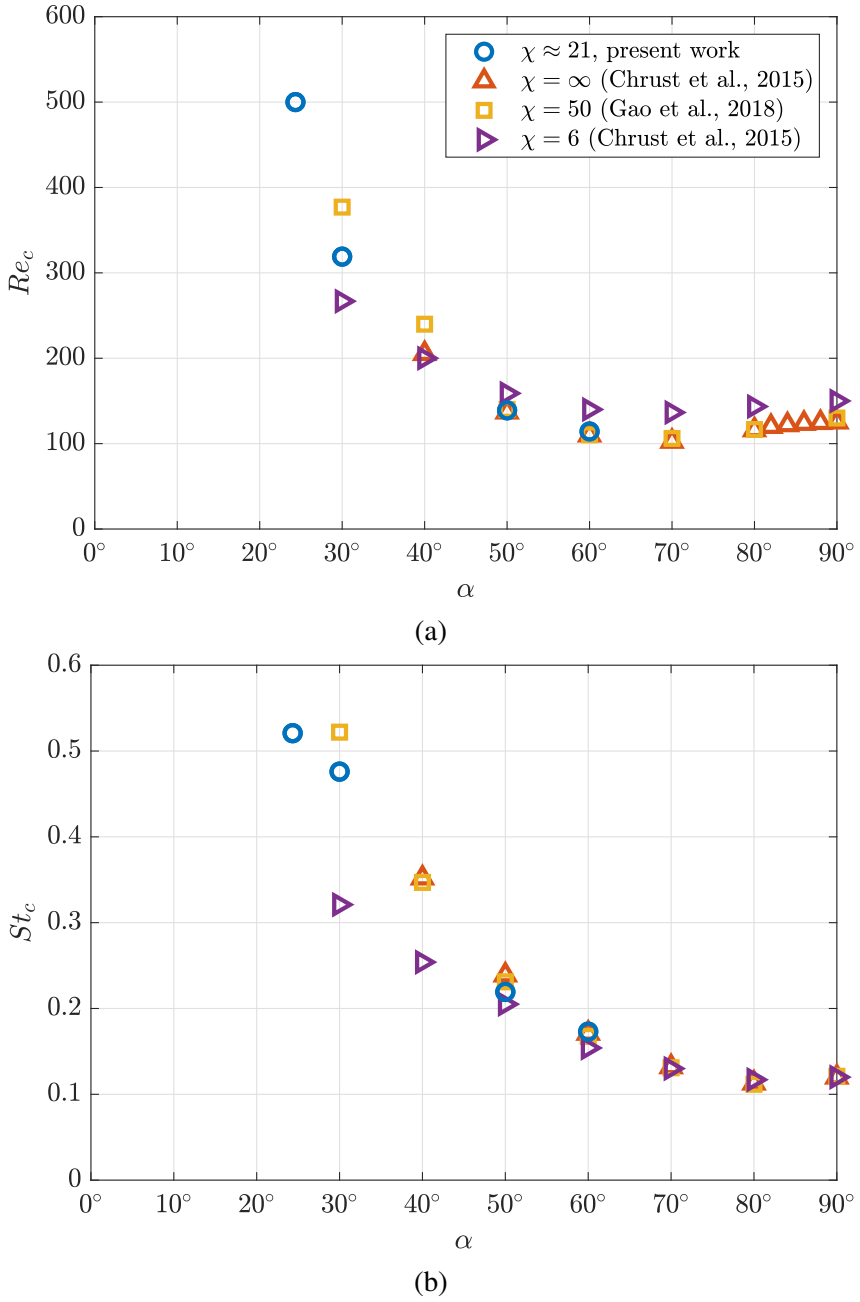

Figure 2.7: (a) Critical Reynolds number and (b) critical Strouhal number against angle of attack for the supercritical Hopf bifurcation from steady to periodic vortex shedding.

the decreasing ΔC_L and ΔC_D observed as we used a finer mesh (and thus effectively thinner disk) in section 2.3.1.

2.5 Parameter Selection

The remaining chapters present results for various simulations of flow over the spinning disk at angle of attack. Table 2.2 lists the production runs upon which the results of this thesis are based and references where they appear. This does not include the simulations performed for convergence studies. The simulations presented in this work used the Extreme Science and Engineering Discovery Environment (XSEDE) Stampede 2 at the Texas Advanced Computing Center through allocation TG-CTS 120005. XSEDE is supported by National Science Foundation grant number ACI-1548562 (Towns et al., 2014).

Table 2.2: Production runs and the associated parameters and sections where they are included

Description	Sections	Re	α (°)	λ
λ sweep	2, 3, 4, 5	500	25	0, 0.25, 0.5, 0.75, 1.0, 1.25, 1.5, 1.6, 1.7, 1.75, 1.8, 1.9, 2.0, 2.1, 2.2, 2.3, 2.4, 2.5, 2.6, 2.7, 2.8, 2.9, 3.0
α sweep	2.4, 3.1.1, B	500	0, 10, 20, 25, 27, 30, 32, 35, 40, 50, 60	0
Re_c estimation	2.4.2	320, 330, 340, 350, 360	30	0
Re_c estimation	2.4.2	140, 150, 160, 170, 180	50	0
Re_c estimation	2.4.2	120, 130, 140, 150	60	0
Shedding effects	4.1.2	500	30	0, 1, 2
Shedding effects	4.1.3	120	60	0, 1, 2
PSL effects	4.1.4	300	50	0, 1, 2
Parallel flow	4.2, C	100	0	0, 1, 2, 4
Rotation only	4.2.2, C	N/A	N/A	$Re_\omega = 100$
High Re	5.7	4000	25	0, 2

Chapter 3

SPINNING DISK AERODYNAMICS AND WAKE STRUCTURE

Past studies have identified several wake regimes for flow over non-spinning inclined disks at $Re = O(10^2)$ (Chrust, Dauteuille, et al., 2015; Tian et al., 2017; Gao et al., 2018). Both Reynolds number and angle of attack serve as bifurcation parameters that take the flow from steady to chaotic as they are increased. The goal of this chapter is to explore the effect of spin on these bifurcations. We study the changing aerodynamics and wake instabilities in this same Re-α parameter space. To this end, we simulate the flow through a range of TSRs from zero to three, while fixing the Reynolds number and angle of attack at $Re = 500$ and $\alpha = 25°$. With no spin ($\lambda = 0$), this flow configuration is supercritical with respect to the first bifurcation ($\alpha_c = 24.3°$ at $Re = 500$) and exhibits mild vortex shedding. By analyzing the changing frequency content and visualizing vorticity isosurfaces, we can identify several distinct wake regimes of interest.

3.1 Aerodynamic forces for a spinning disk

Figure 3.1 shows the long-time time-varying and time-averaged lift and drag coefficients as λ varies. Both lift and drag follow similar trends with increasing λ, though the mean value and fluctuation amplitudes remain higher for lift than for drag throughout. The mean lift and drag both increase monotonically as λ is increased. The fluctuations in lift and drag over time show a more complex and non-monotonic behavior. For the non-spinning case at $\lambda = 0$, at which the flow is only slightly supercritical with respect to the wake (vortex-shedding) instability, the lift fluctuations are small in amplitude and monochromatic. As λ increases to 1.5, the oscillation amplitude decreases to zero, while the fluctuations remain monochromatic. For cases from $\lambda = 1.5$ to $\lambda = 1.7$ inclusive, the lift and drag values are steady, indicating a steady flow, as vortex shedding is suppressed.

For $\lambda \gtrapprox 1.75$, the flow becomes unsteady again. From $\lambda = 1.7$ to $\lambda = 3$, the fluctuation amplitudes generally increases. Just past $\lambda = 1.7$, the fluctuations are again monochromatic with a similar frequency as $\lambda < 1.5$, indicative of flow being once again slightly supercritical. As λ is further increased, the flow remains in a limit cycle behavior. However, the waveforms become more complex and non-monochromatic, indicating that the flow passes through additional bifurcations. We

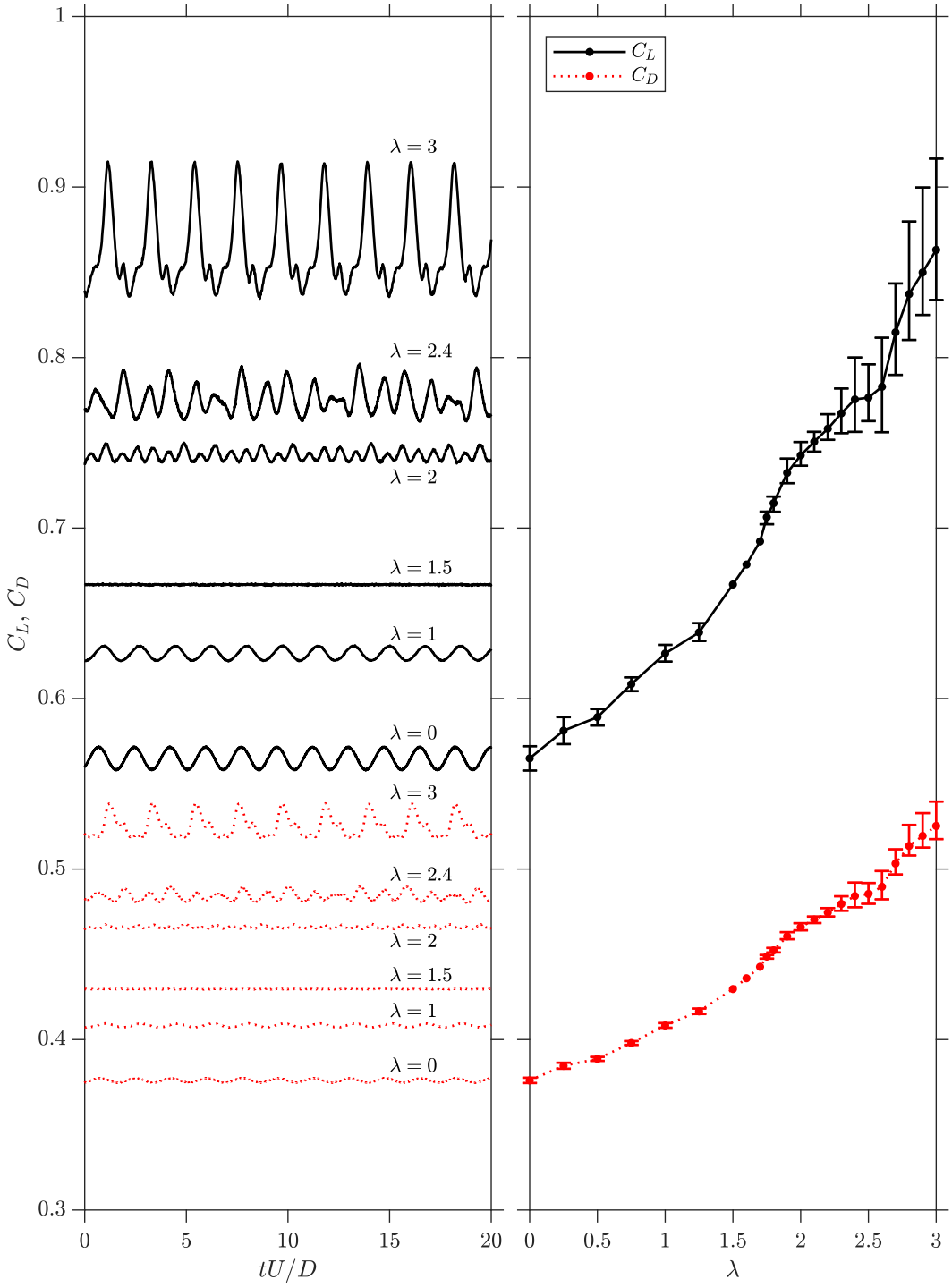

Figure 3.1: Time-varying (left column) and time-averaged (right column) lift coefficients, C_L, and drag coefficients, C_D, for the spinning disk at different tip-speed ratios, λ, for $Re = 500$ and $\alpha = 25°$. Error bars indicate the min-to-max range of coefficient values for unsteady cases. The signal length for computing time-averages is at least 70 tU/D for unsteady cases, leading to standard error values at most $7 \cdot 10^{-5}$.

will later identify a short-wavelength elliptic instability at these high TSRs.

Figure 3.2 shows mean side-force and moment coefficients and their fluctuations for $0 \leq \lambda \leq 3$. The side force and its fluctuation are initially zero due to the planar symmetry of the non-spinning disk flow at $Re = 500$ and $\alpha = 25°$. As λ increases, the planar symmetry breaks, with the force acting towards the receding side of the disk ($z < 0$). The overall increase in side force is non-monotonic, with a region of decrease from $\lambda \approx 1.25$ to $\lambda \approx 2$, which corresponds to the steady region and onset of the short-wavelength instability. The fluctuation amplitude increases after the steady region, following lift and drag force trends.

The rolling moment is zero for the non-spinning case due to the planar symmetry of the flow. It initially decreases slightly to a negative value, with a minimum at $\lambda \approx 0.75$ and then increases monotonically from there. The rolling moment is negative for $\lambda \lessapprox 1.25$ and positive for $\lambda \gtrapprox 1.25$. This means that for $\lambda \gtrapprox 1.25$ the disk will bank to the receding side of the disk, and vice versa for $\lambda \lessapprox 1.25$. Because the center of pressure center of gravity of the disk are different, the pitching moment is positive for the non-spinning disk. This represents a moment that acts to increase angle of attack. The rolling moment does not change significantly as TSR is changed, compared to changes due to angle of attack. The yawing moment, which is aligned with disk spin and can be thought of as a torque countering the spin, is zero for the non-spinning disk. As expected, it increases as the TSR increases.

3.1.1 Lift-to-drag ratio

The lift-to-drag ratio, C_L/C_D, is an important variable to optimize for flight. To get a sense of the effect spin has on the relationship between lift and drag, we examine how the time-averaged lift-to-drag ratio changes with both angle of attack and tip-speed ratio (figure 3.3). As angle of attack is increased from zero for the non-spinning disk, the lift-to drag ratio increases to a peak of $C_L/C_D = 1.9$ at $\alpha = 20°$. It then decreases as angle of attack is further increased. In comparison, when the angle of attack is fixed at $\alpha = 25°$ and TSR is varied, the lift-to-drag ratio increases by about 9% from $C_L/C_D = 1.50$ at $\lambda = 0$ to $C_L/C_D = 1.64$ at $\lambda = 3$. Although mean lift and drag values show relatively large changes with TSR (figure 3.1), since they both increase, the change in their ratio is modest. Thus, the lift-to-drag ratio is determined predominantly by the angle of attack rather than the TSR.

Figure 3.4 shows the lift against drag for both varying angle of attack and varying TSR. As angle of attack increases with fixed $\lambda = 0$, drag increases monotonically

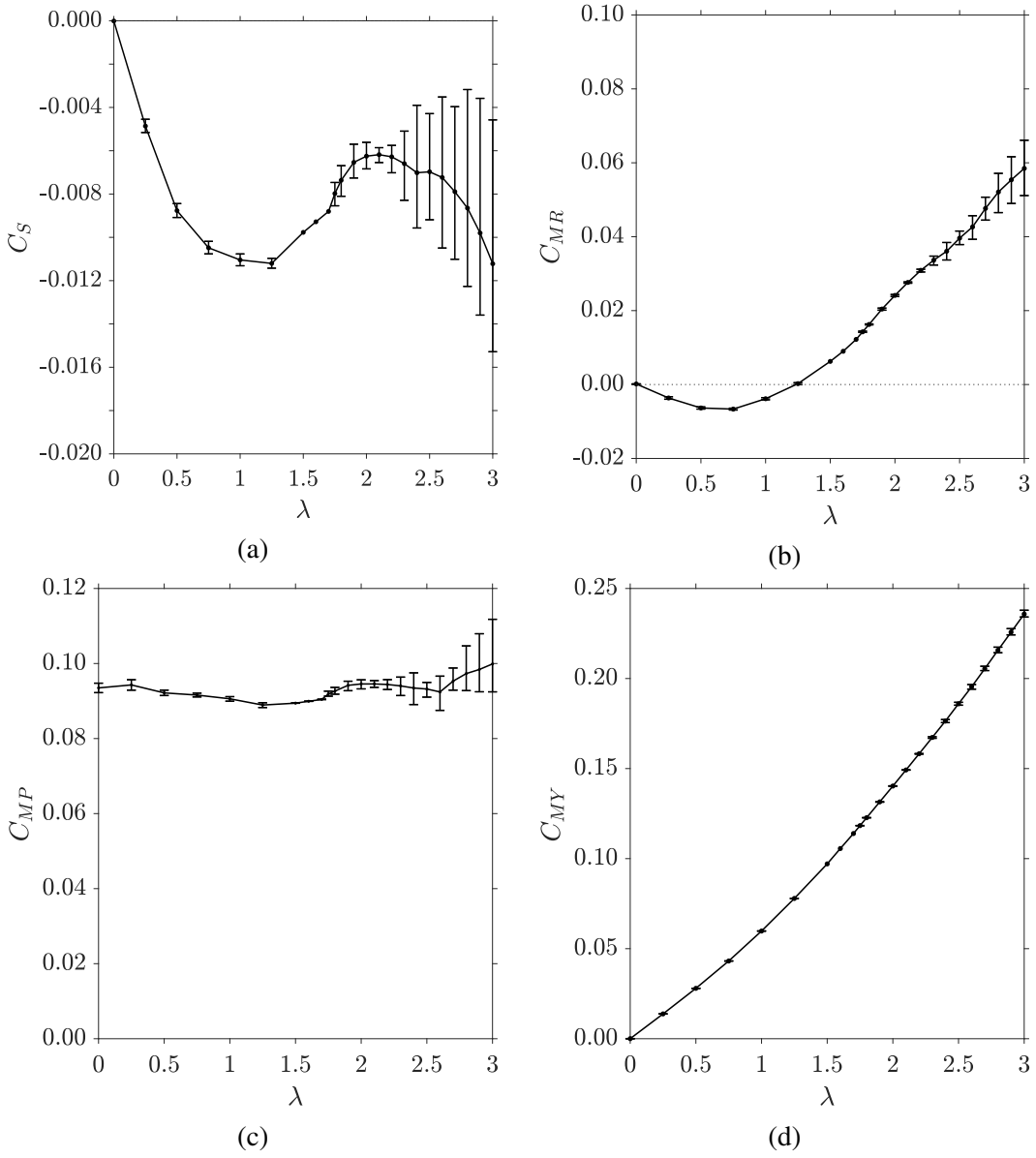

Figure 3.2: (a) Side force, (b) rolling moment, (c) pitching moment, and (d) yawing moment for the spinning disk at different tip-speed ratios, λ, for $Re = 500$ and $\alpha = 25°$. Error bars indicate the min-to-max range for unsteady cases.

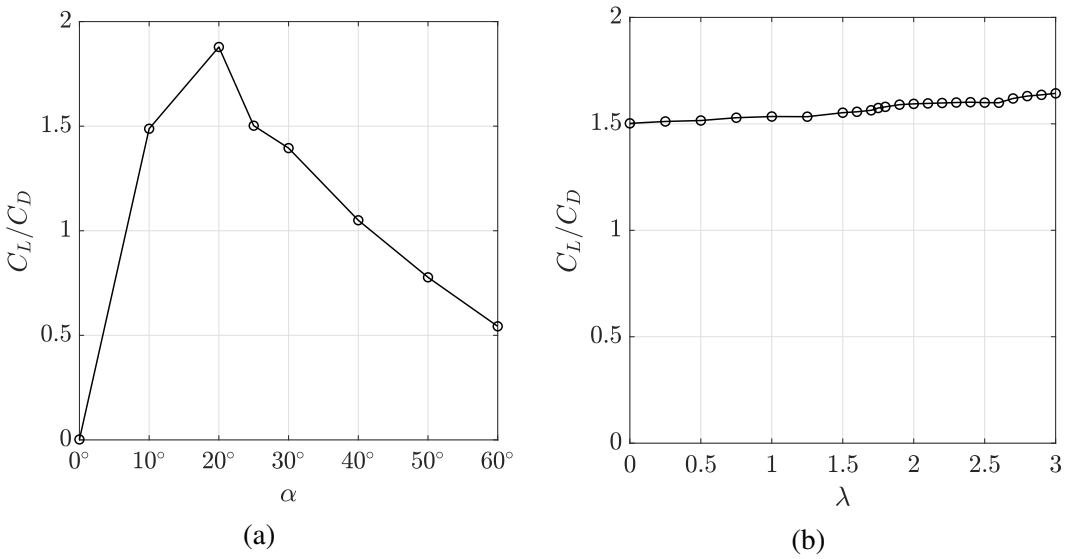

Figure 3.3: Time-averaged lift-to-drag ratio (a) against angle of attack with fixed $\lambda = 0$ (non-spinning) and (b) against tip-speed ratio with fixed $\alpha = 25°$, both at $Re = 500$.

from $C_D = 0.17$ at $\alpha = 25°$ to $C_D = 1.04$ at $\alpha = 60°$. Lift increases from $C_L = 0$ at $\alpha = 0°$ to a peak value of $C_L = 0.70$ at $\alpha = 40°$ before decreasing to $C_L = 0.56$ at $\alpha = 60°$. When angle of attack is fixed at $\alpha = 25°$ and tip speed ratio is varied instead, both lift and drag increase steadily. The magnitude of changes in lift and drag for TSR variation from zero to three is similar to that for changes of about five to ten degrees in angle of attack.

We can define a normal force coefficient, $C_\perp$:

$$C_\perp = \frac{F_\perp}{\frac{1}{2}\rho U^2 S}, \tag{3.1}$$

where $F_\perp$ is the normal force on the disk, aligned with the lift force for $\alpha = 0°$. The normal force coefficient is equivalent to the surface-averaged pressure coefficient and denotes the net pressure force experienced by the disk. The normal force coefficient increases as angle of attack increases, except for a small dip from $\alpha = 20°$ to $\alpha = 25°$ that corresponds to the transition from steady to vortex shedding, where the recirculation bubble geometry will change as vorticity is shed (figure 3.5b). When TSR is increased instead, $C_\perp$ increases, showing an overall decrease in pressure on the suction side versus pressure side of the disk.

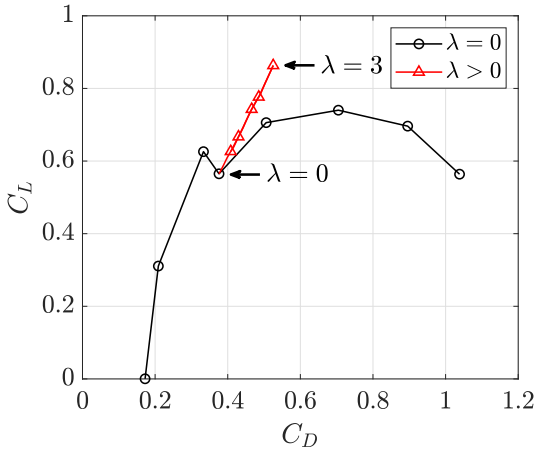

Figure 3.4: Lift against drag for varying angle of attack ($0° \leq \alpha \leq 60°$, $\lambda = 0$) and varying tip-speed ratio ($0 \leq \lambda \leq 3$, $\alpha = 25°$), for the disk at $Re = 500$. Red triangle markers denote 0.5 increments in λ.

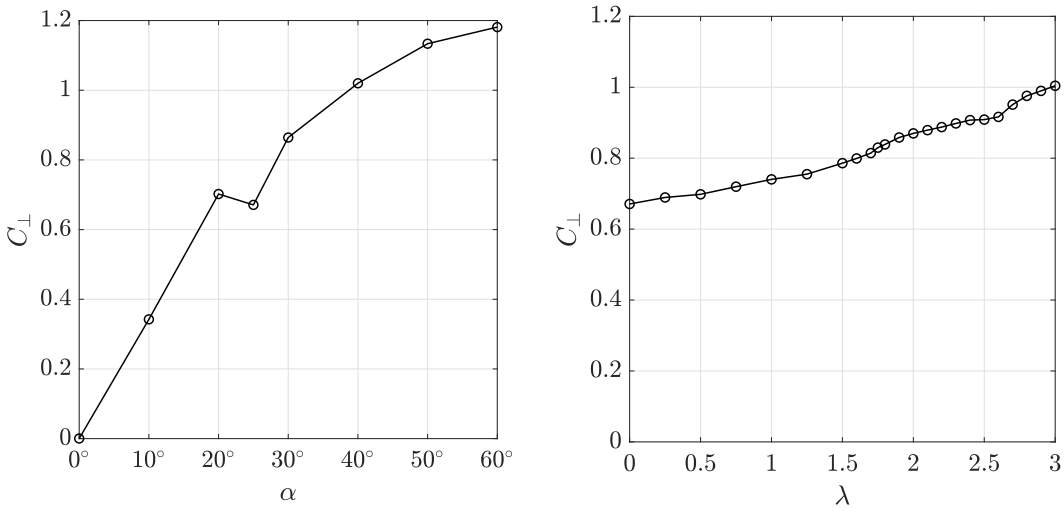

(a) (b)

Figure 3.5: Time-averaged normal force coefficient (a) against angle of attack with fixed $\lambda = 0$ (non-spinning) and (b) against tip-speed ratio with fixed $\alpha = 25°$, for the disk at $Re = 500$.

3.2 Wake regimes for a spinning disk

The transition to unsteadiness in force and moment coefficients is suggestive of instabilities. To better understand the flow phenomenon that give rise to these trends, we examine the frequency content of the aerodynamic forces alongside visualizations of the wake structure. Figure 3.6 visualizes isosurfaces of streamwise and spanwise vorticity for selected values of λ between zero to three. Figure 3.8 shows top views of the vorticity isosurface visualizations. The top view provides a clearer view of the vortex loops that pass through the center plane, which indicates roll-up of the trailing edge vortex sheet into hairpin vortices. These visualizations allow us to identify several distinct wake regimes which we will describe in this section. These regimes are:

1. regime 1 ($0 \lessapprox \lambda \lessapprox 1.9$), a standard wake instability, modulated from slightly supercritical to subcritical and back to supercritical,
2. regime 2 ($1.9 \lessapprox \lambda \lessapprox 2.2$), a short-wavelength instability (later identified as an elliptic instability), and
3. regime 3 ($2.2 \lessapprox \lambda \lessapprox 3$), a combination of both the wake instability and the short-wavelength instability.

Figure 3.7 shows Welch's power spectral density (PSD) estimate of the lift coefficient, which helps to distinguish between different instabilities in the wake. We use the same time period for all of the signals, so the frequency bins are also equal in size. Therefore, the y-axes are arbitrary, but equivalent logarithmic scales. We omit the PSD for the steady $\lambda = 1.5$ case, which lies below the lower limit of the y-axes and consists of frequency content from noise in the signal. By observing changes in the wake structure in a series of visualization snapshots of the wake, we can associate the Strouhal numbers from the PSD peaks with different wake behaviors.

To reveal trends in the changing frequency content with increasing TSR, we determine the frequency peaks with total energies exceeding a certain threshold and plot them against λ (figure 3.9). The marker sizes are scaled based on the peak's total energy, which is found by integrating over each peak in Welch's PSD estimate. The maximum frequency bin size is $\Delta St = 0.04$. Peaks are relatively distinct and compact, with their energies converging to at least 90% of the total energy for integration bin sizes of about $\Delta St = 0.1$. These plots reveal a great deal of information about the flow physics that is discussed in detail in the following chapters. For now,

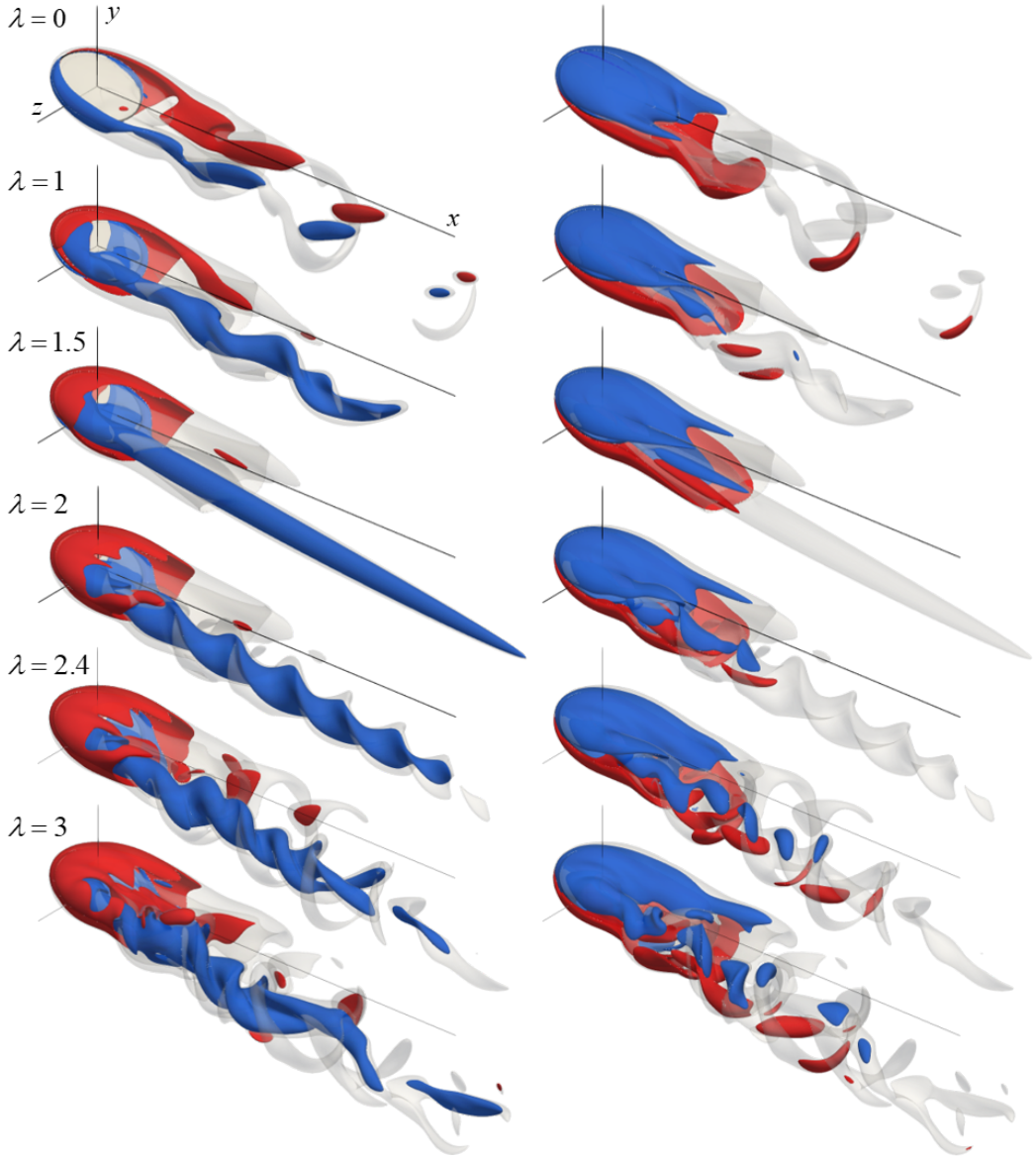

Figure 3.6: Isosurfaces of vorticity for the disk at $Re = 500$ and $\alpha = 25°$ for $\lambda = 0, 1, 1.5, 2, 2.4$, and 3. Flow is from top left to bottom right with the disk rotating clockwise from above. Semi-transparent grey isosurfaces are vorticity magnitude, $||\omega|| = 3$. Streamwise vorticity, ω_x (left column) and spanwise vorticity, ω_z (right column) are shown in opaque red and blue for positive (+3) and negative (-3) values, respectively. The x-, y-, and z-axes reference lines are $5D$, $1D$, and $1D$ long, respectively.

we present a general overview of the key features that arise in order to identify the different wake regimes.

3.2.1 Wake instability and its suppression

For the non-spinning disk ($\lambda = 0$), the wake instability causes the trailing-edge vortex sheet to roll up and shed from the disk periodically. The roll up interacts with segments of the tip vortices to form spanwise-symmetric hairpin vortices which loop across the center plane with legs extending towards the disk (grey isosurfaces in figure 3.6). The power spectrum indicates monochromatic frequency content associated with the wake instability. For $\lambda = 1$, the magnitude of the single frequency peak associated with vortex shedding has decreased from the non-spinning case (figure 3.1). The wake loses its spanwise symmetry, with the hairpin vortices becoming relatively more distinct on the advancing side of the disk ($z > 0$ side) compared to the receding side ($z < 0$ side). The frequency of these fluctuations is $St \approx 0.55$ and remains relatively unchanged between $\lambda = 0$ and $\lambda = 1.5$ (figure 3.9).

For $\lambda = 1.5$, vortex shedding is suppressed and the flow is again steady, indicating that the flow is subcritical with respect to the wake instability (figure 3.6). This behavior and the corresponding lack of hysteresis is consistent with the standard view of the wake instability arising as a supercritical Hopf bifurcation. The trailing-edge vortex sheet no longer rolls up. This vortex-shedding suppression persists in a range from roughly $\lambda = 1.5$ to $\lambda = 1.7$ (figure 3.9). The tip vortex on the advancing side of the disk ($z > 0$) is significantly strengthened while that on the receding side is more diffuse. This vorticity distribution and the mechanism behind the stabilizing effect is discussed in detail in Chapter 4.

3.2.2 Short-wavelength instability

In the range of $1.9 \lessapprox \lambda \lessapprox 2.2$, high-frequency content at $St \approx 1.3$ dominates the spectra (figure 3.9). This corresponds to a corkscrew-shaped instability in the advancing tip-vortex core, with a short wavelength relative to the inter tip-vortex distance (figure 3.8). As λ increases through this narrow range $1.9 < \lambda < 2.2$, the wavelength decreases slightly and the frequency increases slightly as well. The frequencies match closely with twice the rotation frequency of the disk rotation, indicated by the dashed line (figure 3.9). For $\lambda = 2$, most of the energy of the flow is associated with this instability at $f = 1.31$. This short-wavelength instability has a frequency about 2.5 times that of the vortex-shedding frequency and strongly

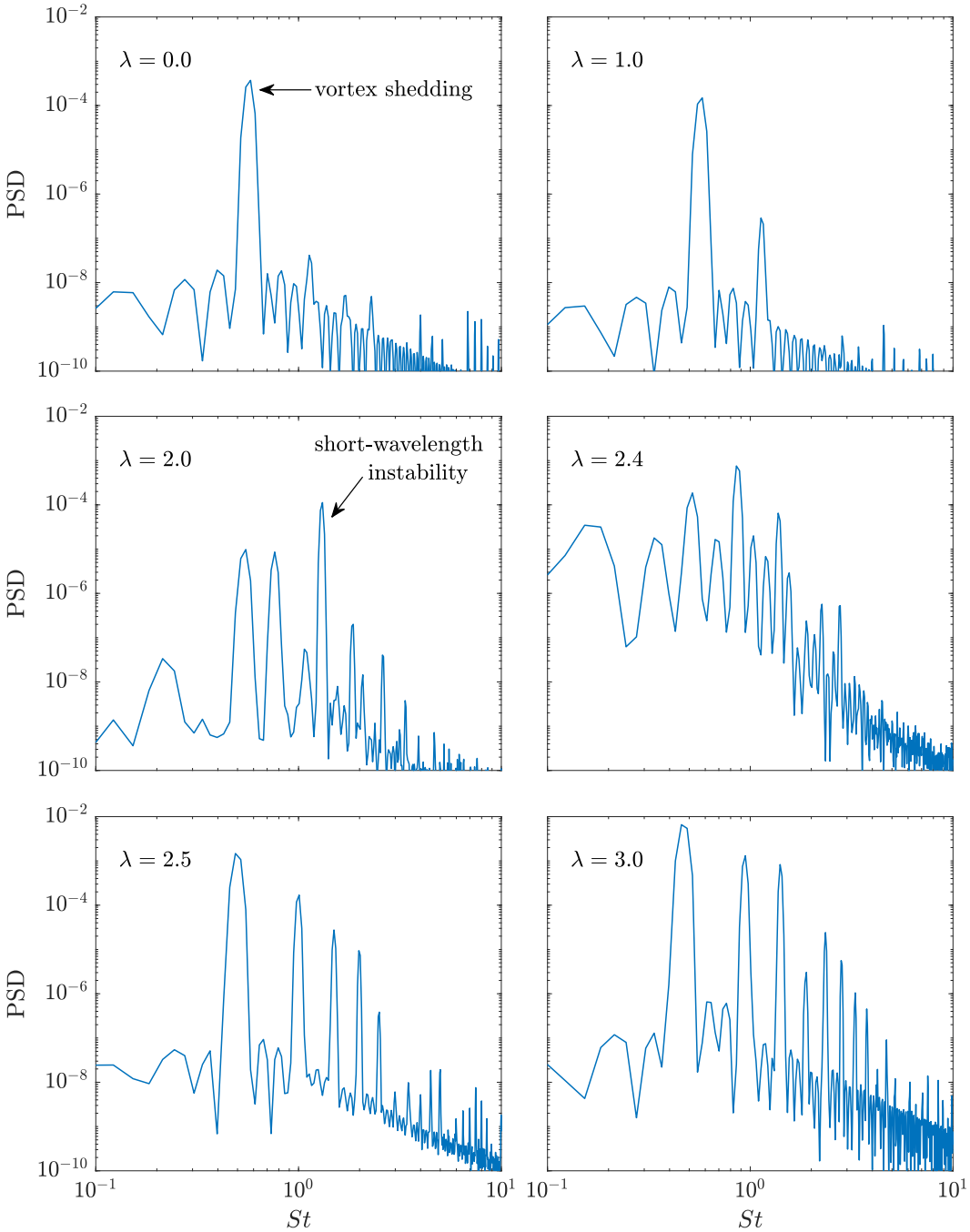

Figure 3.7: Welch's PSD estimate of the lift trace for the disk at $Re = 500$ and $\alpha = 25°$ for various λ. All cases are performed for the same time period so the frequency bin sizes are the same giving a frequency resolution of $\Delta St = 0.03$. Thus the y-axes are arbitrary, but equivalent logarithmic scales. The Nyquist frequency is inversely proportional to the timestep size, ranging from $St = 125$ for $\lambda = 0$ to $St = 500$ for $\lambda = 3$.

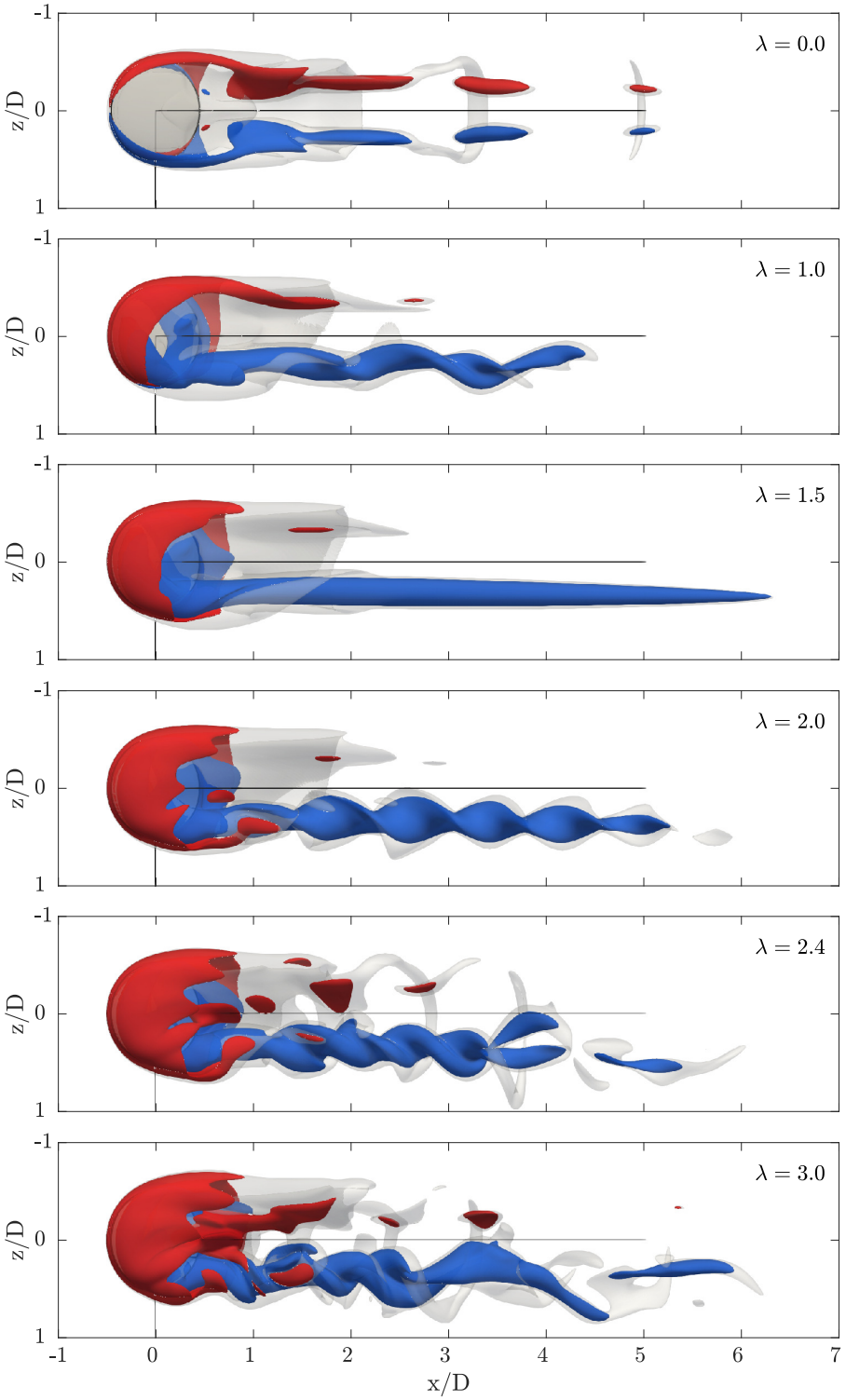

Figure 3.8: Top view of isosurfaces of vorticty for the disk at $Re = 500$ and $\alpha = 25°$ for various λ. Isosurfaces are the same as for figure 3.6.

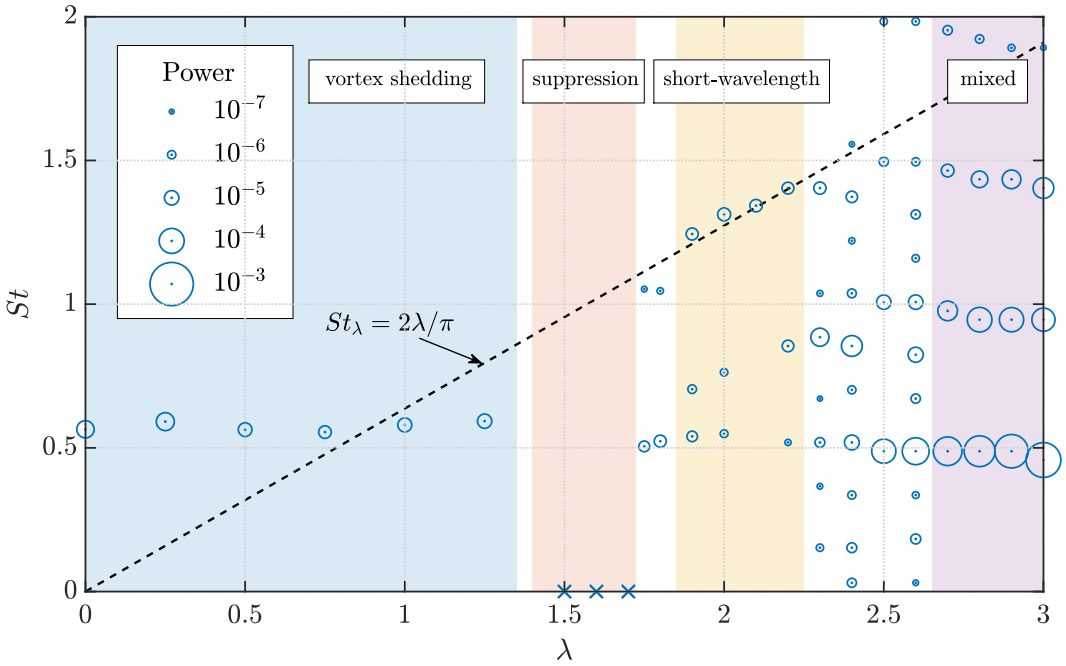

Figure 3.9: Frequency peaks from Welch's method against λ for the lift coefficient trace at $Re = 500$ and $\alpha = 25°$. Marker size is logarithmically scaled based on the integrated power from the PSD peak. Only peaks with power greater than 10^{-7} are plotted. The dashed line indicates twice the Strouhal number associated with the spin ($St = 2\lambda/\pi$). Cross markers indicate steady cases. Regions are shaded by regime, namely vortex shedding (blue), suppression (red), short-wavelength instability (yellow) and mixed vortex shedding and short-wavelength instability (purple).

resembles elliptic instabilities, specifically the (-2,0,1) principal mode (Lacaze, Ryan, and Le Dizès, 2007). We refer to this short-wavelength instability as the elliptic instability and conduct further investigation in Chapter 5.

3.2.3 Mixed wake instability and short-wavelength instability

For $\lambda \geq 2.3$, the short-wavelength instability is no longer the dominant mode. Additional lower frequency flow structures appear, predominantly at $St \approx 0.5$ and $St \approx 1$. The regular braids of the corkscrew shape are still visible in the advancing tip vortex, but now with additional vortex filaments that extend from the braids (figure 3.6). This appearance of the power spectra peak around $St = 0.5$ corresponds to periodic roll up of the trailing-edge vortex sheet that stretch spanwise between the receding and advancing tip vortices (figure 3.6). For $\lambda = 2.3$ and $\lambda = 2.4$, most energy is associated with an intermediate frequency around $St \approx 0.9$. The lower frequency content grows until the PSD peak at $St \approx 0.5$ dominates for

$2.5 < \lambda \geq 3$. Although we observe distinct PSD peaks at similar frequencies to vortex shedding and short-wavelength instability when observed in isolation, when they occur together, they interact nonlinearly, which can impact the precise frequency of the peaks. For $2.5 \lessapprox \lambda \lessapprox 3$, we see strong harmonic behavior, with many or all of the frequency peaks occurring at harmonics of the dominant frequency at $St \approx 0.5$ (figure 3.7). This suggests some coupling between the vortex shedding and short-wavelength instability, and we observe hairpin vortices of varying strength shedding from the braids of the short-wavelength instability. This mixed wake behavior is further discussed in section 5.1.2.

3.3 Conclusions and discussion

In summary, for flow over the spinning disk at $Re = 500$ and $\alpha = 25°$, increasing TSR significantly increases coefficients of lift and drag. This increase is caused by increased circulation over the disk, as a result of the vorticity added by the disk rotation, which also leads to strengthened tip vortices. By visualizing vorticity isosurfaces, we identify several distinct wake regimes for changing TSR. Vortex-shedding is suppressed at moderate TSRs, while a short-wavelength instability appears at higher TSRs. Long-time data used to characterize the wake regimes was found through a combination of impulsively started from rest and by making discrete changes in λ. We note that there was no evidence of hysteresis effects for the various bifurcations when using different means to approach the long-time behavior. However, a more thorough investigation would be required to completely rule out hysteresis effects.

Studies of Frisbee-like spinning disks (with rims and camber) at $Re = O(10^5)$ for TSRs up to one indicate negligible effect on lift and drag (Stilley and Carstens, 1972; Potts and Crowther, 2001). However, studies at higher tip speed ratios around two to three begin to show substantial increases in lift and drag, as well as increased circulation and downwash (Potts, 2005; Nakamura and Fukamachi, 1991; Higuchi et al., 2000), similar to trends observed in the present work. The magnitude of the increase in lift and drag coefficients over this range is comparable as well. This suggests that for sufficiently high TSR, increasing lift and drag due to spin is a Reynolds number independent effect, at least for $O(10^2) < Re < O(10^5)$. However, we do show increasing lift and drag even for small TSRs.

At $Re = O(10^5)$, Potts (2005) also observed increasing side force towards the receding side of the disk with increasing λ. However, the changes were over a

magnitude larger and appear to be monotonic. Potts (2005) observe a similar increase in rolling moment (banking to the receding side) at high Reynolds numbers for λ up to 3.46, although there is little to no change for $\lambda < 2$. Pitching moment trends are similar for high Reynolds number studies by Potts (2005). The differences for low TSR could be caused by a number of factors, including different Reynolds number, the different disk camber and rim geometries, and laminar versus turbulent flow.

In looking towards the application of these results to spinning disk flight, the present work shows that lift-to-drag ratio changes marginally with TSR. Angle of attack is a much stronger factor in lift-to-drag ratio. This is beneficial for being able to change TSR depending on dynamic stability requirements, without significantly impacting flight efficiency. While some trends in side force and moments are observed, the magnitude of these changes is relatively small. Note that since the disk is not accelerating in the simulations, these moment values do not include effects of gyroscopic precession that the disk would experience in free flight. Hubbard and Hummel (2000) and Hummel (2003) used in-flight Frisbee data to fit values of aerodynamic force and moment coefficients for a simple rigid-body flight model. This method produced reasonable results for short flights but are less accurate for longer flights. They showed that moment values can change significantly with flight conditions.

While there is limited data to compare the effect of thickness for $\alpha < 30°$, available literature indicates that bifurcation boundaries can shift with thickness, which is consistent with convergence studies presented in Chapter 2.3 (Chrust, Dauteuille, et al., 2015; Gao et al., 2018). As a result, while the exact transitions between the regimes identified in this work may be sensitive to disk thickness (or profile shape), the presence and qualitative features of the wake regimes are robust to changes in thickness. While further investigation would be required to understand the flow physics behind the thickness effects, we can hypothesize that it has an impact on the separation profile, particularly at leading and trailing edges of the disk. In particular, for low angles of attack where the leading edge faces more directly into the flow, this thickness will become more pronounced compared to the sharp leading and trailing edges of an infinitely thin disk. In addition, the immersed surface edge does not compare directly with a physical disk. The closest approximation may be a disk with a rounded edge, while most studies use a square edge with no rounding, which again could impact separation and boundary layer formation.

Chapter 4

VORTEX-SHEDDING SUPPRESSION BY SPIN

In the previous chapter we observed that spin could suppress vortex shedding for $Re = 500$ and $\alpha = 25°$ in the range of $1.5 \leq \lambda \leq 1.7$. In this chapter we investigate this phenomenon in more detail. We first explore select cases in the Re-α parameter space to determine the robustness of this suppression effect. This includes cases with stronger vortex-shedding and the periodic shedding with low frequency modulation (PSL) regime, as well as high angle of attack cases. We find that weakening and suppression of vortex shedding occur over a range of angles of attack and Reynolds numbers. We then proceed to analyze the wake structure in order to propose a mechanism by which vortex-shedding suppression occurs. To do this, we visualize streamlines and vortex lines to elucidate how the vorticity convection changes as TSR increases. We systematically consider flow for the rotating disk without translation, then the rotating disk with flow parallel to the disk, and finally the rotating disk at angle of attack. This helps us to build a comprehensive picture of how the circulation region changes and how the vorticity produced at the spinning-disk surface convects into the wake. This analysis shows that the disk rotation strengthens the tip vortices which in turn induces spanwise convection in the trailing-edge vortex sheet, which appears to dissipate vorticity and prevent roll up, thus leading to suppression.

4.1 Effect of spin at various Reynolds numbers and angles of attack

In this section, we present evidence for suppression in the periodic vortex shedding regime. We revisit the case first presented in Chapter 3 for $Re = 500$ and $\alpha = 25°$, which was relatively close to the critical point ($\alpha = 24.3°$). We also consider the case at $Re = 500$ and $\alpha = 30°$, which exhibits stronger vortex shedding. We also consider the effect of spin on periodic vortex shedding at $Re = 120$ and $\alpha = 60°$. In addition to vortex-shedding suppression, the high angle of attack allows for the appearance of a swirling wake instability at higher TSRs. Finally, we consider the effect of spin on the PSL wake at $Re = 300$ and $\alpha = 50°$, in which the flow has undergone a second bifurcation.

4.1.1 Vortex-shedding suppression for $Re = 500, \alpha = 25°$

For $Re = 500$ and $\alpha = 25°$, first explored in Chapter 3, we observe that the periodic vortex-shedding flow at $\lambda = 0$ was stabilized at $\lambda = 1.5$. Figure 4.1 shows the gradual modification to the wake as TSR increases from 0 to 1.5. To briefly recap, for the non-spinning case, vortex shedding is spanwise planar symmetric. The trailing-edge vortex sheet rolls up and sheds from the disk as hairpin vortices with legs extending from the tip vortices. The recirculation region, outlined by the leading-edge vortex sheet (blue spanwise vorticity isosurface), is large and extends beyond the trailing edge. For $\lambda > 0$, we see a break in spanwise planar symmetry, as the advancing tip vortex strengthens compared to the receding tip vortex. This corresponds to the receding-side leg of the hairpin vortices also disappearing, and vortex shedding is primarily on the advancing side, though the undulations can be seen to weaken. At the same time, the leading-edge vortex sheet is brought closer to the disk, signalling a decreased in size of the recirculation region. We can also notice increased positive streamwise vorticity around the leading edge as TSR increases. Eventually the flow becomes steady for $\lambda = 1.5$, featuring a distinct straight tip vortex on the advancing side, which is significantly strengthened relative to the receding-side tip vortex. Note that the lack of a visible receding-side tip vortex is a result of the contour levels used, and does not indicate that it has disappeared completely.

4.1.2 Vortex-shedding suppression for $Re = 500, \alpha = 30°$

Although the case at $\alpha = 25°$ is only just above the critical angle of attack, $\alpha_c \approx 24.3°$, we demonstrate that vortex-shedding suppression by spin is possible when the flow is further from the critical point and vortex-shedding strength is higher. To show this, we consider the flow for $Re = 500$ and $\alpha = 30°$. Figure 4.2 shows the changing vorticity isosurfaces in the wake as TSR increases from zero to two. The same trends in wake behavior persist at this higher angle of attack. The strength of vortex shedding at $\lambda = 0$ is visibly greater compared to that for $\alpha = 25°$, with larger vortical structures that persist further downstream. At $\lambda = 1$ the spanwise planar symmetry breaks, with stronger trailing-edge vortex-sheet roll up on the advancing side of the disk. At $\lambda = 2$, the flow is steady, with an unbroken tip vortex on the advancing side that is much stronger than the receding-side tip vortex. While vortex-shedding suppression is present at $\alpha = 30°$, it occurs at a higher TSR compared to the $\alpha = 20°$ case.

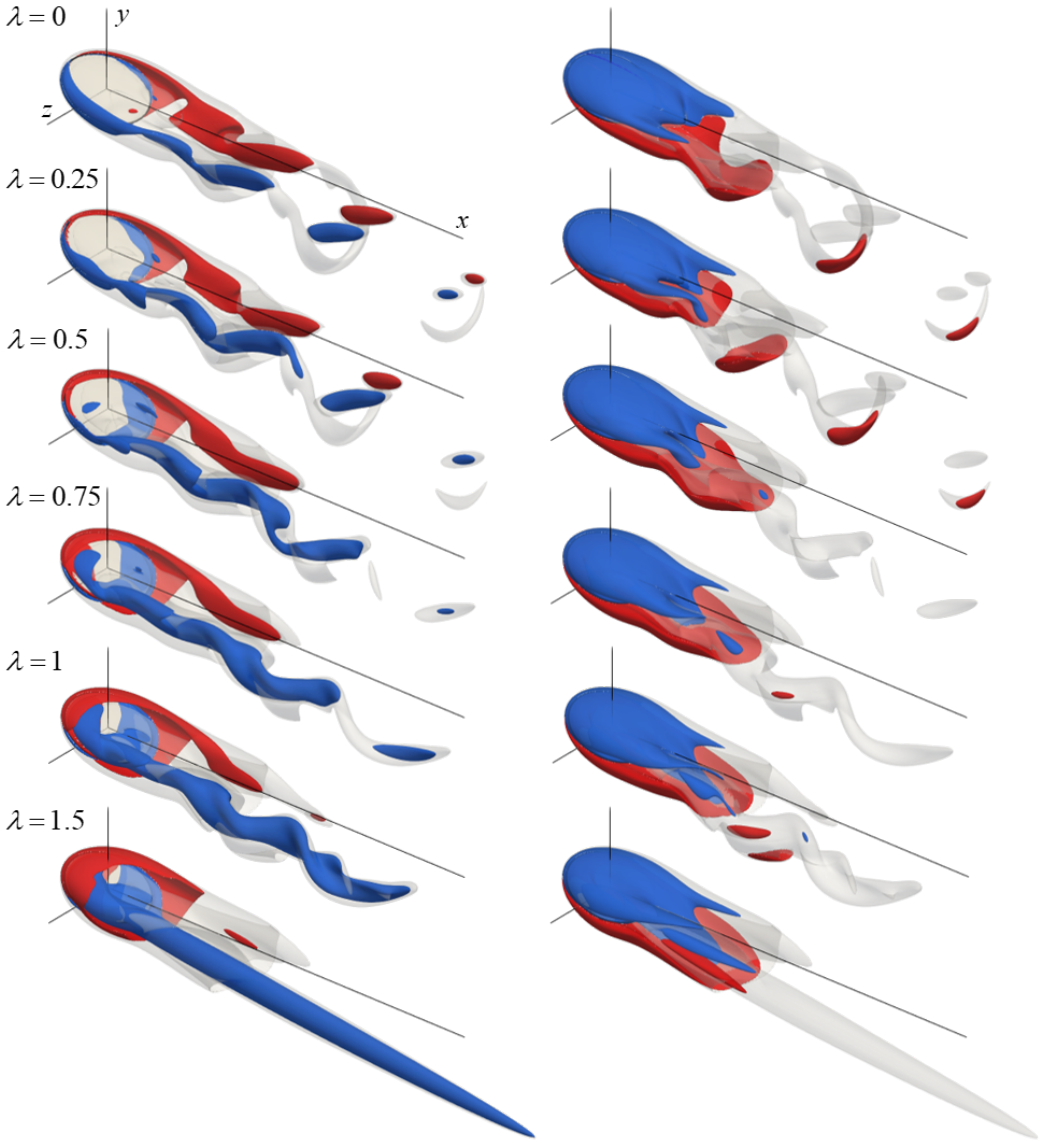

Figure 4.1: Isosurfaces of vorticity for the disk at $Re = 500$ and $\alpha = 25°$ for $\lambda = 0, 0.25, 0.5, 0.75, 1$, and 1.5. Flow is from top left to bottom right with the disk rotating clockwise from above. Semi-transparent grey isosurfaces are vorticity magnitude, $||\omega|| = 3$. Streamwise vorticity, ω_x (left column) and spanwise vorticity, ω_z (right column) are shown in opaque red and blue for positive (+3) and negative (-3) values, respectively. The x-, y-, and z-axes reference lines are $5D$, $1D$, and $1D$ long, respectively.

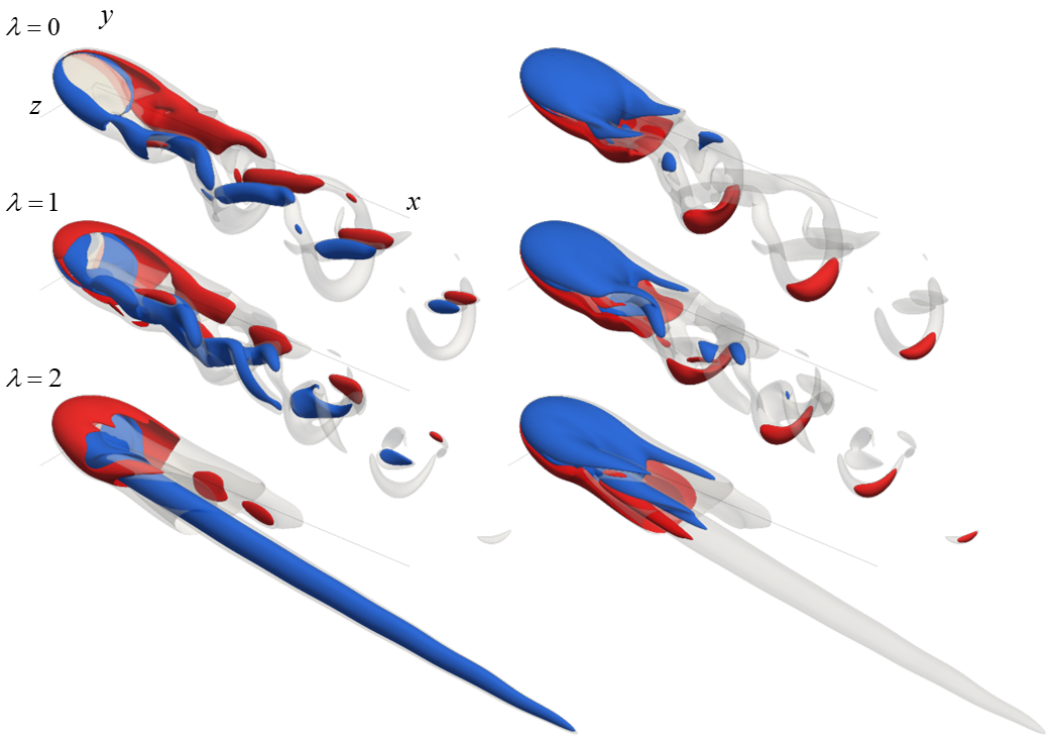

Figure 4.2: Isosurfaces of vorticity for the disk at $Re = 500$ and $\alpha = 30°$ for $\lambda = 0, 1$, and 1.5. Flow is from top left to bottom right with the disk rotating clockwise from above. Semi-transparent grey isosurfaces are vorticity magnitude, $||\omega|| = 3$. Streamwise vorticity, ω_x (left column) and spanwise vorticity, ω_z (right column) are shown in opaque red and blue for positive (+3) and negative (−3) values, respectively. The x-, y-, and z-axes reference lines are $5D$, $1D$, and $1D$ long, respectively.

4.1.3 Vortex-shedding suppression and swirling-wake instability at high angle of attack - $Re = 120, \alpha = 60°$

We consider the weakly vortex-shedding case at $Re = 120$ and $\alpha = 60°$ to explore the effect of spin at higher angles of attack. Figure 4.3 shows vorticity isosurfaces for $Re = 120$ and $\alpha = 60°$ for varying TSR. For the non-spinning case, the flow is supercritical ($Re_c = 114$) and exhibits periodic vortex shedding. Because of the low Reynolds number and proximity to the critical point, the strength of the vortical structures is much weaker than in the $Re = 500$ cases. Note that the vorticity contour levels have been decreased to reflect this. The red isosurface of z-vorticity show the trailing-edge vortex sheet beginning to oscillate before rolling up and shedding into the wake. Isosurfaces of x-vorticity show tip vortices on both the sides of the disk.

For $\lambda = 1$, the flow is steady and the trailing-edge vortex sheet does not roll up. In contrast to the non-spinning case, the advancing tip vortex is greatly strengthened

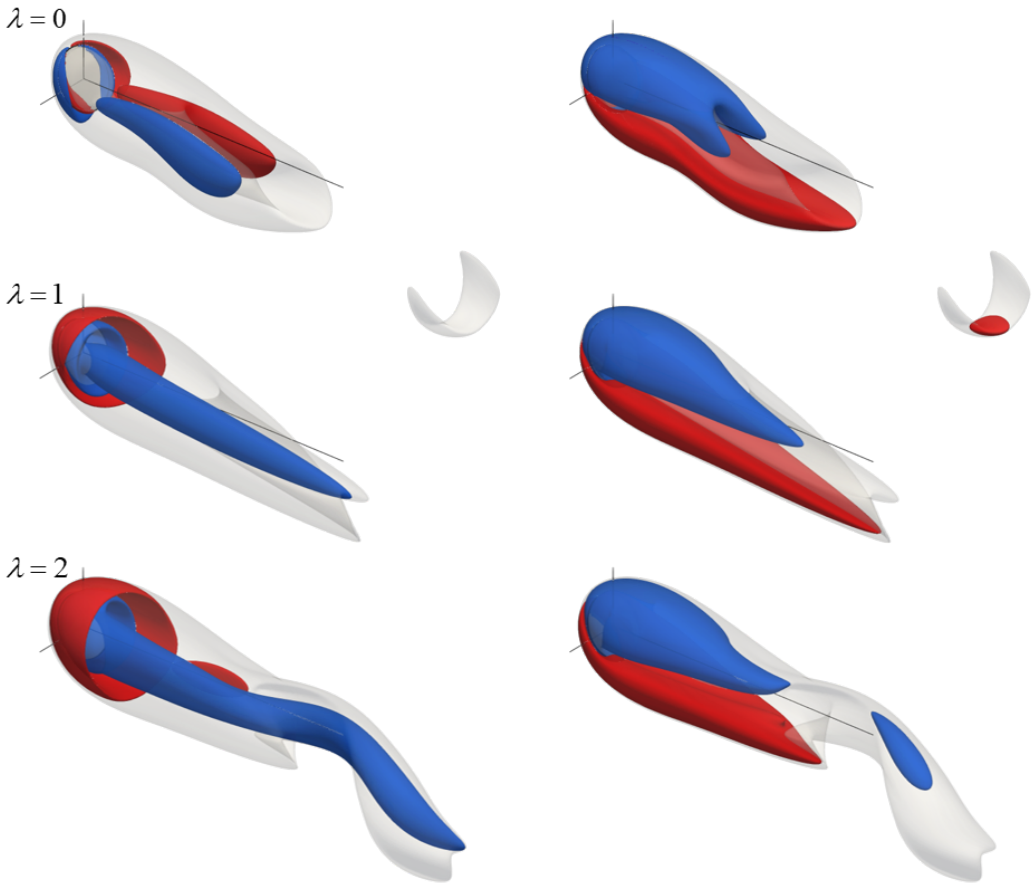

Figure 4.3: Isosurfaces of vorticity for the disk at $Re = 120$ and $\alpha = 60°$ for $\lambda = 0, 1,$ and 2. Flow is from top left to bottom right with the disk rotating clockwise from above. Semi-transparent grey isosurfaces are vorticity magnitude, $||\omega|| = 0.8$. Streamwise vorticity, ω_x (left column) and spanwise vorticity, ω_z (right column) are shown in opaque red and blue for positive (+0.8) and negative (−0.8) values, respectively. The x-, y-, and z-axes reference lines are $5D$, $1D$, and $1D$ long, respectively.

while the receding tip vortex disappears from the wake. The advancing tip vortex extends past the spanwise center plane. The steady flow is observed at both $\lambda = 0.5$ and $\lambda = 1$, indicating that weaker vortex shedding can be suppressed at lower TSRs. At $\lambda = 2$, the flow is no longer steady, and the advancing tip vortex continues to strengthen, resulting in a tail that persists further downstream. We also see another instability arise in the advancing tip vortex. The vortex core itself is displaced from its center and begins to spiral around. The frequency of the spirals is almost half that of the vortex-shedding instability.

The swirling wake structure is remarkably similar to those seen for other axisymmetric spinning bluff bodies. Kim and Choi (2002) studied flow past a sphere rotating

about its streamwise axis and found that rotation could induce a swirling wake for both steady and planar-symmetric shedding cases. Paralleled in these cases, the rotation strengthens one tip vortex over the other. Pier (2013) further characterizes and maps out the parameter space for the same configuration. In addition, Jiménez-González et al. (2014) observed a similar swirling vortical structures in flow past a spinning axisymmetric bullet-shaped body. This flow appears to arise when the tip vortices for the non-rotating case are weak, allowing for rotation to completely eliminate one of the tip vortices. As a result, a single tip vortex contains all the streamwise vorticity, and for sufficiently high vorticity, the tip vortex loses its straight configuration and begins to swirl.

While we do not conduct further analysis into the swirling-wake instability, we briefly comment on notable patterns between its appearance in these different configurations and remark on how these results may extend to similar cases. For the rotating disk and bullet-shaped body, where there is no fixed alignment for the wake with respect to the body, the wake is free to rotate with the body (Kim and Choi, 2002; Jiménez-González et al., 2014). In the case of the disk, for $\alpha < 90°$, the inclination will select an alignment plane for the tip vortices. However, this selection is increasingly tenuous as $\alpha \to 90°$. In these cases, the rotation may be strong enough to perturb the flow such that it begins to swirl. We propose that this swirling instability occurs when the body's rotation is above a critical value that overcomes the body configuration's wake alignment. This critical value will be lower as the flow configuration shows increasing axissymmetry about the freestream axis.

4.1.4 Effect of spin on the PSL region - $Re = 300, \alpha = 50°$

The vortex-shedding bifurcation is only the first in a series of bifurcations that take the flow from steady to chaotic flow. Characterizing the effect of spin beyond the single-frequency periodic vortex-shedding regime will be important for understanding how the effect of spin extends to much higher Reynolds numbers, which are supercritical with respect to this array of bifurcations. While we do not study all of the different regimes, we consider the case at $Re = 300$ and $\alpha = 50°$, which has undergone a second bifurcation and exhibits quasi-periodic shedding with low frequency modulation (PSL) for the non-spinning case (Tian et al., 2017). Tian et al. (2017) showed that this modulation is associated with a low-frequency increase and decrease in the size of the recirculation bubble, which modulates the strength of the shed vortices. As with the $Re = 500$ and $\alpha = 25°$ case, we see hairpin vortices shed from the disk, although the tip vortices are comparatively closer together and

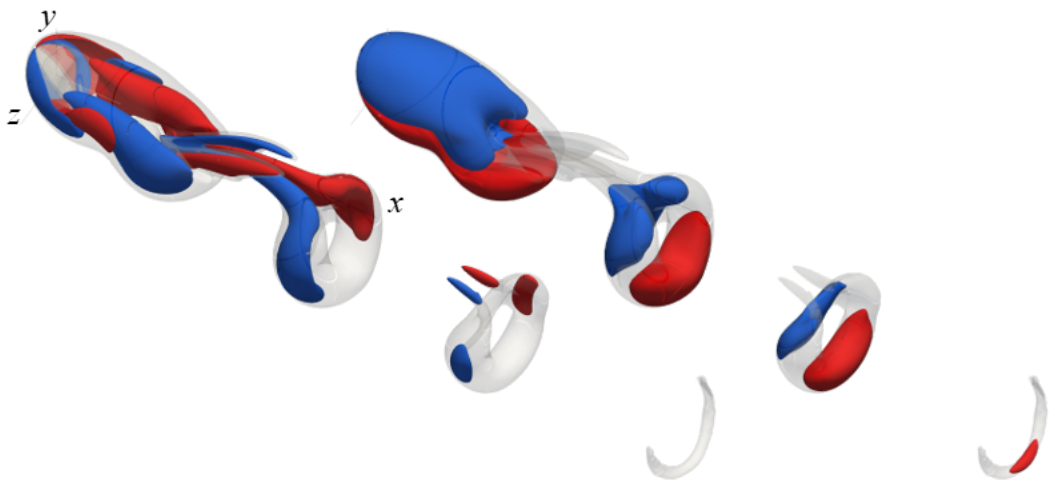

Figure 4.4: Isosurfaces of vorticity for the disk at $Re = 300$ and $\alpha = 50°$ for $\lambda = 0$. Flow is from top left to bottom right with the disk rotating clockwise from above. Semi-transparent grey isosurfaces are vorticity magnitude, $||\omega|| = 1$. Streamwise vorticity, ω_x, (left column) and spanwise vorticity, ω_z, (right column) are shown in opaque red and blue for positive (+1) and negative (−1) values, respectively.

weaker as they peel away with the trailing edge vortex sheet (figure 4.4). Since the legs are weak, the hairpin vortices gradually form vortex loops as they convect downstream, similar to observations by Kim (2009). The additional low-frequency modulation appears as a gradual strengthening and weakening of the vorticity in the hairpin vortices. Further visualizations of the PSL regime are shown for reference in appendix B.

Figure 4.5 shows the modification to the wake with increasing TSR for a higher vorticity contour level, allowing us to focus on the near-wake changes. We include top views of the same isosurfaces in figure 4.6, which helps to identify the orientation of different vortical structures. As TSR increases, spanwise planar symmetry breaks and the advancing tip vortex dominates (figure 4.6). At $\lambda = 2$, we also see a rotation of the planar alignment of the shedding, with the hairpin vortices orienting towards the advancing side of the disk rather than the trailing edge. This may arise because at higher angles of attack approaching normal flow, the selection of a plane for alignment of vortex shedding is less distinct compared to low angles of attack. In other words, for high angles of attack, the separation profile between spanwise sides is increasingly similar to that for the leading and trailing edges. In these cases, rotation can shift the alignment of vortex shedding. The low-frequency modulations are also less intense, and the amplitude of shedding remains relatively constant in time, rather than strengthening and weakening as for $\lambda = 0$. In PSL flow, the spin

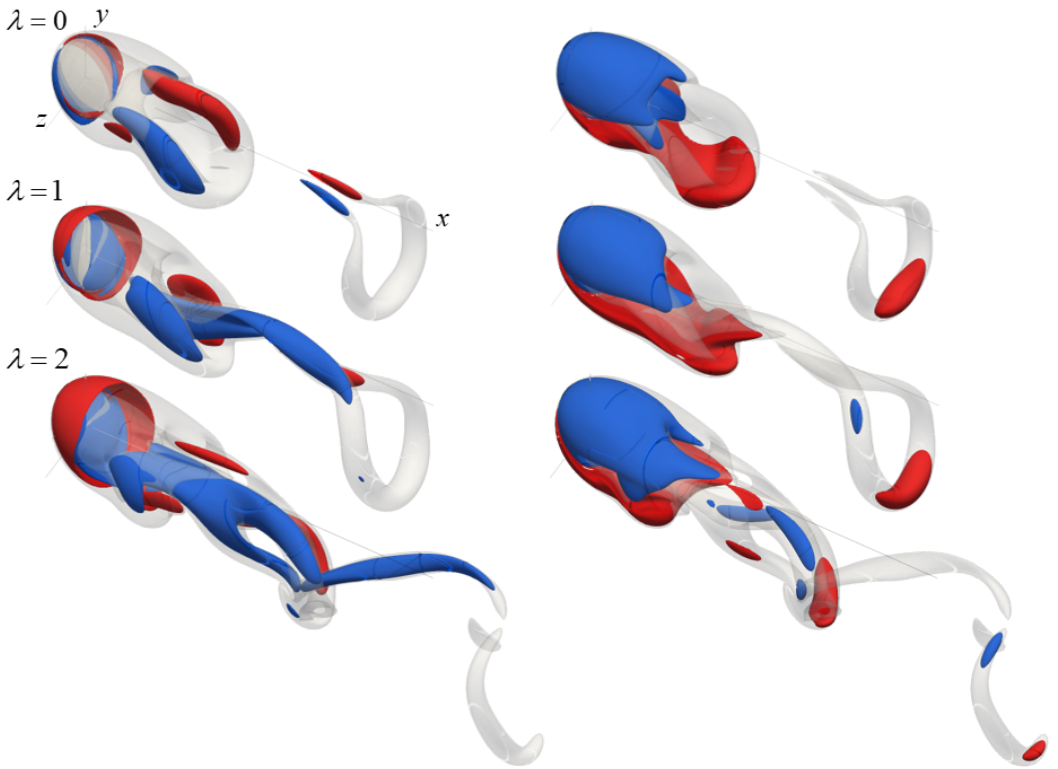

Figure 4.5: Isosurfaces of vorticity for the disk at $Re = 300$ and $\alpha = 50°$ for $\lambda = 0, 1$, and 2. Flow is from top left to bottom right with the disk rotating clockwise from above. Semi-transparent grey isosurfaces are vorticity magnitude, $||\omega|| = 3$. Streamwise vorticity, ω_x (left column) and spanwise vorticity, ω_z (right column) are shown in opaque red and blue for positive (+3) and negative (−3) values, respectively.

does not lead to vortex-shedding suppression for TSRs up to two, but it does appear to have a stabilizing effect on the low frequency modulations. Since decreased low frequency modulation is observed, this suggests that the recirculation region undergoes smaller fluctuations in size as well.

4.2 Wake structure in flow parallel to a spinning disk

The previous section showed how vortex shedding suppression occurred at various values of Re and α. Overall, spin strengthens the advancing tip vortex and leads to vortex shedding primarily on the advancing side of the disk, until eventually the roll up is suppressed completely and the flow becomes steady. We seek to gain a better understanding of the underlying mechanism behind this suppression of vortex-shedding for low to moderate TSRs. To do this, we take a closer look at how the wake structure changes with rotation. Specifically, we visualize streamlines and

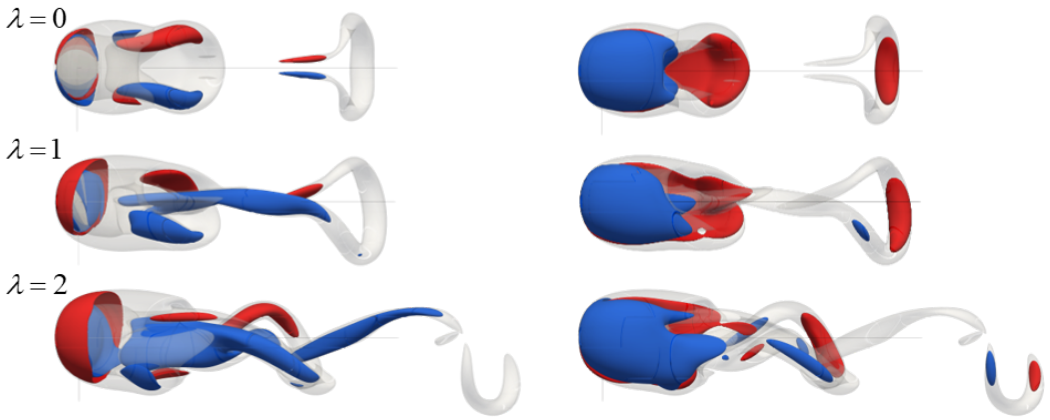

Figure 4.6: Top view of isosurfaces of vorticity for the disk at $Re = 300$ and $\alpha = 50°$ for $\lambda = 0, 1$, and 2. Flow is from top left to bottom right with the disk rotating clockwise from above. Semi-transparent grey isosurfaces are vorticity magnitude, $||\omega|| = 3$. Streamwise vorticity, ω_x (left column) and spanwise vorticity, ω_z (right column) are shown in opaque red and blue for positive (+3) and negative (−3) values, respectively.

vortex lines in the wake to discover how the rotation at the disk surface changes the distribution of vorticity in the wake. Streamlines demonstrate the topology of the recirculation region and tip vortices. Since vorticity is generated by the disk rotation, vortex lines, which are everywhere tangent to the vorticity, will reveal how vorticity convects into the wake from the disk surface. Because of the many factors at play, including disk rotation, streamwise flow and angle of attack, we deconstruct the flow and attempt to build an understanding by analyzing these factors in a modular manner. We first analyze changes in the wake structure for flow parallel to a disk as the TSR increases. We compare these observations with the flow induced by a rotating disk in quiescent flow. From von Kármán's (1921) similarity solution for the infinite rotating disk, we know that the rotating disk induces an outward, swirling flow close to the surface while drawing in fluid from the normal direction. This helps us to understand the interaction of the rotating disk flow with streamwise flow, without the added complexity of the tip vortices and vortex sheets that develop at angle of attack. Finally, we return to the case of flow over the inclined spinning disk to understand the interaction with the tip vortices and vortex sheets, allowing us to propose a mechanism for vortex-shedding suppression that is consistent with the observations.

4.2.1 Streamlines

Analyzing the changing wake for flow parallel to the disk is helpful as it avoids the presence of tip vortices and vortex sheets in the inclined case. We first study the associated streamlines with increasing TSR, and we observe significant changes to the recirculation region above the disk as well as how the flow advects into the wake. Note that this flow is symmetric about the disk plane, so we display only one side of the disk, where rotation is clockwise. We analyze streamlines within the recirculation region as well as those that pass above the recirculation region, and observe how they move into the wake. By identifying the topology in the wake, we can interpret later visualizations of vortex lines to understand how the vorticity from the disk surface distributes itself in the wake. Note that for the cases presented in this section, the flows are steady so streamlines are equivalent to pathlines.

Figure 4.7 shows the pathlines of particles that pass adjacent to the disk with increasing TSR at $Re = 100$. As a result, these streamlines for $\lambda > 0$ comprise of particles that pass through the recirculation region. For $\lambda = 0$, there is no separation so particles remain close to the disk surface throughout, with some turning due to the curved disk leading edge and resulting boundary layer formation. For $\lambda > 1$, a small recirculation region forms that increases in size with increasing TSR (figures 4.7b and 4.7c). The separation and resulting recirculation region is most pronounced on the advancing side. This is caused by the upstream movement of the disk on the advancing side of the disk, which promotes separation, whereas the streamwise movement of the disk on the receding side minimizes the boundary layer formation. As a result, close to the disk surface the fluid follows the disk spin and rotates, and this swirling flow extends into a cone-shaped recirculation region that tilts to the advancing side of the disk. The recirculation lifts flow up near the center of the disk and then brings it quickly down, leading to reattachment on the disk surface. The flow reattachment occurs earlier for higher TSR. For $\lambda = 0$, the streamlines contract slightly past the disk, whereas for $\lambda = 4$, the streamlines from the disk are expelled much further in the spanwise direction, due to the tangential velocity from the disk that pushes fluid out towards the advancing side.

Figure 4.8 shows the pathlines for particles released above the disk that pass above the recirculation region. For $\lambda = 0$, these pathlines are almost unaffected by the presence of the disk. However, for increasing TSR, the rotation draws in the fluid closer to the disk plane as it passes over the disk. Figure 4.9 shows a couple streamwise cross-section of these streamlines at different downstream distances.

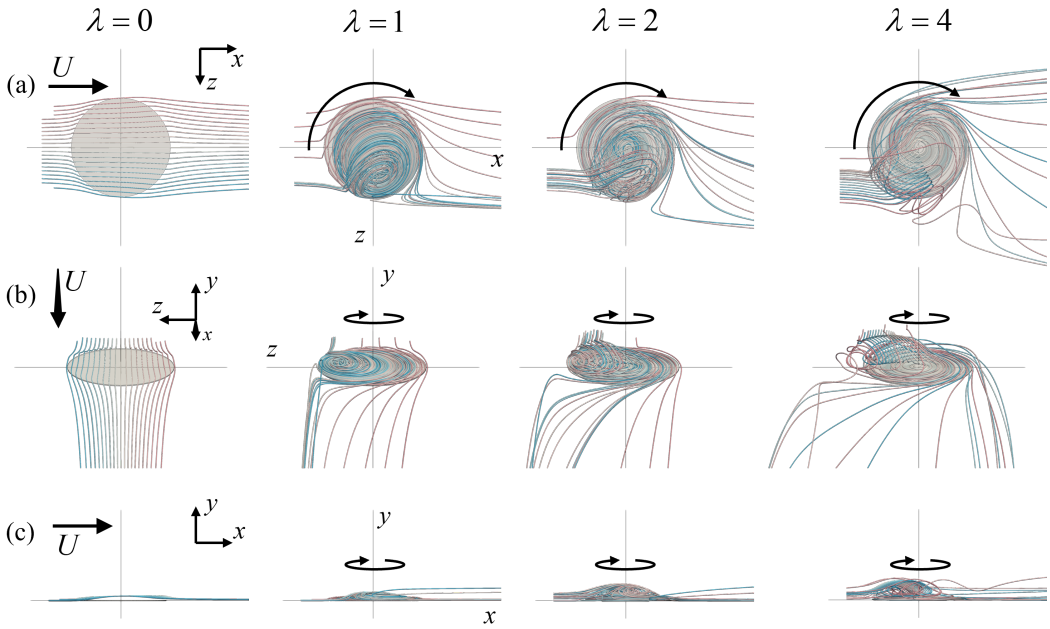

Figure 4.7: Streamlines that pass through the rake at $x = 0D$, $y = 0.05D$ and $-0.5D \leq z \leq 0.5D$, spaced every $0.05D$, for the steady flows at $Re = 100$, $\alpha = 0°$. Columns from left to right use $\lambda = 0, 1, 2$ and 4. Different rows show (a) a top view, (b) an upstream elevated view, and (c) a side view. Flow is in the $+x$ direction. Streamlines are colored by particle number. The flow is steady so streamlines are equivalent to pathlines.

These reveal more about the spanwise motion of particles. For $\lambda = 0$, the particles are slightly higher compared to their release height. This is in line with positive wall-normal velocity for a developing boundary layer. As TSR increases, the particles are brought downwards to the disk plane and also towards the advancing side of the disk. There is a clear spanwise convection in the $+z$ direction as particles move downstream. This spanwise movement is quite large in magnitude, with particles shifting past $z = +1D$ at $x/D = 2$, and shifting to almost $z = +1.5D$ by $x/D = 4$. Overall, spin creates a significant spanwise movement towards the advancing side of the disk for particles passing over the recirculation region.

We next take a look at streamlines that pass closer to the disk surface, and thus give a better indication of separation and reattachment profiles. In figure 4.10, the streamlines are initialized upstream of the disk, but close to the disk plane. As these streamlines approach the disk, they conform to the flow around the recirculation region. For $\lambda > 1$, the flow is first accelerated to the receding disk side when passing over the first half of the disk, and then is accelerated to the advancing side as it passes over the second half of the disk, matching the velocity on the disk surface.

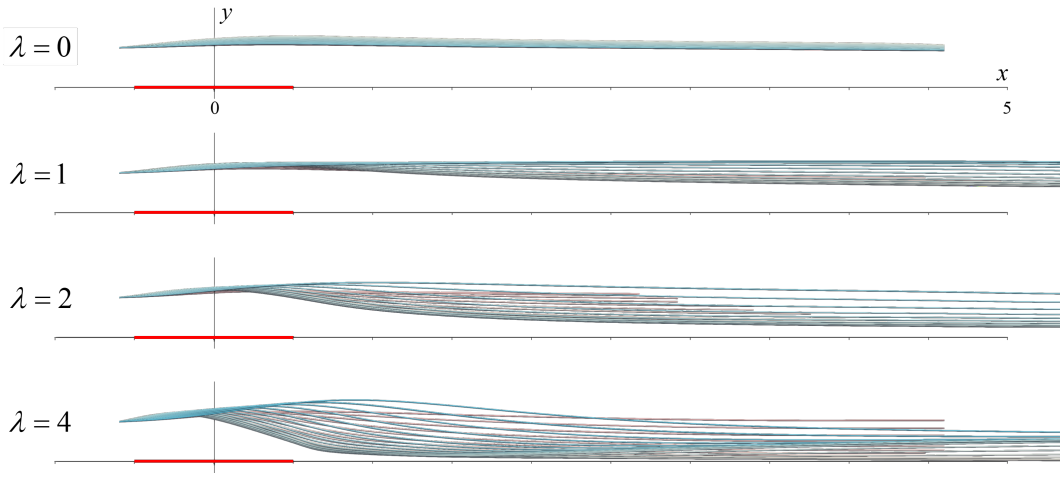

Figure 4.8: Side view of a rake of streamlines initialized at $x = -0.6$, $y = 0.25$ and $-0.5 \leq z \leq 0.5$, spaced every $0.05D$ across the z extent of the computational domain, for $Re = 100$, $\alpha = 0°$ and changing λ. Streamlines are colored by particle number. The flow is steady so streamlines are equivalent to pathlines.

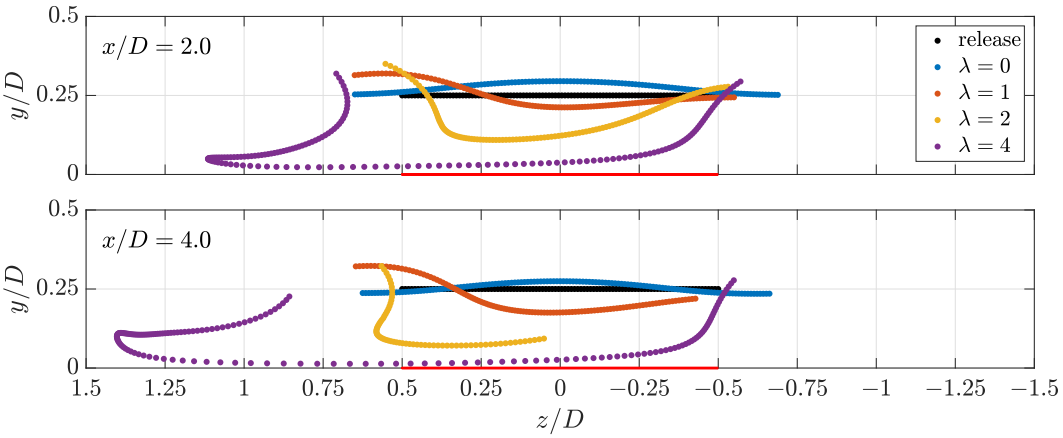

Figure 4.9: Streamwise plane showing the intersection of streamlines on the $x/D = 2$ plane (top) and $x/D = 4$ plane (bottom) when released at $x/D = -0.6$, $y = 0.25$ and across the z extent of the computational domain for $Re = 100$, $\alpha = 0°$ and changing λ. The disk profile is shown in red. The flow is steady so streamlines are equivalent to pathlines.

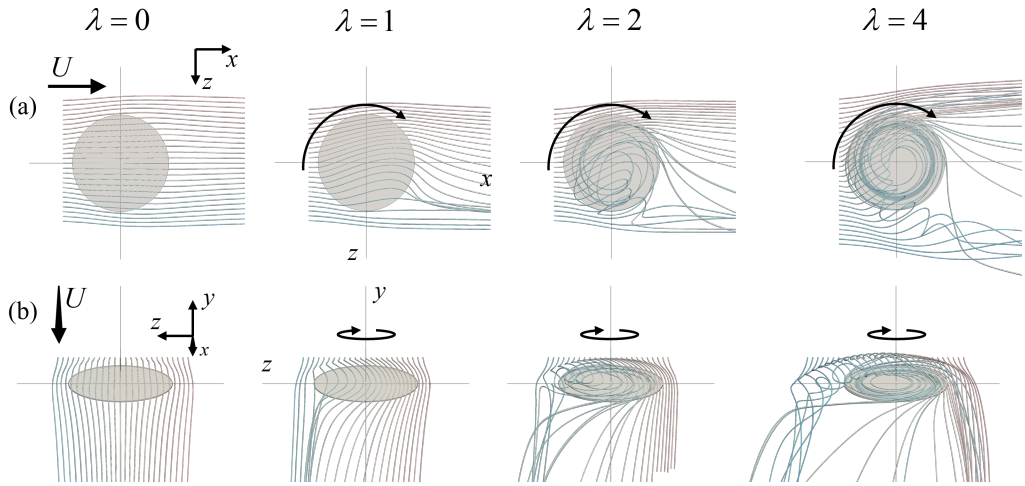

Figure 4.10: Streamlines from a rake initialized at $x = -0.6$, $y = 0.05$, spaced every 0.05D across the z extent of the computational domain, for $Re = 100$, $\alpha = 0°$. Columns from left to right use $\lambda = 0, 1, 2$ and 4. Different rows show (a) a top view, and (b) an upstream elevated view. Flow is in the $+x$ direction. Streamlines are colored by particle number. The flow is steady so streamlines are equivalent to pathlines.

We again see the reattachment of the flow after the separation region. For $\lambda = 4$, we see a very strong recirculation region that extends beyond the sides of the disk. This gives rise to two connected vortical structures, one on either spanwise side, which resemble tip vortices in the sign of their streamwise vorticity content. Overall the streamlines show that the disk rotation induces a spanwise-outward flow close to the disk plane. Fluid passing above the disk is brought abruptly downwards to replace this fluid. We see that the recirculation region naturally tilts to the advancing side of the disk, such that on the advancing side, flow is upstream at the surface of the disk, and downstream towards the top of the recirculation region. This allows flow passing over the disk to be in the same direction as the flow in the recirculation region. A clear pattern emerges where the rotation of the disk creates a recirculation region that points towards the advancing side of the disk and connects to a vortical structure akin to a tip vortex. Much of the flow is directed into this vortex.

4.2.2 Vortex lines

With an understanding of the changing recirculation region and flow in the wake, we turn to analyzing the arrangement of vortex lines. Vortex lines illuminate flow structures such as the tip vortices and the trailing-edge vortex sheet. Since vortex lines are everywhere tangent to the local vorticity vector, they indicate the contribution of vorticity generated at the disk surface contributes to different negative

or positive components of vorticity in the wake. While this flow is not inviscid and we observe some viscous dissipation of vorticity, we can drawn on Helmholtz's theorems as a basis for understanding the vortex line motion. They state that vortex lines must extend to the fluid boundaries or form a loop. In this case, vortex lines begin on either side of the disk surface due to the rotation. In a purely rigid-body rotating flow, vortex lines are parallel to the axis of rotation and extend normal from the surface. For the finite disk, these vortex lines extend into the wake and eventually loop back to end on the other side of the disk. Figure 4.11 shows the arrangement of vortex lines for a rotating disk with and without freestream flow. For additional configurations of the vortex lines from the disk surface, see appendix C. The loops are symmetric about the disk plane. For the non-spinning case, loops leave the surface on one side, extend out past the disk radius and loop back to the other side of the disk, forming a closed loop. The loops swirl around the disk since the angular velocity of the flow decays beyond the disk radius.

When streamwise flow is introduced, we still see the overall loop structure and swirling configuration, with some added modifications. Vortex loops on the upstream side of the disk are concentrated around the leading edge, while vortex loops towards the trailing edge are convected downstream into the wake. The vortex lines that proceed downstream on the advancing side consist of negative streamwise vorticity and concentrate themselves in the vortical tube emerging from the recirculation region. Note that the sign of streamwise vorticity depends on the orientation of the vortex line. Vortex lines that originate at the top disk surface have negative streamwise vorticity when oriented downstream, as a result of the clockwise disk rotation (when viewed from above). When the vortex lines orient themselves upstream, as in the case of some of the vortex lines that have turned back upstream, then they have positive streamwise vorticity values. Note that if we were to take a look at the bottom side of the disk, the vorticity signs will be opposite, since the bottom side of the disk introduces positive streamwise vorticity into the flow.

4.3 Wake structure in flow over an inclined spinning disk

Overall, from the parallel flow simulations, we observed that disk rotation creates a recirculation region that orients itself to the advancing side of the disk, while increasing the downwash over the top of the disk helps to bring the leading-edge vortex sheet closer to the disk. Vorticity from the top side of the disk contributes to negative streamwise vorticity as it convects downstream, and predominantly concentrates into a vortex on the advancing side of the disk. We remark that this is

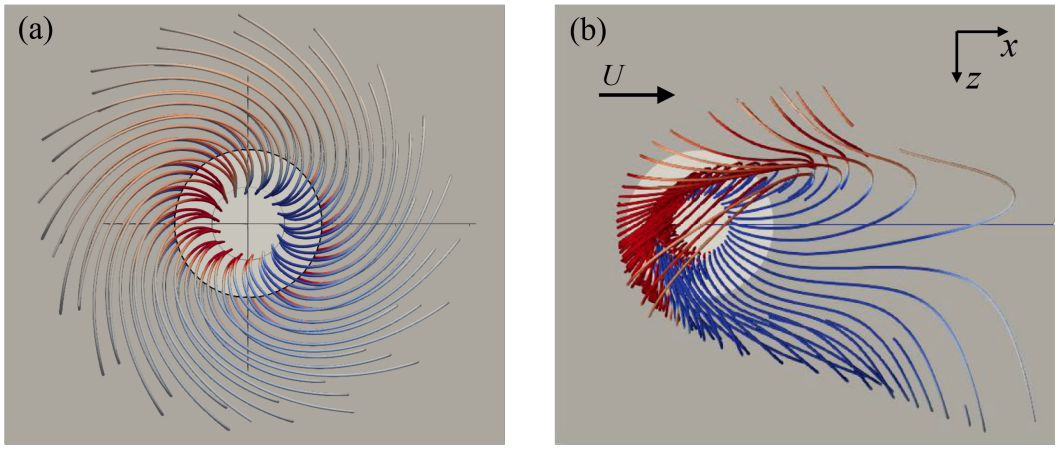

Figure 4.11: Top view of vortex loops from the disk surface for (a) $Re_\omega = 100$ and (b) $Re = 100$, $\lambda = 4$, and $Re_\omega = 400$). Vortex lines are colored by x-vorticity.

the same sign of streamwise vorticity as in tip vortices that form on the advancing side of the disk for inclined flow. We will see that this is important for allowing the vorticity from the disk to strengthen the advancing tip vortex. We now apply the same streamline and vortex line analysis from section 4.2.1 for the case with disk inclination and describe the effect of disk rotation on the wake structure. There are several connections to the case of flow parallel to the disk, although inclination leads to separation at the trailing edge even without spin, as well as tip vortices from the sides of the disk. As we consider the inclined disk case at $Re = 500$ and $\alpha = 25°$, we keep in mind the vorticity signs from the top and bottom surfaces, which are significant for how they interact with tip vortices and vortex sheets.

4.3.1 Streamlines

Returning to the case of inclined flow at $Re = 500$ and $\alpha = 25°$, at $\lambda = 0$, there is already a recirculation region because of the separation at the leading edge. The pressure difference between the top and bottom surfaces gives rise to counter-rotating tip vortices on either side of the disk, which are not present for the parallel flow case. Again, we analyze streamlines within the recirculation region. Because of the angle of attack, it is important to look at streamlines that pass both above and below the disk, as these are no longer symmetric as in the parallel flow case, and they illuminate different parts of the wake structure. Figure 4.12 shows the pathlines for particles starting upstream and passing both above and below the disk. Note that in this case, the flow is steady so streamlines and pathlines are equivalent. We see that streamlines pass over the recirculation bubble. Because of the strong

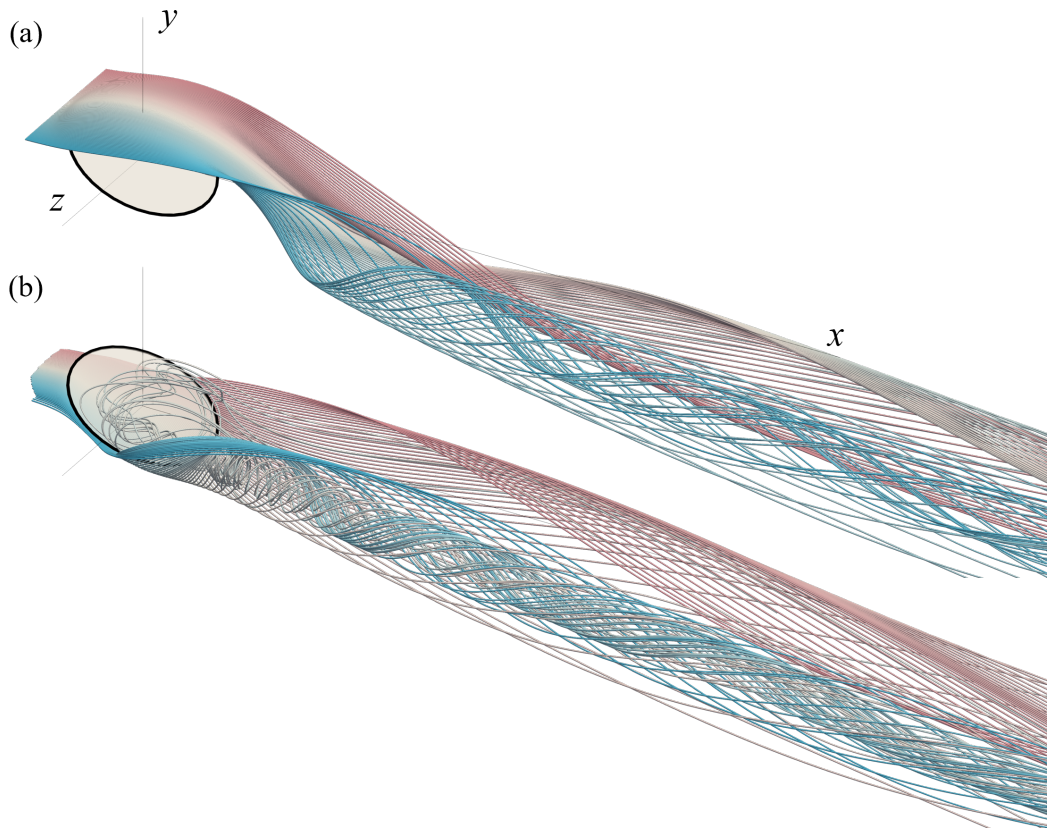

Figure 4.12: Pathlines for the steady flow for $Re = 500$, $\alpha = 25°$ and $\lambda = 1.5$. Particles pass through every $0.01D$ along (a) a spanwise line with a parallel distance of $0.1D$ from the disk leading edge and (b) a spanwise line below the disk with a normal distance of $0.05D$. Flow is from top left to bottom right and streamlines are colored by particle.

tip vortices and resulting downwash, the streamlines are swept towards the center spanwise plane and also brought quickly downwards. They spread into the top side of the trailing edge vortex sheet and are also entrained into each tip vortex, causing them to swirl. None of the streamlines end up in the recirculation region but instead continue downstream in the tip vortices.

For streamlines passing close to the pressure side of the disk, most particles are entrained into the tip vortices as well. As in the case of flow parallel to the disk (figure 4.9), we see significant spanwise-outward velocity in the trailing-edge vortex sheet, induced by the entrainment of the tip vortices. However, there is a narrow region of fluid that is entrained into the advancing tip vortex and then proceeds to swirl upstream into the recirculation region. Ultimately, these streamlines exit the recirculation region primarily on the receding side of the disk, where the disk velocity is in line with the freestream velocity. This behavior indicates that there

is a boundary in the advancing tip vortex, slightly downstream of the disk, that separates fluid that travels upstream into the recirculation bubble, and fluid that proceeds downstream in the tip vortex. Figure 4.13 distinguishes between these sets of streamlines for a clearer view. We see that a narrow region of upstream points are entrained into the advancing tip vortex and pulled upstream into the recirculation region. Meanwhile points towards the advancing side are entrained into the advancing tip vortex but proceed downstream. Points on the receding side are much more greatly diffused in the trailing edge vortex sheet and end up entrained in both the advancing and receding tip vortices. These visualizations also show how the rotation induced by the advancing tip vortex is much stronger than that in the receding tip vortex.

To grasp the structure of the recirculation bubble and how this affects the distribution and advection of vorticity in the wake, we examine streamlines that all pass through the recirculation region, shown in figure 4.14. While the recirculation bubble is spanwise symmetric in the non-spinning case, we see here that the recirculation region elongates along the advancing side of the disk, while shortening on the receding disk side. This follows from the differential in local Reynolds number on either spanwise side of the disk due to the rotation (higher on the advancing side and lower on the receding side), as seen in the case of flow parallel to the disk (figure 4.7). The recirculation region takes on a cone-like shape that shares many similarities with the flow profile caused by rotating disk in quiescent flow (non-translating), which exhibits a spiralling, viscous pump action that draws in fluid towards the rotating disk. This cone of swirling fluid has its nose shifted into the advancing tip vortex. This is a result of the match in orientation of rotation in both the recirculation region and the advancing tip vortex (streamwise negative). The flow in the recirculation region swirls around and towards the disk. Flow in this region comes predominantly from a narrow upstream region of fluid that passes below the disk, is brought above the disk by the advancing tip vortex, and spirals inward to the disk surface. Most particles are then released near the disk surface on the receding side.

4.3.2 Vortex lines

The rigid-body rotation of the disk generates vorticity on both the pressure and suction surfaces. Examining the resulting vortex lines at $Re = 500$ and $\alpha = 25°$ demonstrates how vorticity convects in the wake for inclined flow. The vortex lines from the parallel flow case in section 4.2.2 revealed that vorticity from the top

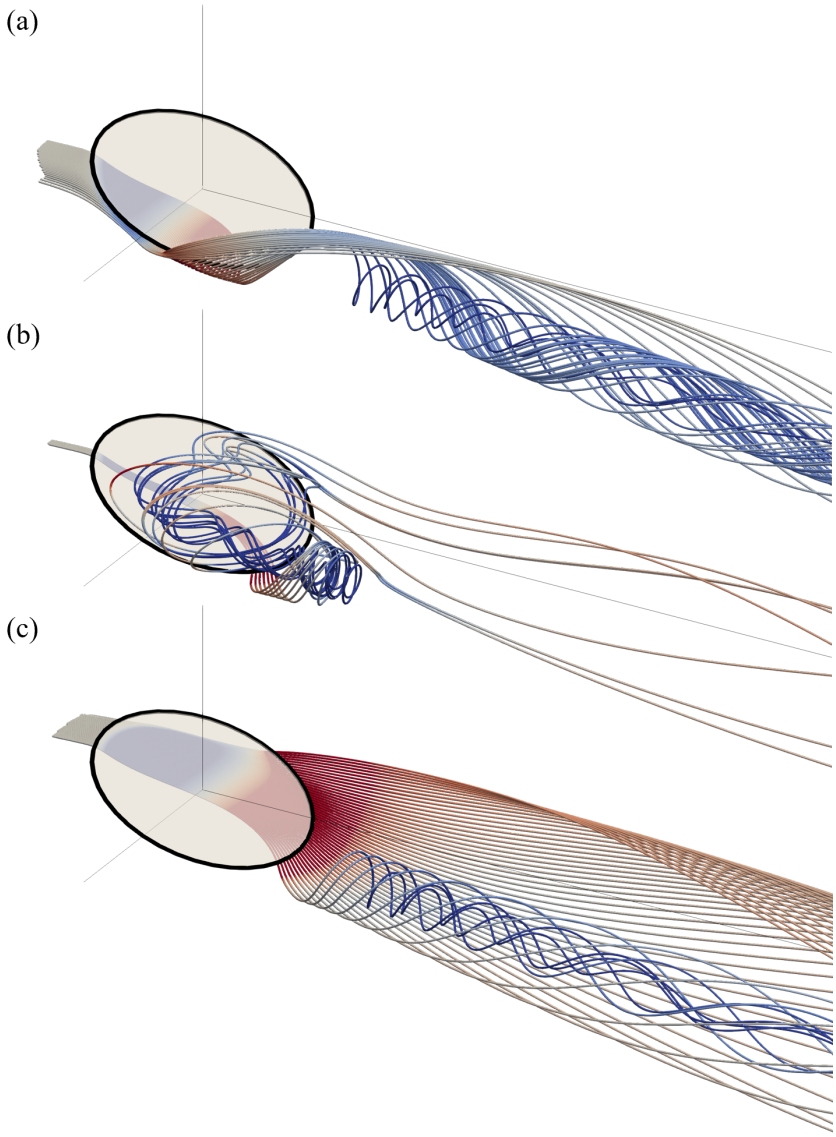

Figure 4.13: Pathlines below the disk for the steady flow for $Re = 500$, $\alpha = 25°$, and $\lambda = 1.5$. Particles pass through every $0.01D$ along a spanwise line below the disk with a normal distance of $0.05D$, with (a) $0.1D < z < 0.5D$, (b) $0D < z < 0.06D$, and (c) $-0.5D < z < 0D$. Flow is from top left to bottom and streamlines are colored by streamwise vorticity, ω_x.

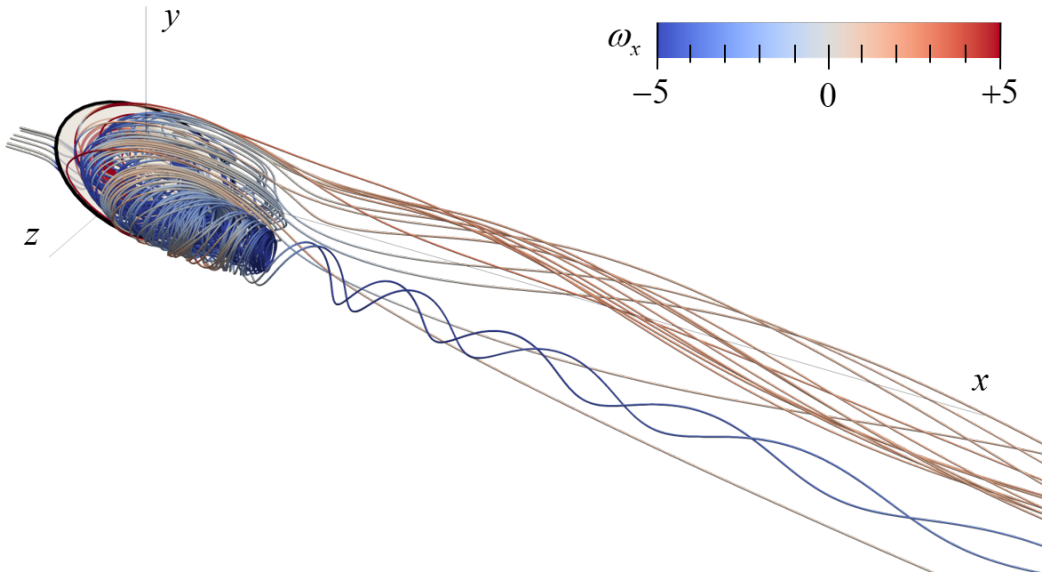

Figure 4.14: Pathlines below the disk for the steady flow for $Re = 500$, $\alpha = 25°$ and $\lambda = 1.5$. Particles are initialize in a ring parallel to the disk with a normal distance $0.1D$ and diameter $0.5D$. Flow is from top left to bottom and streamlines are colored by streamwise vorticity, ω_x.

disk surface contributed to negative streamwise vorticity in the wake, primarily on the advancing side of the disk, following the alignment of the recirculation region towards the advancing side of the disk as well. We channel this understanding to interpret the vortex lines in the wake of flow for the rotating disk at $Re = 500$, $\alpha = 25°$, and $\lambda = 1.5$.

Figure 4.15 displays two sets of vortex lines, one showing how the vortex lines extend into the wake and eventually loop back towards the disk (top image in figure 4.15) and another that displays just the vortex lines as they extend into the wake, so that we can see them unobstructed (bottom image in figure 4.15). Following the orientation of the recirculation cone into the advancing-side tip vortex, the vortex lines originating from the top surface of the disk extend directly into the advancing tip vortex. On the other hand, vortex lines from the bottom surface are more diffused in the wake, distributed into both the receding tip vortex and the leading-edge and trailing-edge vortex sheets. The spanwise-outward motion seen from the streamlines in figure 4.12 helps to entrain vorticity from the trailing-edge vortex sheet around the advancing tip vortex, and we see these vortex lines circle the vortex core. While this configuration may seem complicated at first, we can make comparisons to the non-spinning case to help explain this geometry. For the non-spinning disk flow

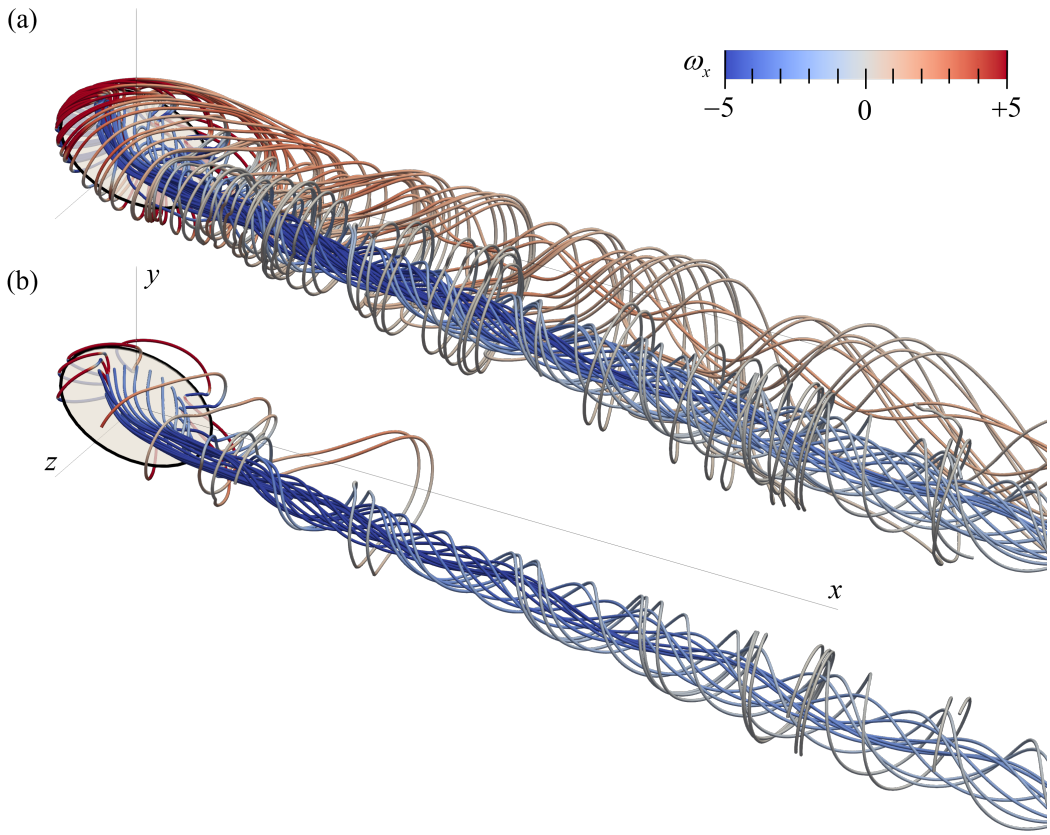

Figure 4.15: Vortex lines extending from the suction surface of the disk for the steady flow for $Re = 500$, $\alpha = 25°$, and $\lambda = 1.5$. All vortex lines are initialized in a ring parallel to the disk with a normal distance $0.1D$ and diameter $0.5D$. Flow is from top left to bottom and streamlines are colored by streamwise vorticity. The maximum length of vortex lines is (a) $40D$ and (b) $10D$. In (b) only the vortex lines primarily in the advancing tip-vortex core are revealed while in (a), longer vortex lines eventually loop back towards the disk. Vortex lines are colored by streamwise vorticity, ω_x.

with vortex shedding, vortex lines follow the hairpin-vortex loops. The strengthened advancing tip vortex for the spinning case causes the ends of these vortex loops to become entrained and swirl around the advancing tip vortex, as seen by the vortex loops that circle around the advancing tip-vortex core.

4.4 A mechanism for vortex shedding suppression by vorticity advection

This picture of the recirculation region and how vortex lines distribute in the wake help us to understand how the vorticity generated from the disk distributes itself in the wake and leads to vortex-shedding suppression. While the magnitude of vorticity generated from the disk is the same for both surfaces, their orientation and

how they advect into the wake differ greatly. Vortex lines from the top surface have the same streamwise sign as the advancing tip vortex, while vortex lines from the bottom disk surface have the same streamwise sign as the receding tip vortex. Since vortex lines from the top surface enter into the cone-shaped recirculation region, they are then fed into the advancing tip vortex directly, greatly strengthening the advancing tip vortex. However, vorticity from the bottom disk surface enter the wake from outside the recirculation region and so are more distributed around the tip vortices and trailing-edge vortex sheet. This leads to the behavior observed in the vorticity-isosurface visualizations, where the advancing tip vortex dominates and the receding tip vortex is more diffuse. The increased circulation in the tip vortices increases downwash above the disk, so the leading edge vortex sheet hugs closer to the disk (figure 4.1). It also induces a significant spanwise-outward flow in the trailing edge vortex sheet, helping to advect vorticity in the trailing edge vortex sheet outwards. This diffusion of vorticity in the trailing edge vortex sheet prevents its roll up, thus suppressing roll up.

4.5 Unsteadiness at high tip-speed ratios

While we have focused on the changes in wake structure from periodic vortex shedding to steady flow, we have also seen that there are additional instabilities at high TSRs. Revisiting figures 3.6 and 3.9, we recall that for high TSRs beyond the steady region ($\lambda \gtrapprox 1.75$), we saw unsteadiness in the wake. The high-frequency content is associated with elliptic instability that will be discussed in more detail in Chapter 5. Meanwhile the low frequency content corresponds to the reappearance of vortex shedding, which continues to grow with TSR. This means that rotation serves to modulate the flow from subcritical to supercritical with respect to the vortex shedding instability. A potential explanation for the reappearance of vortex shedding is related to the addition of vorticity into the wake by the disk rotation. Previously, we discussed that some of this vorticity enters the tip vortices, which in turn helps them to dissipate vorticity in the trailing-edge vortex sheet before it rolls up. At the same time, some vorticity from the bottom side of the disk ends up in the trailing edge vortex sheet (figure 4.15). As TSR increases, the strength of the trailing-edge vortex sheet increases as well. Whether or not the trailing-edge vortex sheet rolls up may then be a function of the competing effects of the spanwise convection of vorticity out of the trailing-edge vortex sheet and the addition of vorticity into the trailing-edge vortex sheet.

4.6 Conclusions and Discussion

In summary, we observe that disk rotation helps to reduce and, in some cases, suppress vortex shedding in flow over an inclined spinning disk. This occurs over a range of supercritical Re-α combinations, including into higher bifurcations such as the quasi-periodic vortex-shedding (PSL) flow, where low-frequency modulations are inhibited. The TSR required to suppress vortex shedding differs depending on the original strength of vortex shedding in the non-spinning case. Streamline and vortex line analyses show that, as λ increases, more vorticity is generated at the disk surface and ultimately advected into the wake. The rotation induces a cone-shaped recirculation region that orients itself into the advancing tip vortex, greatly strengthening the advancing tip vortex. This induces a spanwise-outward flow in the trailing-edge vortex sheet, causing it to be entrained into the tip vortices. This serves to dissipate vorticity from the trailing-edge vortex sheet, preventing it from rolling up and resulting in weakened or suppressed vortex shedding. At higher TSRs, the vortex-shedding instability reappears, which may be caused by the disk rotation strengthening the trailing-edge vortex sheet beyond the ability of the tip vortices to dissipate it. Overall, disk rotation causes two competing effects: (1) the increase in vorticity in the tip vortices, especially the advancing tip vortex, which helps to dissipate the trailing edge vortex sheet, and (2) the addition of vorticity into the trailing-edge vortex sheet. The stronger effect determines whether or not vortex shedding occurs.

This vortex-shedding suppression and subsequent destabilization by spin is not unique to the case of the spinning disk. Kim (2009) studied flow past a sphere rotating in the transverse direction and observed that moderate rotation rates suppressed vortex shedding while even higher rotation rates could destabilize the flow and cause vortex shedding to appear again. Poon et al. (2010) explored different axes of rotation between streamwise and transverse rotation, observed similar phenomenon for a range of rotation axes. Similarly, Kang, Choi, and Lee (1999) found that in two-dimensional flow past a circular cylinder, rotation could suppress vortex shedding and lead to a steady flow. By studying higher TSR regimes for the same configuration, Mittal and Kumar (2003) observed a second critical rotation beyond which the flow was unsteady. Karabelas et al. (2012) also observed suppression of vortex shedding in turbulent two-dimensional flow over a rotating circular cylinder for $Re = 5 \cdot 10^6$, Given similarities in the trends and wake structures, it is possible that the underlying mechanisms in these various flows may be related as well, with the rotation strengthening the tip vortices and helping to dissipate vorticity before

it rolls up. Further study would be required to understand this non-monotonic behavior, which is relevant to a variety of rotating bluff-body flow configurations.

Chapter 5

ELLIPTIC INSTABILITY IN TIP VORTICES

In this chapter, we consider spinning disk flow at $Re = 500$ and $\alpha = 25°$ for high TSRs ($\lambda \geq 1.9$). At these TSRs, a short-wavelength instability appears, both in isolation and in conjunction with other instabilities. We use spectral proper orthogonal decomposition (SPOD) to isolate the instabilities in the flow and characterize their features. We find that the short-wavelength instability shows remarkable qualitative and quantitative similarities to the $(-2, 0, 1)$ principal mode of elliptic instability. To make comparisons, we model the tip vortices as a pair of counter-rotating Batchelor vortices and estimate the flow parameters that are relevant to elliptic instability. Our parameter estimates are consistent with instability of the $(-2, 0, 1)$ principal mode. We also observe frequency lock-in between the disk rotation and the short-wavelength instability, which suggests the importance of disk rotation for forcing the short-wavelength instability.

5.1 Short-wavelength instabilities at high tip-speed ratio

5.1.1 Isolated short-wavelength instability

While vortex-shedding is stabilized for low to moderate TSRs, higher TSRs excite a short-wavelength instability, see for example figure 5.1. This short-wavelength instability appears as a corkscrew-shaped double-helical twisting of the vorticity isosurfaces. It is particularly distinct for $1.9 \leq \lambda \leq 2.2$, but persists into higher TSRs as well. At $\lambda = 1.8$, just above the steady range, we see the onset of the instability in the advancing tip vortex, with a shallow corkscrew shape starting to take hold. At $\lambda = 1.9$, this corkscrew or double-helical shape is distinct with regular "braids" of vorticity twisting around themselves. The wavelength of this instability is on the same order as the inter-tip-vortex distance, making it wavelength relative short relative to the wavelength of vortex shedding, which is about 2-3 times greater.

As λ increases further, the shape is maintained but the wavelength decreases visibly, corresponding to a gradual increase in frequency as well (figure 3.9). We can observe the grooves of the corkscrew deepening as λ increases. As a result of the decreasing wavelength, the helix angle decreases as well, and we can see some of the vortical structures in the braids orienting themselves increasingly in the spanwise direction, leading to stronger spanwise vorticity around the advancing tip vortex (figure 5.1).

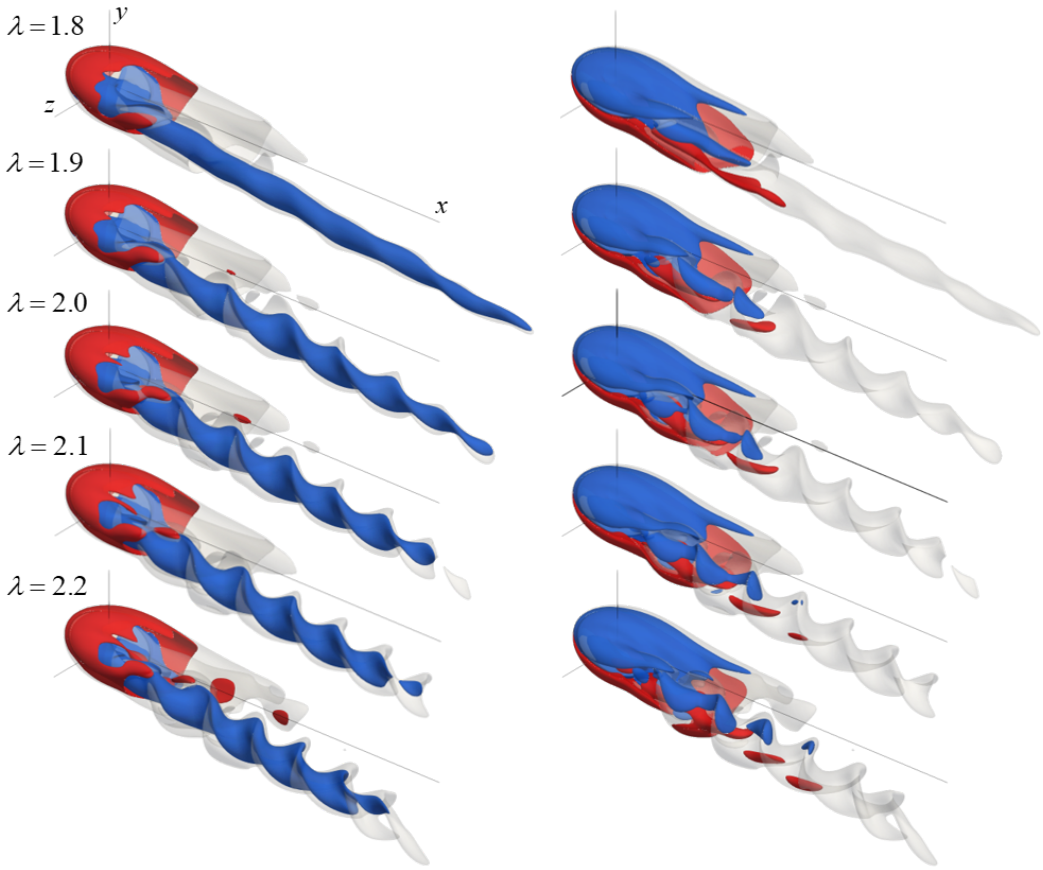

Figure 5.1: Isosurfaces of vorticity for the disk at $Re = 500$ and $\alpha = 25°$ for $\lambda = 1.8, 1.9, 2.0, 2.1$ and 2.2. Flow is from top left to bottom right with the disk rotating clockwise from above. Semi-transparent grey isosurfaces are vorticity magnitude, $||\omega|| = 3$. Streamwise vorticity, ω_x (left column) and spanwise vorticity, ω_z (right column) are shown in opaque red and blue for positive (+3) and negative (−3) values, respectively. The x-, y- and z-axes reference lines are $5D$, $1D$ and $1D$ long, respectively.

This short-wavelength instability closely resembles the elliptic instability, which has been extensively studied in the literature and will be described in detail in section 5.3.

5.1.2 Mixed short-wavelength instability and vortex shedding

While the short-wavelength instability is dominant in the range of $1.9 \leq \lambda \leq 2.2$, for $\lambda > 2.3$, the vortical structures in the wake become more complicated, although they still exhibit strongly periodic behavior (figure 3.9). Figure 5.2 shows the modification to the wake with increasing TSR for $2.3 \leq \lambda \leq 3$. We refer back to figure 3.9 to track the changes in frequency content over this range as well. For $1.9 \leq \lambda \leq 2.2$, the flow is largely monochromatic, with the short-wavelength elliptic

instability providing the dominant frequency content at $St \approx 1.4$. For $\lambda \geq 2.3$, we see additional lower frequencies appear and take over as the highest energy peaks. The dominant frequency for $\lambda = 2.3$ and $\lambda = 2.4$ is $St \approx 0.9$. Meanwhile for $2.5 \leq \lambda \leq 3$, the dominant frequency is $St \approx 0.5$, which is close to the vortex shedding frequency at low TSR (figure 3.9). This results in a transitionary region for $2.3 \leq \lambda \leq 2.6$ where the spectra are quite colorful, with many distinct peaks appearing. Visually, we are still able to see the corkscrew shape of the short-wavelength instability, though we have the addition of more complex vortical structures. The grey isosurfaces of vorticity magnitude reveal non-planar-symmetric vortex shedding that extends from the advancing tip vortex and loops partially towards the receding side. This vortex shedding is associated primarily with the low frequency peak at $St \approx 0.5$.

It is noteworthy that the frequency of the intermediate peak ($St \approx 0.9$) is equal to the difference between the high frequency ($St \approx 1.4$) and low frequency values ($St \approx 0.5$), which are associated with the short-wavelength and vortex shedding instabilities, respectively. As a result, the three highest energy frequencies for each case in this range form frequency triads. This suggests that the vortex shedding and the elliptic instability are coupling together. Upon closer inspection, we can see that the legs of the shedding hairpin vortices align with braids of the elliptic instability (figure 5.2). For $2.7 \leq \lambda \leq 3$, the frequencies are more organized and form harmonics of one another, indicating even stronger coupling. There are also irregular globules of vorticity being shed from the leading-edge vortex sheet, which has accumulated more streamwise vorticity as TSR has been increasing. In section 5.2.3, we analyze the SPOD modes for the flow at $\lambda = 3$ to gain more insight into the interaction between the two instabilities.

5.2 Spectral proper orthogonal decomposition for identifying energetic modes

To better characterize the short-wavelength instability, we use spectral proper orthogonal decomposition (SPOD) to identify the most energetic modes in the flow at various frequencies (Towne, Schmidt, and Colonius, 2018). SPOD at $\lambda = 2$ isolates the short-wavelength instability. We also compute the SPOD modes at $\lambda = 1$ to understand the mode shapes for non-planar-symmetric vortex shedding. Then, we examine the SPOD modes at $\lambda = 3$ to understand the mixed behaviour of these instabilities.

The SPOD analysis is similar to a PSD in that sequential snapshots of the flow over a long time period are required, with the snapshot frequency determining the

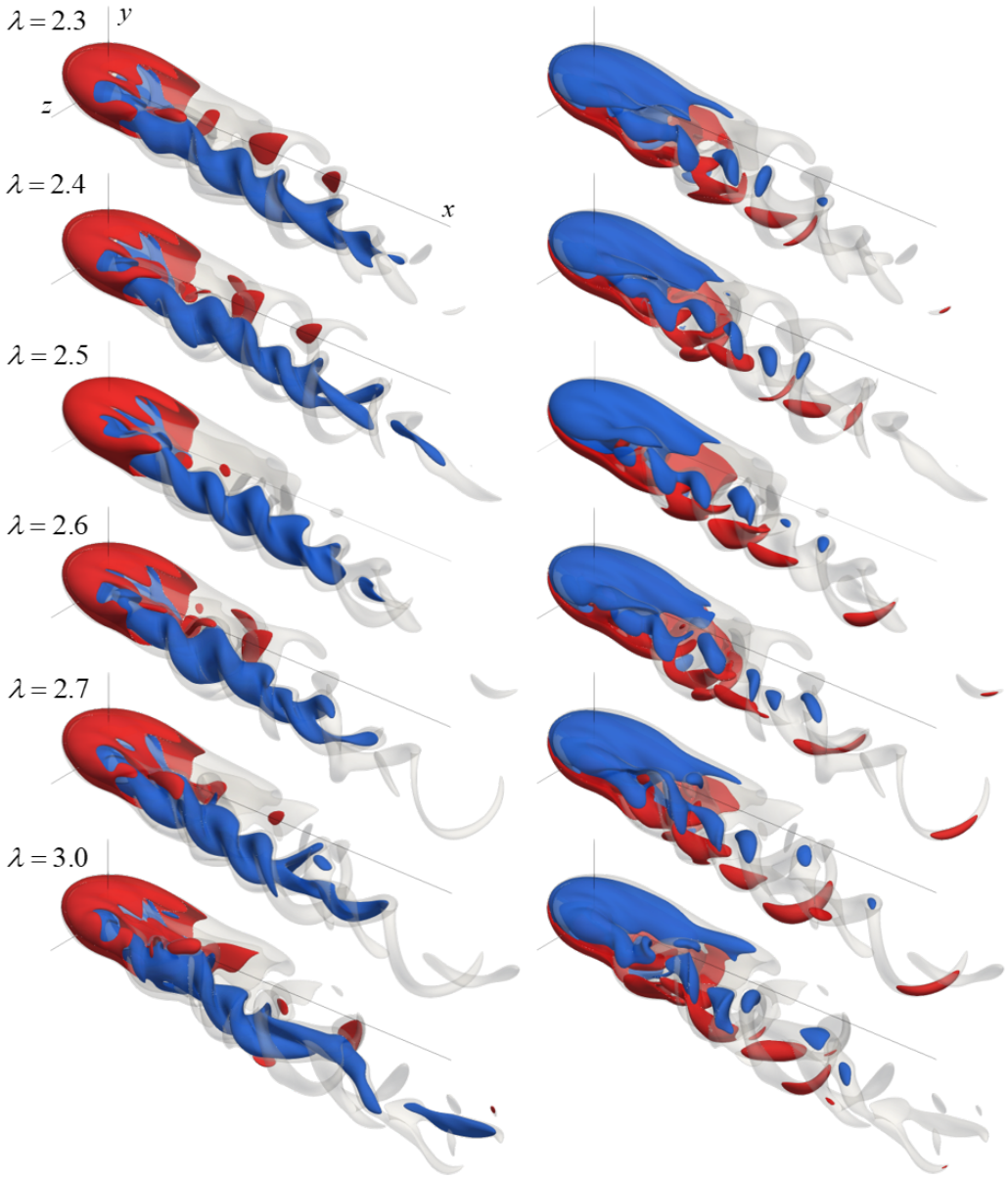

Figure 5.2: Isosurfaces of vorticity for the disk at $Re = 500$ and $\alpha = 25°$ for $\lambda = 2.3, 2.4, 2.5, 2.6, 2.7$, and 3.0. Flow is from top left to bottom right with the disk rotating clockwise from above. Semi-transparent grey isosurfaces are vorticity magnitude, $||\omega|| = 3$. Streamwise vorticity, ω_x (left column) and spanwise vorticity, ω_z (right column) are shown in opaque red and blue for positive (+3) and negative (−3) values, respectively. The x-, y-, and z-axes reference lines are $5D$, $1D$, and $1D$ long, respectively.

Nyquist limit and the time series length determining the resolution. Statistical variability in the flow allows SPOD to identify multiple coherent structures for the same frequency, if present. Using the Welch method the cross-spectral-density is estimated by dividing the time series into a number of segments—this number of segments is then equal to the number of modes that can be resolved for a given frequency. For the laminar flows analyzed here, the flow fields are periodic or nearly so, so the primary mode for each frequency contains the overwhelming majority of the energy at that frequency. Since many instances of the flow field are necessary for SPOD, it can be memory intensive, especially for 3D flows. To aid with this, we use a streaming SPOD algorithm developed by Schmidt and Towne (2019), which efficiently processes the the snapshots one by one, and makes SPOD for the 3D flow field viable (Schmidt and Towne, 2019). To minimize the data, we also coarsen the flow field data by a factor of five in each spatial direction.

5.2.1 SPOD modes for vortex shedding - $\lambda = 1$

At $Re = 500$, $\alpha = 25°$ and $\lambda = 1$, the flow exhibits non-planar-symmetric vortex shedding. Figure 5.3 shows the most energetic mode corresponding to the vortex shedding, which occurs at $St = 0.6$. The streamwise-vorticity isosurfaces shows the advancing-side legs of the hairpin vortices. The vortical structures in the spanwise-vorticity isosurfaces reach across the spanwise center plane of the disk, but do not connect to a tip vortex on the receding side. This indicates the roll up of the trailing edge vortex sheet, though biased to the advancing side.

5.2.2 SPOD modes for the short-wavelength instability - $\lambda = 2$

For $\lambda = 2$, the highest energy SPOD mode occurs at $St = 1.31$ and is shown in figure 5.4. The mode is confined to the advancing tip vortex core and we clearly see the double-helical braiding of positive and negative vorticity. Other frequency peaks are over an order of magnitude weaker than the highest frequency, and we can see from the flow reconstruction using just the mean flow and the first SPOD mode at $St = 1.31$ that the corkscrew-like structure of the advancing tip vortex is fully captured in this first mode (figure 5.5). The missing features that are associated with the lower energy modes are the shedding of vortical blobs from the leading edge vortex sheet.

There are some evident parallels between the hairpin vortex structure within the advancing tip vortex and the short-wavelength instability structure. The hairpin vortex legs also result in alternating braids of positive and negative vorticity, though

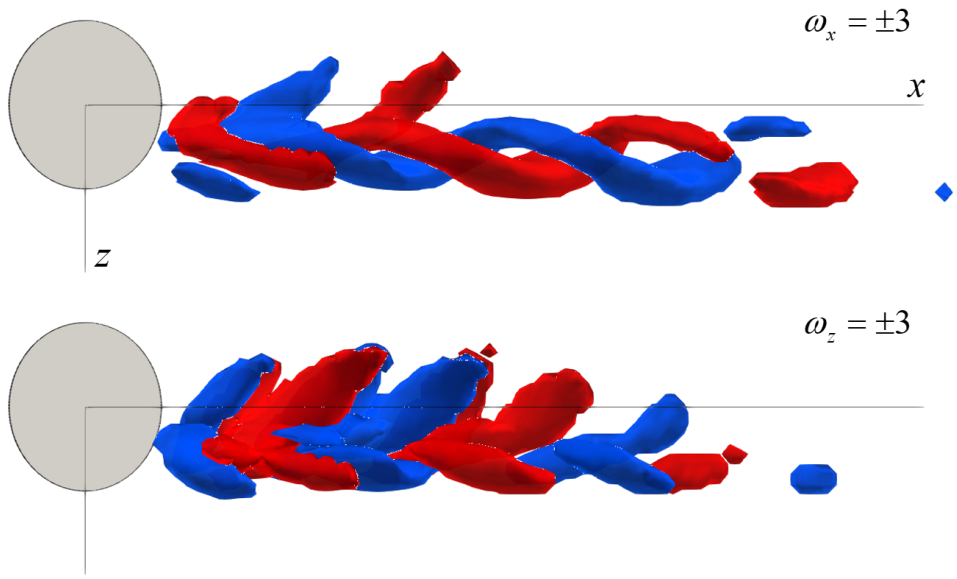

Figure 5.3: Top view of streamwise (top) and spanwise (bottom) vorticity isosurfaces of the most energetic (vortex shedding) SPOD mode for $Re = 500$, $\alpha = 25°$, and $\lambda = 1$, occurring at $St = 0.6$.

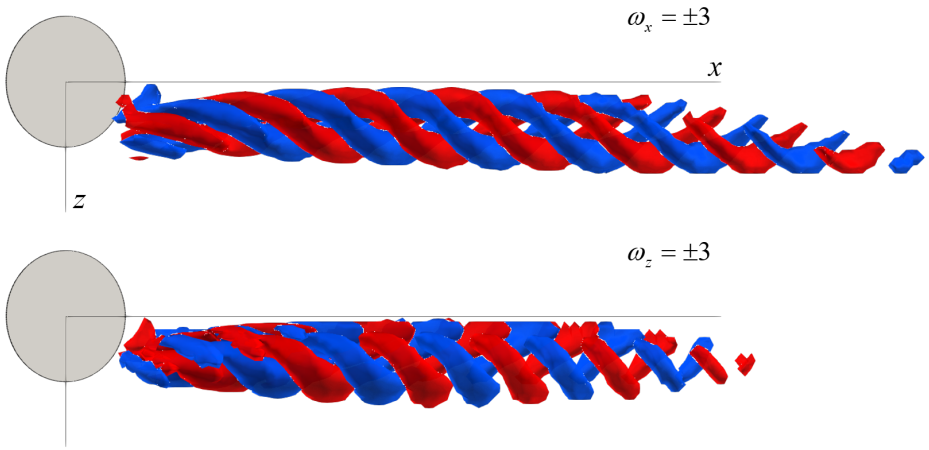

Figure 5.4: Top view of streamwise (top) and spanwise (bottom) vorticity isosurfaces of the most energetic SPOD mode for $Re = 500$, $\alpha = 25°$ and $\lambda = 2$, occurring with temporal frequency $\omega = 1.31$ and axial wavenumber $k = 1.9$

there are only two strands of vorticity per streamwise section (one positive and one negative) as opposed to four (two positive and two negative) for the short-wavelength instability. The wavelength of the hairpin vortices is longer as well, with a correspondingly lower frequency.

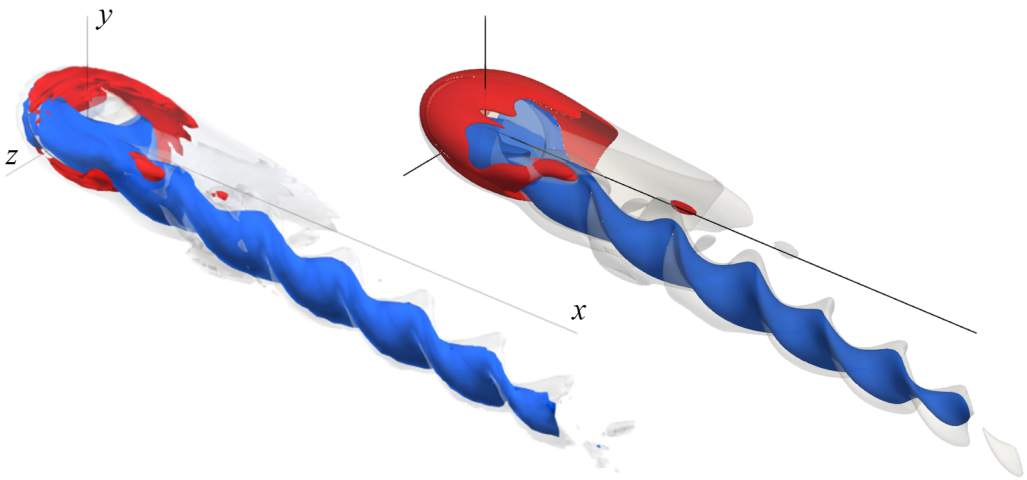

Figure 5.5: Isosurfaces of streamwise vorticity for the reconstruction of the flow by the superposition of the mean flow and the first SPOD mode at $St = 1.31$ (left) alongside a snapshot of the full flow field (right) for $Re = 500$, $\alpha = 25°$ and $\lambda = 2$.

5.2.3 SPOD modes for the mixed wake - $\lambda = 3$

For $\lambda = 3$, the frequency content is more rich, with the presence of both vortex-shedding and short-wavelength instability. SPOD allows us to isolate the mode shapes for each of these frequency peaks to better understand the flow. Figure 5.6 shows the three most energetic SPOD modes for the $\lambda = 3$ case at $Re = 500$ and $\alpha = 25°$. These modes occur at frequencies that harmonics of the primary frequency peak at $St = 0.47$. The low-frequency SPOD mode at $St = 0.47$ shows structures mainly present in the advancing tip-vortex, with fluctuations in the streamwise vorticity akin to hairpin vortex legs. The SPOD mode at $St = 0.94$ shares a similar structure to that seen for non-planar-symmetric vortex shedding in figure 5.3, although with a shorter wavelength and higher frequency. It also displays some of the same double-helical braiding of four lobes of positive and negative vorticity as with the short-wavelength instability, though much less distinct and also modified by the presence of additional vortical structures. The spanwise vortical structures indicates some fluctuations in vorticity along the trailing-edge vortex sheet as well. The SPOD mode at $St = 1.41$ also shows structures in both the advancing tip vortex and the trailing-edge vortex sheet. There is positive-negative vorticity braiding in the advancing tip vortex, though its structure is not as clean as with the mode at $St = 0.97$. The spanwise vortical structures that merge into the advancing tip vortex are reasonably distinct for this mode. Overall, the structure of the various SPOD modes demonstrates that the vortex shedding and short-wavelength instabilities no longer occur at their own distinct frequencies but instead interacting nonlinearly.

The presence of both is clearly seen for $St = 0.97$ and $St = 1.41$ as the structures align with one another.

5.2.3.1 Frequency lock-in between vortex shedding and the short-wavelength instability

For $\lambda \geq 2.3$ we observe a mixed wake behavior with both vortex shedding and the short-wavelength instability, previously described in 5.1.2. In this region, we observe a separate frequency lock-in phenomenon for $2.5 \leq \lambda \leq 3$. The SPOD modes at $St = 0.94$ and $St = 1.41$ possess features of both vortex shedding and the short-wavelength instability. These modes also occur at harmonics of $St = 0.47$, indicating that the frequency of vortex shedding and the short-wavelength instability have locked in to one another. This corresponds to the legs of vortex shedding structure being aligned with the braids of the short-wavelength instability in the advancing tip vortex. To provide a possible explanation for this phenomenon, we note that the orientation and position of the hairpin vortex legs (figure 5.3) are similar to those of the corkscrew-like braids of the short-wavelength mode (figure 5.4). They differ in their wavelength and that the corkscrew instability does not have filaments of spanwise vorticity crossing the spanwise centerline. In this case, it appears that the shedding occurs preferentially from the braids in the short-wavelength instability, allowing the different instabilities to lock in to each other's frequencies.

We present two possible explanations based on the vortical structures present. Firstly, the close match in vortical structures between the legs of hairpin vortices and the short-wavelength braids affects how the roll up the trailing-edge vortex sheet interacts with the advancing tip vortex. As the trailing edge vortex sheet rolls up, its legs will preferentially align themselves and merge with the co-rotating braids of the short-wavelength instability, resulting in the formation of hairpin-vortex legs that merge with the corkscrew braids. Alternatively, in figure 5.1 we saw the increasing spanwise alignment of the short-wavelength braids, which leads to increased spanwise vorticity around the the tip vortex. With enough vorticity, these spanwise braids eventually begin to shed and interact with the trailing edge vortex sheet, causing roll up. In either case, the braids and vortex-sheet roll up will tend to align due to the merging of co-rotating vortical elements. In the transitionary region, the two frequencies don't quite line up, so a myriad of other frequencies arise as the vortex shedding and short-wavelength instabilities interact at different phases.

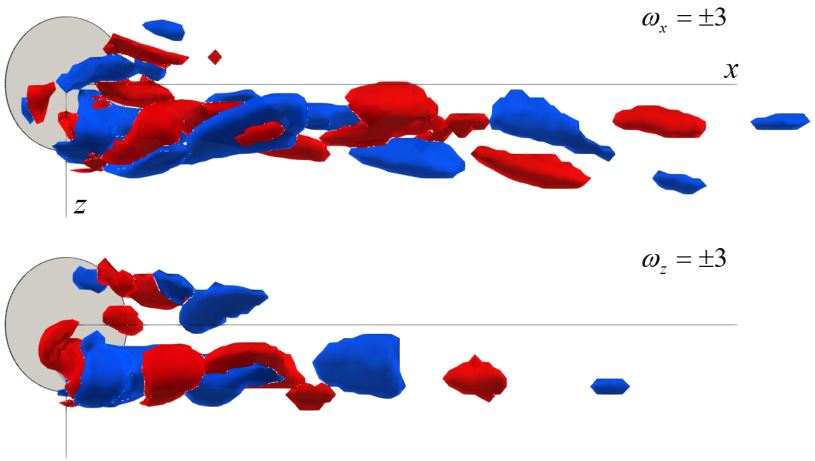

(a) $St = 0.47$

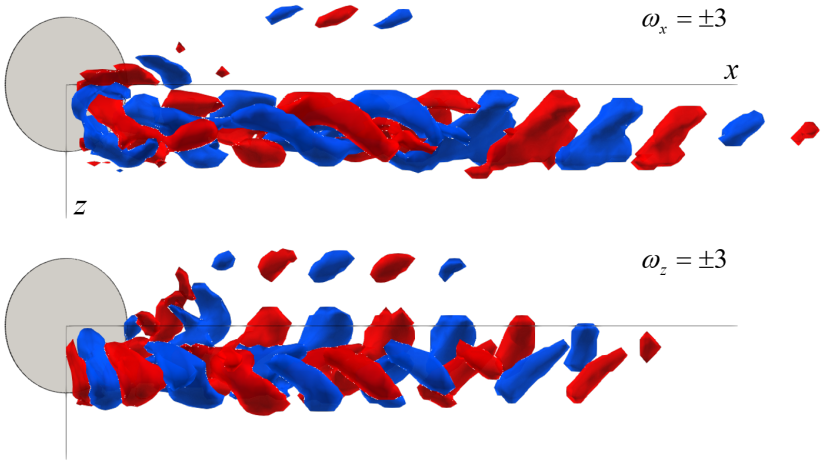

(b) $St = 0.94$

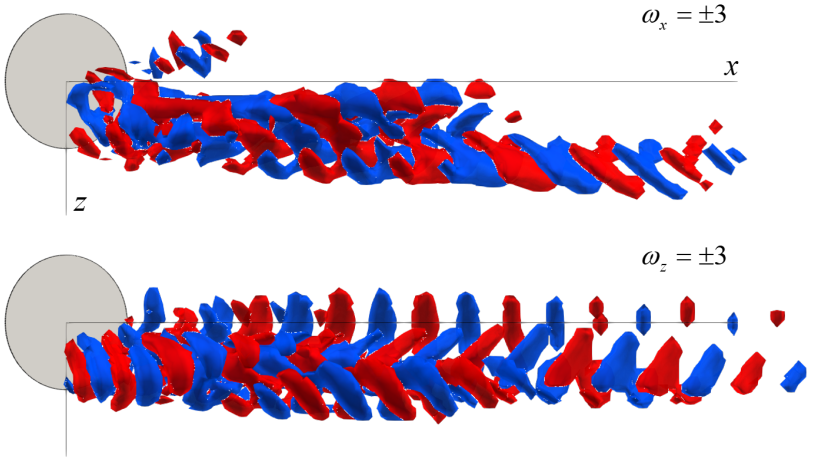

(c) $St = 1.41$

Figure 5.6: Top view of streamwise (top) and spanwise (bottom) vorticity isosurfaces of the most energetic SPOD mode for $Re = 500$, $\alpha = 25°$ and $\lambda = 3$.

5.3 The elliptic instability in a pair of counter-rotating Batchelor vortices

In order to understand the presence of the short-wavelength instability, we first note its close resemblance to one of the elliptic instability modes. Elliptic instability occurs as a result of the amplification of Kelvin modes in a vortex core due to an external strain field, often from an adjacent vortex (Widnall, Bliss, and Tsai, 1974). Elliptic instabilities are so called because the strain field imposed by one vortex on the other causes an elliptic deformation of the otherwise circular vortices in the base flow (Ryan and Sheard, 2007).

The elliptical instability has been studied in a variety of vortex-pair configurations, including various vorticity profiles, both counter- and co-rotating vortex pairs, and with and without axial flow. The most unstable mode depends on these details and is summarized by Kerswell (2002) and Leweke, Le Dizès, and Williamson (2016). For this chapter, we will focus specifically on elliptic instability in a pair of counter-rotating Batchelor vortices, which was investigated in detail by Ryan and Sheard (2007) and Lacaze, Ryan, and Le Dizès (2007). The Batchelor vortex has both Gaussian axial vorticity and axial velocity profiles, and thus matches closely to the velocity profile for a pair of tip vortices behind wings (Batchelor, 1964). While the elliptical instability is typically studied in pairs of equal strength vortices, it can occur for unequal strength pairs as well or in single vortices as long as a strain field is applied (Ryan, Butler, and Sheard, 2012).

5.3.1 The Batchelor vortex

For a single Batchelor vortex, the non-dimensionalized axial vorticity, $\omega_0(r)$, and axial velocity, $W(r)$, are given by:

$$\omega_0(r) = 2\exp(-r^2), \text{ and} \tag{5.1}$$

$$W(r) = W_0 \exp(-r^2), \tag{5.2}$$

where r is the radial distance, $W_0 = 2\pi R_0 \xi/\Gamma$ is the axial velocity strength, Γ is the circulation, ξ is the dimensional axial velocity, and R_0 is the vortex radius. Note that the axial velocity strength, W_0, can also be written in terms of the ratio of the maximum axial velocity to the maximum azimuthal velocity to the maximum $W_0 = (0.638 \max V)/(\max W)$, where V is the azimuthal velocity. The azimuthal velocity is non-dimensionalized by the angular velocity in the vortex $\Omega_0 = \Gamma/(2\pi R_0^2)$, and can be written as

$$V(r) = \frac{1}{r}\left(1 - \exp(-r^2)\right). \tag{5.3}$$

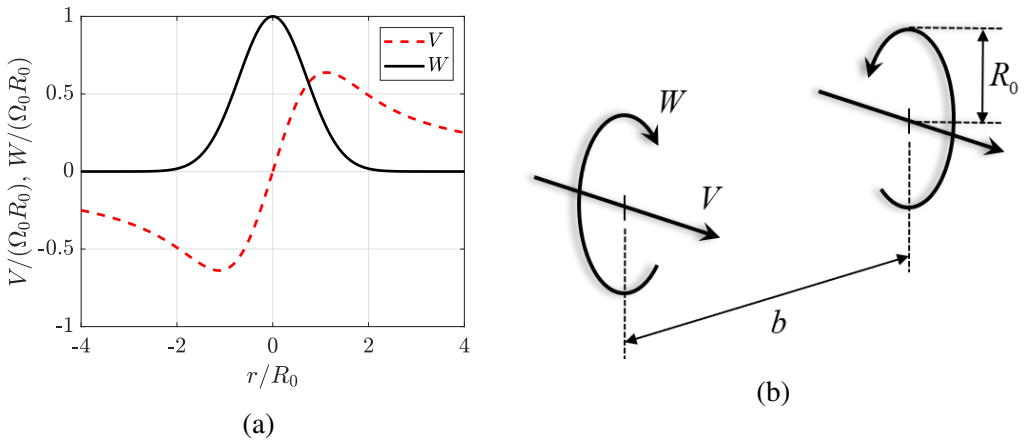

Figure 5.7: Setup for the Batchelor vortex: (a) axial and azimuthal velocity profiles, and (b) diagram for configuration of a counter-rotating pair of Batchelor vortices.

Figure 5.7a depicts the velocity profile for $W_0 = 1$. We can consider a pair of counter-rotating vortices, where one vortex imposes a strain on the other (figure 5.7b). The flow is then parameterized by the circulation Reynolds number, $Re_\Gamma = \Gamma/(2\pi\nu)$, the axial velocity strength, W_0, and the strain rate imposed on the vortex, ε. Using a point-vortex approximation, the strain rate can be approximated by

$$\varepsilon \approx \frac{\Gamma}{2\pi b^2}, \tag{5.4}$$

where b is the distance between the centers of the two vortices.

5.3.2 Conditions for elliptic instability

The elliptic instability arises from resonance of Kelvin modes in the vortex core. Kelvin modes are the linear normal perturbation modes in the core of a columnar vortex in the inviscid limit (Thomson, 1880). For the Batchelor vortex, the Kelvin modes are given in cylindrical coordinates (r, θ, z) for the velocity field, $\mathbf{u}'$, and pressure field, p', by

$$\mathbf{u}' = \mathbf{u}_K(r) exp\left(ikz + im\theta - i\omega t\right), \text{ and} \tag{5.5}$$

$$p' = p_K(r) exp\left(ikz + im\theta - i\omega t\right), \tag{5.6}$$

where k is the axial wavenumber, m is the azimuthal wavenumber, and ω is the temporal frequency (not to be confused with the vorticity vector, $\boldsymbol{\omega}$) (Thomson, 1880; Lacaze, Ryan, and Le Dizès, 2007). Individual Kelvin modes are all neutrally stable or damped (Ryan and Sheard, 2007). However, the strain imposed by one vortex on the adjacent vortex causes a coupling of pairs of Kelvin modes. These

pairs are referred to as principal modes, and they are able to resonate in certain conditions, giving rise to the elliptic instability.

The pairs of modes follow strict rules in order to achieve resonance. First, their temporal frequency and axial wavenumbers must match. In addition, their azimuthal wavenumbers must differ by two (see Eloy and Le Dizès, 2001; Lacaze, Birbaud, and Le Dizès, 2005). This can be written as

$$\omega_1 = \omega_2, \quad k_1 = k_2, \quad m_1 = m_2 \pm 2, \tag{5.7}$$

where the subscripts denote the first and second mode of the pair. The branch label, l, gives the numuber of zeros in the radial velocity along the radial direction. Typically, the most unstable configuration is for $l_1 = l_2 = l$. As a result, principal modes are referenced by their azimuthal wavenumbers, m_1 and m_2, and a branch label, l, as (m_1, m_2, l). The condition for perfect resonance is given by Eloy and Le Dizès (2001) as

$$\omega - kW_0 = \frac{m_1 + m_2}{2}, \tag{5.8}$$

relating the wavenumbers and temporal frequency to the axial velocity strength.

Lacaze, Ryan, and Le Dizès (2007) performed a stability analysis to identify the most unstable principal modes in the pair of counter-rotating Batchelor vortices for a range of Re_Γ, W_0 and ε values. They find that the principal modes (m_1, m_2, l) of the elliptic instability are unstable for sufficiently high circulation Reynolds number and strain rate. Though the exact principal modes that are most unstable do depend on Re_Γ and ε, the axial velocity strength, W_0, is the strongest factor in determining the most unstable principal modes. This is due to the presence or absence of a critical layer and its associated damping for the various Kelvin modes as W_0 changes. As a result, the amount of axial flow plays a key role in the nature of the elliptic instability. While the $(-1, 1, 1)$ principal mode is dominant for vortex pairs with no axial flow, the modes become damped in the presence of axial flow. Instead, the $(-2, 0, 1)$ principal mode is most unstable in flows with sufficient axial flow ($W_0 \geq 0.2$), where the critical-layer damping rate decreases in magnitude as W_0 increases (Lacaze, Ryan, and Le Dizès, 2007). This $(-2, 0, 1)$ principal mode consists of the resonant coupling between the $m = 0$ Kelvin mode, which produces axial swelling and contracting of the vortex core, and the $m = -2$ Kelvin mode, which consists of the alternating braiding of positive and negative vorticity perturbations (Ryan and Sheard, 2007). The $m = -1$ mode is strongly damped at low W_0 but is neutrally stable for $W_0 \geq 0.5$ (Lacaze, Ryan, and Le Dizès, 2007). In

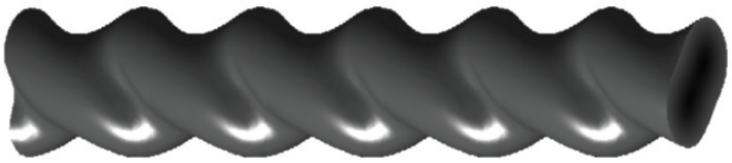

Figure 5.8: Vorticity isosurfaces for the theoretical (-2, 0, 1) principal mode. The image is reproduced with permission from Leweke, Le Dizès, and Williamson (2016).

combination, this results in a cork-screw vortical structure with an axial wavelength on the order of the inter-vortex distance, seen in figure 5.8.

Comparing these vorticity isosurface representations, we see substantial qualitative match in the short-wavelength instability and the $(-2, 0, 1)$ principal mode shown by (Leweke, Le Dizès, and Williamson, 2016) (figure 5.8. They both feature a double-helical, corkscrew shape of the vortex core. In order to provide a more detailed quantitative comparison, we will use spectral proper orthogonal decomposition (SPOD) to isolate the short-wavelength mode and compare its frequency and wavenumbers with that seen in studies by Lacaze, Ryan, and Le Dizès (2007).

5.4 Modeling tip vortices as a pair of counter-rotating Batchelor vortices

To provide a quantitative comparison between the short-wavelength instability and the elliptic instability, we estimate the flow parameters in the advancing tip vortex that are relevant to the elliptic instability. These parameters are the axial velocity strength, W_0, the circulation Reynolds number, Re_Γ, and the strain rate, ε. To estimate these parameters, we model the mean flow in the tip vortices as a pair of counter-rotating Batchelor vortices. These values can change along the length of the tip vortex so we estimate the values at several streamwise distances to evaluate the range of values found in the vortex. We use vortices with unequal strengths since the advancing tip vortex is considerably stronger than the receding tip vortex. The mean flow is shown in figure 5.9. Note that the receding tip vortex is present, but weaker than the advancing tip vortex.

5.4.1 Axial velocity strength, W_0

The axial velocity strength scales with the ratio of maximum axial velocity to maximum azimuthal velocity. In the tip vortex configuration, the non-zero axial velocity arises from the velocity deficit in the vortex cores, with axial velocity tending to the freestream velocity away from the vortex core. By changing to

Figure 5.9: Streamwise vorticity isosurface ($\omega_x = 1$) for the mean flow at $Re = 500$ and $\alpha = 25°$ for $\lambda = 2$.

the freestream-fixed reference frame, this is equivalent to the general configuration outlined by the vortex profiles in equations 5.1 and 5.3, namely a peak axial velocity at the vortex center that goes to zero with increasing radial distance. As TSR is increased, we saw that the rotation induces a recirculation region that aligns with the advancing tip vortex and creates a region of upstream flow. Overall, this increases the velocity deficit in the vortex cores, resulting in higher W_0 as TSR increases.

To determine the axial velocity strength, W_0, we determine the maximum azimuthal velocity and maximum axial velocity in the advancing tip vortex at a given streamwise plane. Note that the azimuthal velocity profile can be fit using either the maximum azimuthal velocity (equation 5.3) or using the maximum axial vorticity (equation 5.1). The maximum axial vorticity provides the center of the vortices for estimating the inter-vortex distance b. Figure 5.10 provides an example fit for the Batchelor vortices based on fitting the Gaussian profiles to the maximum axial vorticity and maximum axial velocity. We include the resulting azimuthal velocity estimate to show that while this model provides a reasonable estimate, it does not fully capture the tip-vortex configuration. While a more involved optimization could be performed, this crude approximation is quite reasonable given that the Batchelor vortex model is incomplete and will not be able to account for the presence of other vortical structures in the wake such as the leading-edge and trailing-edge vortex sheets.

The estimates of axial velocity strength using both azimuthal velocity estimates are shown in figure 5.11. There is some variability along the length of the vortex and between the two methods, with an average value of $W_0 \approx 1.2$.

5.4.2 Circulation Reynolds number, Re_Γ

To determine the circulation Reynolds number, we estimate the total circulation in the advancing tip vortex by integrating the negative streamwise vorticity in the vortex for each streamwise plane. Figure 5.12 shows the evolution of the circulation

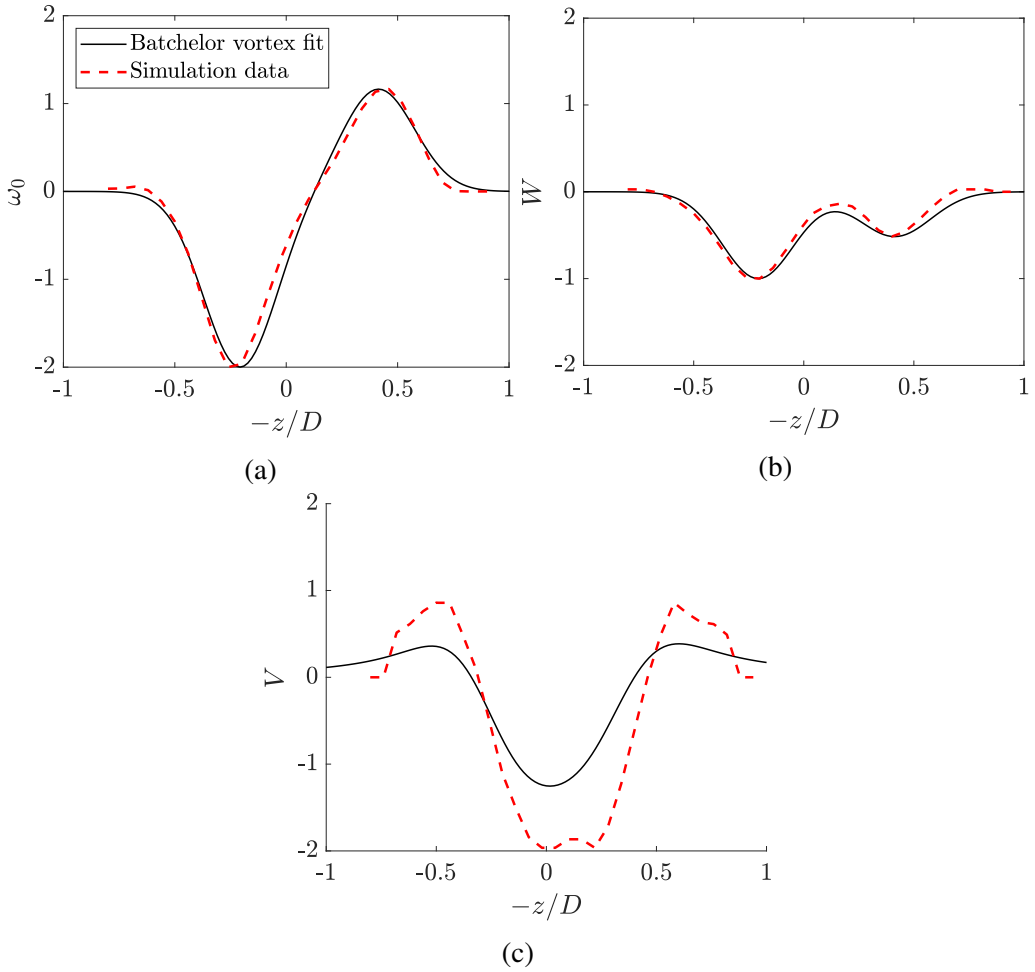

Figure 5.10: Comparison of the real profiles and the modeled Batchelor vortex profiles determined using max W and max ω_0 for (a) axial vorticity, (b) axial velocity, and (c) azimuthal velocity.

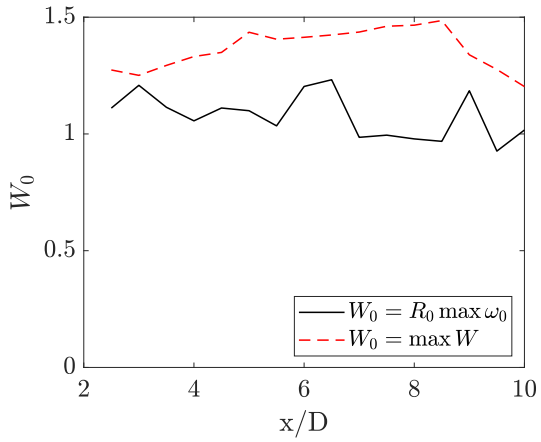

Figure 5.11: Axial velocity strength with streamwise distance estimated from either fitting the Batchelor vortex profile to the maximum axial vorticity or the maximum axial velocity.

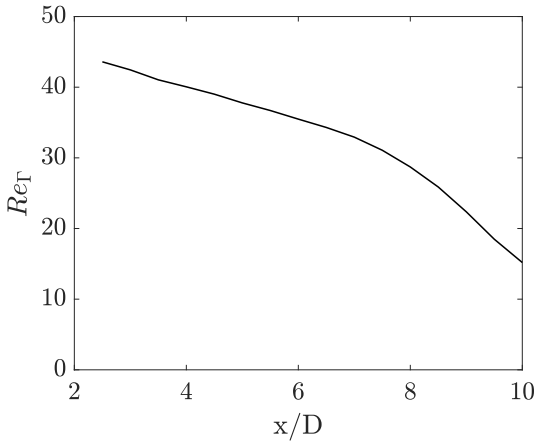

Figure 5.12: Circulation Reynolds number with streamwise distance.

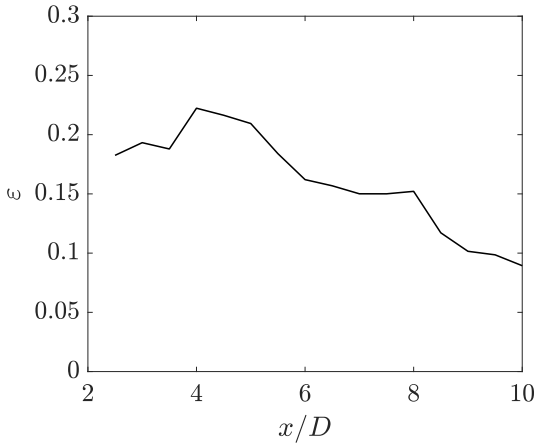

Figure 5.13: Strain rate estimate using equation 5.4 as a function of streamwise distance.

Reynolds number with streamwise distance. The circulation Reynolds number decreases as vorticity diffuses by viscous effects. We can estimate the circulation Reynolds number as $Re_\Gamma \approx 35$ in the mid wake.

5.4.3 Strain rate, ε

The strain rate, ε, can be estimated for a known circulation, Γ, and inter-vortex distance, b, by equation 5.4. Note that the circulation used is for the adjacent vortex, namely the receding tip vortex. The inter tip-vortex distance is determined by the distance between the peaks in axial velocity in both tip vortices. Figure 5.13 shows the strain rate estimate against streamwise distance. Strain decreases since it is dependent on the circulation, which decreases with downstream distance. We can estimate the strain as $\varepsilon \approx 1.5$ in the mid wake.

5.5 Comparisons between the short-wavelength instability and the elliptical instability

Having estimated the parameters in the tip vortices using the Batchelor vortex model, we perform several different comparisons between the short-wavelength instability and the elliptic instability. First, we check that the tip-vortex parameters estimated in 5.4 match the expected unstable ranges for the elliptic instability, particularly of the $(-2, 0, 1)$ mode. Then we compare streamwise cross-sections of the mode shapes and discuss the corresponding wavenumbers and frequencies. Finally, we consider the conditions for perfect resonance between pairs of Kelvin modes in the elliptic instability, and ensure that this condition is indeed satisfied for the short-wavelength instability.

Lacaze, Ryan, and Le Dizès (2007) show the most unstable modes in the (W_0,εRe_Γ) parameter space. For $\varepsilon = 0.1$ within the range $0 \leq W_0 \leq 0.6$, all of the principal modes are stable at least up to $\varepsilon Re_\Gamma \approx 4$. Increasing strain rate lowers the Reynolds number at which the modes first become unstable, since strain amplifies the resonance of the modes. The most unstable principal mode at $Re_\Gamma = O(10)$ for $W_0 \geq 0.18$ is the $(-2, 0, 1)$ mode (Lacaze, Ryan, and Le Dizès, 2007). The lowest Re_Γ at which the mode is unstable depends on W_0, but is as low as about $\varepsilon Re_\Gamma = 4$ at $W_0 = 0.4$. Since Lacaze, Ryan, and Le Dizès (2007) only consider W_0 up to 0.6, it is not possible to make a direct comparison. However, we do expect the $(-2, 0, 1)$ principal mode to continue to show resonant properties, since the individual Kelvin modes are neutrally stable for $W_0 \geq 0.5$ (Lacaze, Ryan, and Le Dizès, 2007). From section 5.4, we estimate that the tip vortices have $\varepsilon Re_\Gamma \approx 5$ with $W_0 \approx 1.2$. Therefore, the advancing tip vortex for $Re = 500$, $\alpha = 25°$ and $\lambda = 2$ does possess the correct order of magnitude of flow parameters for the $(-2, 0, 1)$ mode to be unstable, when modeled by the Batchelor vortex pair. This is consistent with the onset of the elliptic instability at around $\lambda = 1.8$, where the circulation Reynolds number and strain will be slightly lower than for the $\lambda = 2$ case since the advancing tip vortex is weaker. For the highest axial velocity strength considered by Lacaze, Ryan, and Le Dizès (2007), the axial wavenumber of the flow is $k \approx 2$ and is fairly independent of W_0, Re_Γ and ε for $W_0 > 0.5$. This matches well with the axial wavenumber of the short-wavelength SPOD mode at about $k = 1.9$.

Figure 5.14 shows streamwise cross-sections of the SPOD modes for comparison with various elliptic-instability principal modes. Although principal modes can show resonance for a range of (k, ω) combinations depending on W_0 (by the res-

onance condition in equation 5.8), the mode shapes themselves maintain the same qualitative features. As a result, while we do not have direct literature comparisons for our estimated vortex configuration $Re_\Gamma \approx 35$ and $\varepsilon \approx 0.15$, we can still find strong qualitative comparisons across different (Re_Γ, ε) values. We compare to the $(-2, 0, 1)$, $(-3, -1, 1)$, and $(-4, -2, 1)$ principal modes presented by Lacaze, Ryan, and Le Dizès (2007) for $W_0 = 0.482$, $Re = 3180$, and $\varepsilon = 0.063$, shown in figure 5.15. The SPOD mode at $St = 1.31$ displays the same structure as the $(-2, 0, 1)$ principal mode, with four lobes of alternating vorticity sign arranged in a circle (figure 5.15). The same is true comparing the SPOD modes at $St = 2.1$ and $St = 2.5$ to the $(-3, -1, 1)$ and $(-4, -2, 1)$ principal modes, respectively, but for additional numbers of lobes. Note that while the energies of the SPOD modes at $St = 2.1$ and $St = 2.6$ are about three orders of magnitude lower than that of the most energetic SPOD mode at $St = 1.3$, they form distinct peaks above the noise level. The axial velocity strength required for the perfect resonance of these SPOD modes at $St = 2.1$ and $St = 2.6$ are $W_0 \approx 1.4$ and $W_0 \approx 1.5$, respectively. These are in line with the rough estimate of W_0 from section 5.4, although the estimate is too crude to state for certain the level of resonance achieved. This matches with the analysis by Lacaze, Ryan, and Le Dizès (2007) which shows that for $W_0 \geq 0.5$, the $(-2, 0, 1)$ principal mode is more unstable than both the $(-3, -1, 1)$ and $(-4, -2, 1)$ principal modes. Regardless, we draw attention to them because they are still present with very low spectral energy, indicating that they may be neutrally stable or weakly damped.

5.5.1 Condition for perfect resonance

To provide further confirmation that the observed short-wavelength instability is the $(-2, 0, 1)$ principal mode of the elliptic instability, we can determine if it satisfies the conditions for perfect resonance that allow two Kelvin modes to couple. We can rewrite equation for the condition of perfect resonance (equation 5.8) to get an expression for W_0 in terms of the wavenumbers and temporal frequency, which gives

$$W_0 = \frac{1}{k}\left(\omega - \frac{m_1 + m_2}{2}\right). \tag{5.9}$$

Using this equation, we can use the wavenumbers and frequency of the short-wavelength SPOD mode, and estimate the axial velocity strength that would lead to perfect resonance. For the SPOD mode at $\lambda = 2$ with $St = 1.31$, $k = 1.9$, $m_1 = -2$ and $m_2 = 0$, equation 5.9 gives perfect resonance for axial velocity strength of $W_0 = 1.22$. This matches closely with our axial velocity strength estimate of $W_0 \approx 1.2$ from section 5.4.1, indicating that the tip-vortex configuration supports

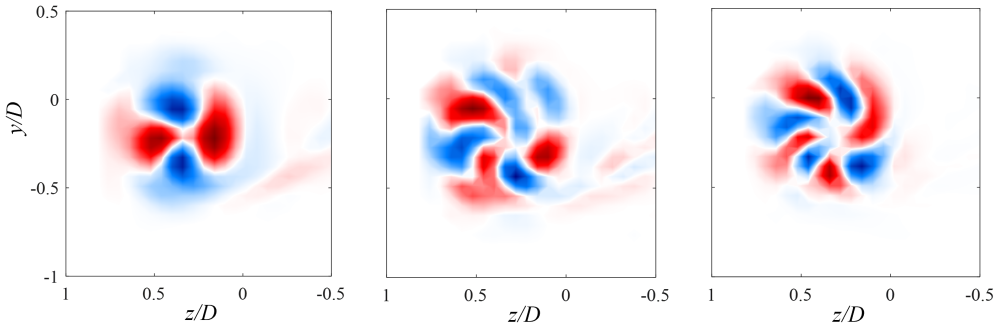

(a) $k = 1.9$, $\omega = 1.31$ (b) $k = 3.0$, $\omega = 2.06$ (c) $k = 3.8$, $\omega = 2.59$

Figure 5.14: Streamwise vorticity in a streamwise cross-section of SPOD modes at $\omega = 1.3, 2.1$ and 2.5 for $Re = 500$, $\alpha = 25°$, and $\lambda = 2$. The solid black line represents the disk's streamwise projection.

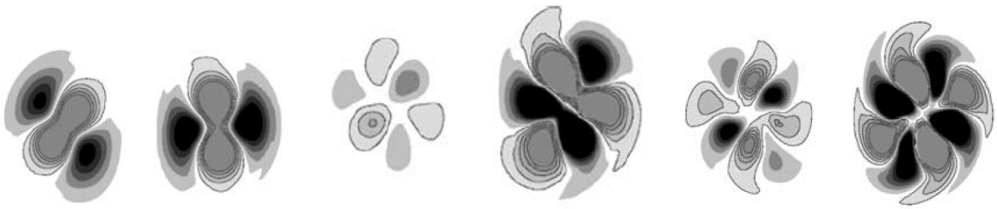

(a) $(-2, 0, 1)$, $k = 1.88$ (b) $(-3, -1, 1)$, $k = 3.23$ (c) $(-4, -2, 1)$, $k = 4.57$

Figure 5.15: Cross-sections of the vorticity perturbation fields at $W_0 = 0.482$, $Re = 3180$, and $\varepsilon = 0.063$ for various principal modes from simulations by Lacaze, Ryan, and Le Dizès (2007).

perfect resonance of the $(-2, 0, 1)$ principal mode.

5.6 Frequency lock-in between the short-wavelength instability and disk rotation

Revisiting the changing frequency content displayed in figure 3.9, we see that the frequency of the short-wavelength instability increases with TSR for $1.9 \leq \lambda \leq 2.2$. In fact, this frequency increase coincides closely with twice the frequency of disk rotation. This demonstrates a lock-in phenomenon between the short-wavelength instability and the disk rotation. Lock-in suggests that the disk rotation may play a role in helping to force the $(-2, 0, 1)$ principal mode, especially for this region where the flow is very close to the critical point. Fluctuations associated with the rotation could force the $(-2, 0, 1)$ principal mode, even if it is neutrally stable or damped. We also observe a range of TSRs right after the lock-in region ($2.3 \leq \lambda \leq 2.6$) for which the energy of the elliptic instability first declines. The strength of the $(-2, 0, 1)$

mode may be enhanced specifically in this lock-in region thanks to resonance with the disk rotation forcing, allowing it to appear distinctly within this range, even though it is less apparent just beyond the lock-in range. For $2.6 \leq \lambda \leq 3$, the energy of the $(-2, 0, 1)$ mode continues to grow. This is consistent with the increasing growth rates of the mode as Re_Γ and ε increase with increasing λ.

5.7 Flow over spinning disks at high Reynolds number

To predict the presence of the short-wavelength instability at higher Reynolds numbers, we briefly present some preliminary results for flow over a spinning disk at $Re = 4000$ and $\alpha = 25°$. We observe many of the same flow features that are present at $Re = 500$, including vortex shedding, its reduction, and elliptic instability. These simulations are performed with grid resolution $\Delta x = 0.0048$, scaled based on the $O(Re^{-1/2})$ laminar boundary layer thickness. Figures 5.16 and 5.17 show isosurfaces of streamwise and spanwise vorticity for $\lambda = 0$ and $\lambda = 2$, respectively. The non-spinning case shows distinct vortex shedding and tip vortices, though several smaller scale structures are present throughout as well. At $\lambda = 2$, we see significantly strengthened tip vortices that persist further downstream, along with weakened vortex shedding. A close look at the tip-vortices shows some corkscrew-like braids reminiscent of elliptic instability. The legs of the spanwise vortical structures align with these braids as well, and there is spanwise roll up all around the tip vortices. Towards the end of the wake, we see long-wavelength mirrored sinusoidal perturbations in both tip vortices, characteristic of the onset of Crow instability in trailing vortices (Crow, 1970). If allowed to develop, the Crow instability causes the tip vortices to pinch together and eventually form vortex rings in the wake. These simulations demonstrate the persistence of vortex-shedding suppression and elliptic instability at higher Reynolds numbers, although modulated by additional instabilities and small-scale structures.

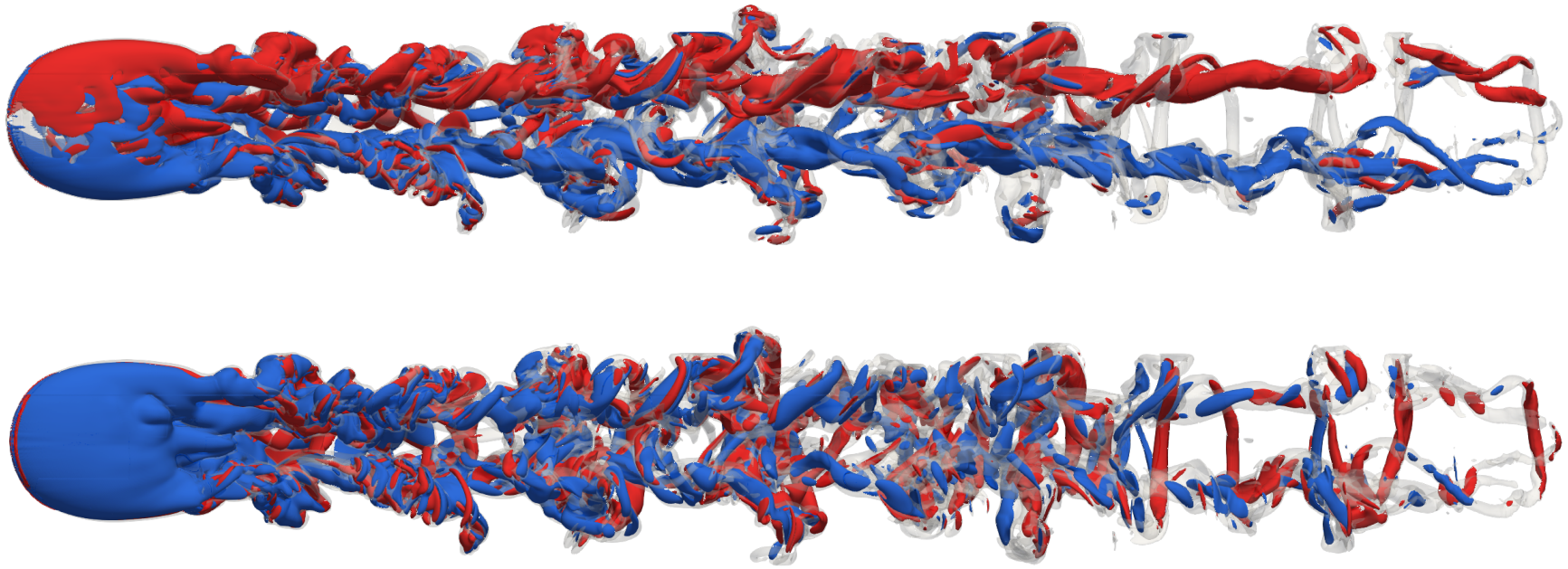

Figure 5.16: Top view of isosurfaces of vorticity, ω, for the wake behind a disk at $Re = 4000$, $\alpha = 25°$, and $\lambda = 0$. Flow is from left to right with the disk rotating clockwise (from above). Grey isosurfaces are for vorticity norm $||\omega|| = 3$. In the top image, red and blue isosurfaces represent positive and negative streamwise vorticity ($\omega_x = +3$ and $\omega_x = -3$) and in the bottom image, red and blue isosurfaces represent positive and negative spanwise vorticity ($\omega_z = +3$ and $\omega_z = -3$)

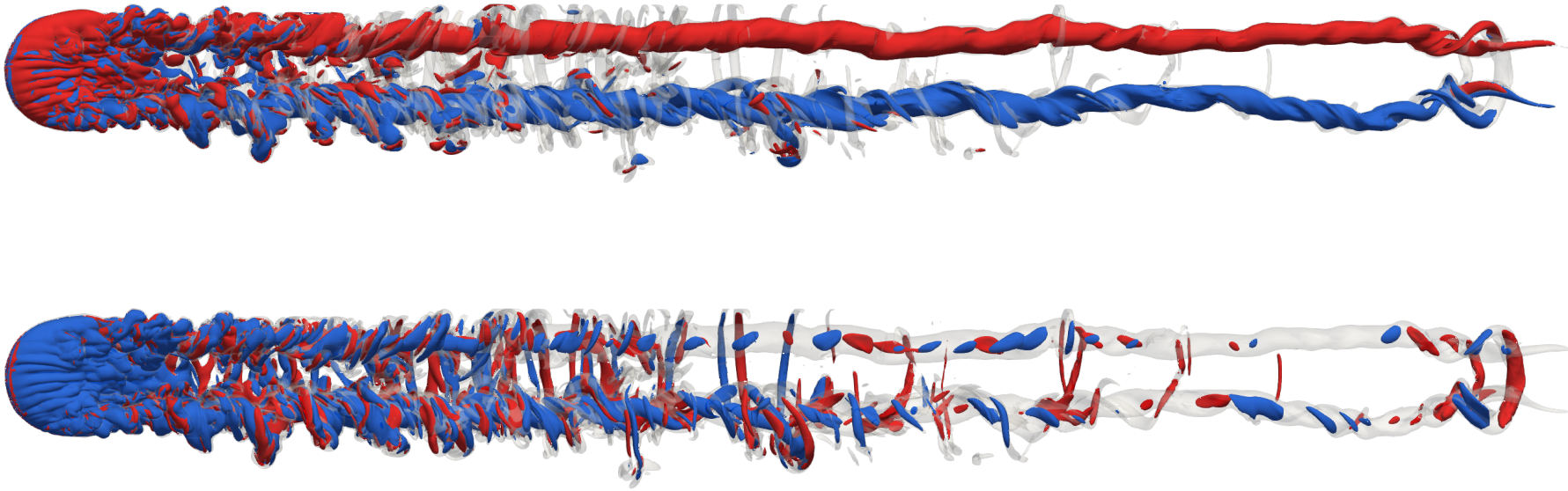

(a)

Figure 5.17: Same as figure 5.16 but for $\lambda = 2$.

5.8 Conclusions and Discussion

At high TSRs ($\lambda \geq 1.9$) beyond the region of vortex-shedding suppression, we observe the appearance of a distinct, short-wavelength instability that closely resembles the $(-2, 0, 1)$ principal mode of the elliptical instability. By using SPOD to isolate the mode shape and estimating the relevant parameters of the tip-vortex profiles, we find that the frequency and wavenumbers match the conditions for perfect resonance that is characteristic of elliptic instability. At the same time, we observe a lock-in phenomenon between twice the disk rotation frequency and the short-wavelength instability that appears to act as additional forcing, enhancing the resonance of the $(-2, 0, 1)$ principal mode. For the highest TSRs considered ($2.3 \leq \lambda \leq 3$), the wake exhibits a mixture of vortex shedding and short-wavelength instability. At certain TSRs, for example for $2.6 \leq \lambda \leq 3$, the frequency peaks of these combined phenomena organize into harmonics of one another, with hairpin-vortex shedding occurring quasi-periodically with the braids of the elliptic instability. In summary, it appears that these two main instability modes characterize the flow seen over the range of TSRs. These are the vortex shedding mode, which consists of trailing-edge vortex-sheet roll up, and the $(-2, 0, 1)$ principal mode, which is an elliptic instability within the tip-vortex core. We observe either their individual distinct presence when only one is supercritical, of their combined nonlinear interactions when both are excited. Vortex shedding occurs as a result of growing perturbations in the wake for a sufficiently strong trailing edge vortex sheet. On the other hand, the $(-2, 0, 1)$ principal mode arises when resonance conditions are achieved with sufficient circulation, axial velocity, and strain in the advancing tip vortex. While these instabilities arise by different mechanisms and are located in different parts of the wake, their proximity and similar structures allow them to interact when they are both present.

We remark that the $(-2, 0, 1)$ principal mode does not appear in the non-spinning parameter space. While Re and α can both change the vorticity in the tip vortices, they seem not able to create the conditions required for resonance of the elliptic instability modes. Rather, increasing TSR allows for appropriate values of Re_Γ, ε and W_0 for the elliptic instability to occur. This is the result of the suction effect from the rotating disk's recirculation region, which additionally injects linear momentum directly into the advancing tip vortex, modifying the axial velocity significantly.

While there is a strong match with features from studies of the $(-2, 0, 1)$ principal mode in Batchelor vortices, some of the discrepancies in the flow configuration will

likely affect the prediction of the exact critical points. In addition to the discrepancy between the actual tip vortex profile compared to the idealized Batchelor vortex shape, there is also the presence of the trailing-edge vortex sheet just outside the vortex core. It could be that this vortex sheet imposes a significant strain on the tip vortex, as it does possess opposite streamwise vorticity to the advancing tip vortex. This affects the estimation of the strain parameter, ε. Despite these discrepancies in the flow configuration, the strong match in mode shapes shows the robustness of these modes over a range of frequencies, wavenumbers and axial velocity strength, as long as resonance conditions are met. Therefore, while we have considered here only a single (Re, α) combination, we expect these principal modes to emerge for a range of flow parameters if there is sufficient spin to produce the required flow profile in the tip vortices. Similarly, the frequency lock-in effect between the disk rotation and the elliptic instability, as well as that between vortex shedding and the elliptic instability in the mixed wake, is a condition specific phenomenon that will arise when frequencies align appropriately.

We also observe many of the same wake structures at an order of magnitude higher Reynolds number of $Re = 4000$. Although high Reynolds number flow is more complex, with small-scale structures and additional instabilities, vortex shedding is known to persist for bluff bodies at high Reynolds numbers, for example in flow over inclined disks (Calvert, 1967) and flow over axisymmetric bluff bodies (Rigas et al., 2014). While separation profiles and boundary layer formation are different for high Reynolds numbers, disk rotation inevitably injects both linear and angular momentum into the wake, leading to increased circulation in the wake (Nakamura and Fukamachi, 1991; Higuchi et al., 2000). However, it remains to be seen if elliptic instability will continue to persist as Reynolds number increases into turbulent regimes.

Chapter 6

CONCLUSIONS

In this thesis, the flow over a spinning disk at angle of attack was investigated in regimes that lie at the intersection between available studies on laminar flow over non-spinning disks and on spinning-Frisbee flight in turbulent regimes. We observed bifurcations associated with instabilities that alter the aerodynamic forces and wake dynamics. In this chapter, we summarize the main conclusions from each chapter, discuss their implications, and suggest noteworthy avenues for future work.

In Chapter 2, we proposed a method to simulate disk rotation using rigid-body-rotation boundary conditions applied to the immersed-boundary points. We validated the results using comparisons of aerodynamic forces for non-spinning disks, showing that the disk thickness can affect the location of critical points for the vortex-shedding bifurcation.

In Chapter 3, we swept over a range of TSRs up to three to observe the effect of spin on the aerodynamics. We observed a monotonic increase in lift and drag for all TSR values. This effect appears to be largely Reynolds number independent, with studies at $Re = O(10^5)$ showing similar increases in lift and drag for $\lambda > 1$, though changes are negligible for $\lambda < 1$ (Potts, 2005). The effect of spin on lift-to-drag ratio and moment coefficients is marginal, showing promise for application in spinning disk flight with consistent flight properties. We also observe several interesting phenomenon, including the suppression of vortex shedding for moderate TSRs, and the short-wavelength corkscrew-shaped $(-2, 0, 1)$ principal mode from the family of elliptic instabilities, which form the basis of study in further chapters.

In Chapter 4, we explored the vortex-shedding-suppression phenomenon in greater detail, demonstrating that spin acts to reduce and/or suppress vortex-shedding instabilities over a broad range of Re and α. The mechanism behind this suppression relates to the vorticity generation at the spinning disk surface and how this vorticity convects into the wake. By analyzing the pattern of streamlines in wake, we show that the disk rotation produces a cone-shaped recirculation region that tilts into the advancing tip vortex and draws in fluid towards the disk surface. As a result, the vortex lines originating from the top disk surface align with the advancing tip vortex and add significantly to its strength. The vorticity from the pressure side of the disk

distributes itself more diffusely in both the receding tip vortex and the trailing-edge vortex. The increased circulation in the tip vortices induces a spanwise stretching of the trailing edge vortex sheet, helping to dissipate vorticity and prevent roll up, suppressing vortex shedding. Similar trends are observed in the wake of other spinning, axisymmetric bluff bodies, including the sphere (Kim and Choi, 2002; Kim, 2009), the bullet-shaped body (Jiménez-González et al., 2014), and the circular cylinder (Kang, Choi, and Lee, 1999; Mittal and Kumar, 2003). The similarity in changes in wake structure suggest that the strengthening of the tip vortices and spanwise vorticity dissipation may play a role across these different cases. This may serve to help predict wake changes in rotation of general axisymmetric bluff bodies.

Finally, in Chapter 5, we compare the distinct short-wavelength instability that appears at high TSRs to the $(-2, 0, 1)$ principal mode associated with elliptic instability. We perform SPOD to isolate the associated modes and compare them to characterizations of this principal mode studied in a pair of counter-rotating Batchelor vortices, demonstrating strong qualitative and quantitative agreement (Lacaze, Ryan, and Le Dizès, 2007). Principal modes of the elliptic instability are unstable when resonant conditions are met for sufficiently high circulation Reynolds number and strain. While this condition is not satisfied for non-spinning disks, increasing TSR, in contrast to Re or α, is uniquely able to modify the axial velocity strength in the advancing tip vortex, as a result of the upstream flow generated by the recirculation region. For a narrow range of TSRs, the frequency of the $(-2, 0, 1)$ principal mode locks in to twice the frequency of disk rotation, suggesting that the rotation acts as an additional forcing that helps to enhance the resonance of the elliptic instability. We also observe cases for higher TSRs where both vortex shedding and the $(-2, 0, 1)$ principal mode are apparent. SPOD shows that these modes lock-in to one another, with the hairpin-vortex shedding aligning with the braids of the short-wavelength instability.

While the observations in this thesis were made for low Reynolds number flow ($O(10^2)$) over a disk, we note that many trends are consistent with observations for high Reynolds number and for other bluff-body geometries.

The structure of vortex-shedding instabilities observed at low Reynolds numbers has been shown to persist statistically as large-scale coherent structures at turbulent Reynolds numbers, as seen for flow over the inclined disk for up to $Re = 5 \cdot 10^4$ (Calvert, 1967) and for the axisymmetric bluff body for up to $Re = 2 \cdot 10^5$ (Rigas et al., 2014).

Therefore, while we require further investigation at high Reynolds number to draw definitive conclusions, we speculate that the mechanisms uncovered here may offer some insight into the underlying flow physics for flow over different rotating bodies at high Reynolds number.

6.1 Future work

In this thesis, we focused primarily on characterizing and exploring mechanisms for vortex-shedding suppression and elliptic instability in flow over a spinning disk. However, there is still much to investigate in order to comprehensively understand and predict these instabilities throughout the large parameter space of spinning-disk flow. Below, we outline several ways to expand upon the present work.

Since disk rotation plays a key role in suppressing vortex shedding and creating the conditions for elliptic instability in the tip vortices, it would be beneficial to precisely quantify the convection of vorticity from the rotating disk into the wake. This would involve measuring the change in strength of the tip vortices and trailing-edge vortex sheet. In terms of vortex shedding, this could help to characterize the opposing effects of both the increased vorticity input and the increased spanwise dissipation of vorticity in the trailing-edge vortex sheet as TSR increases. This would shed light on the modulation of the flow from supercritical to subcritical and back to supercritical, which is relevant in a number of flow configurations featuring rotating bodies (Kim, 2009; Mittal and Kumar, 2003). In addition, spin affects values of axial velocity strength, circulation Reynolds number, and strain rate, which affect the stability of the elliptic-instability principal modes. If these changes could be quantified for different wake regimes, this would allow for a more accurate prediction of when elliptic instability occurs.

The observations made here hint at the presence of similar phenomenon at high Reynolds number. This thesis has focused on a relatively narrow range of Reynolds numbers and angles of attack close to the first (vortex-shedding) bifurcation. High-Reynolds-number studies could help to extend these results to MAV flight regimes. These studies could be done experimentally, which would comfortably reach $Re = 0(10^5)$. Experiments would allow for the added benefit of efficiently studying a range of disk profiles for flight applications. Alternatively, Dorschner et al. (2020) and Yu (2021) have expanded on the current IBLGF method with adaptive grid refinement and LES capabilities. These would allow for simulations at high Reynolds numbers as well. Increasing Reynolds number will undoubtedly affect the

separation characteristics and wake structures, especially in turbulent regimes. One might consider whether disk spin will still affect the axial velocity in the tip vortices at high Reynolds numbers where the recirculation region will change significantly. Reynolds number (and angle of attack) will ultimately affect the strength of both the trailing-edge vortex sheet and the tip vortices, which are key factors in the appearance of the various instabilities discussed.

The flow topology, and therefore the effect of spin, are a function of the disk geometry. The changing wake structure with disk geometry parameters such as aspect ratio, camber and edge shape is still largely unstudied. Investigating these effects are necessary to understand how vorticity generated by disk rotation will convect into the wake. Since the disk's thickness or aspect ratio can effect the bifurcations, it may also be worthwhile to estimate the effect of the apparent thickness from the finite regularization when using the immersed boundary method (see section 2.3.5). One way to do this would be to study a laminar boundary layer developing over a flat plate modelled using immersed boundary points. Carefully comparing the resulting flow field to the Blasius boundary layer solution could help to quantify the apparent thickness of the immersed boundary surface for a given resolution and highlight any other ways that the immersed boundary support effects the thickness. Clearly, there remains a large parameter space to explore as a fundamental step towards being able to quantify and predict wake parameters as a function of spin. Such developments would be vital for optimal spinning-disk flight design.

Extending the stability analysis and numerical simulations performed by Lacaze, Ryan, and Le Dizès (2007) to cover $W_0 \geq 0.6$ would allow for an improved comparison with the present work and would provide a more accurate picture of which principal modes of the elliptic instability are unstable for high W_0. However, this would still be limited due to discrepancies from the ideal Batchelor vortex configuration. Ideally, it would also be important to consider and model the effect of the disk rotation and/or the nearby trailing-edge vortex sheet, as these change the structure of the base flow significantly. While it may prove challenging to model these effects, it is possible that the effect of the trailing-edge vortex sheet could be captured by incorporating its effect in the strain field appropriately, instead of assuming the strain field from a single adjacent vortex. As it stands, our comparison is indirect and relies on the robustness of the mode shapes and resonance characteristics, which compare well despite the discrepancy in W_0. A more accurate assessment of the growth rates

of the elliptic instability in the absence of the disk rotation would shed light on the lock-in phenomenon and help us understand the degree to which rotation can enhance the resonance of the modes and modify the elliptic-instability frequency.

We can also look beyond spinning-disk flight and consider a mounted spinning disk as an actuator for flow control. We have already seen how spin injects linear and angular momentum into the wake, modifying the wake structure significantly. Ricco and Hahn (2013) demonstrated that rotating wall-flush-mounted disks could reduce drag in channel flow. Wise, Alvarenga, and Ricco (2014) and Olivucci, Ricco, and Aghdam (2019) studied a similar configuration using rotating rings instead of disks, which are able to achieve similar drag reduction levels via a similar mechanism, while using less power. Similarly, Munday and Taira (2018) studied swirling jet actuators on an airfoil and found that the injection of wall-normal and angular momentum helped to control separation. The spinning disk could offer similar applications for wings where zero net mass flux is required. This could open up the possibility of using small rotating-disk actuators in an overall fixed-wing configuration.

The future work proposed above all tie in to ultimately being able to quantify and predict how the vorticity produced by the spinning disk convects into the wake and influences the flow regimes. The present work is only the start of a more comprehensive understanding of the complex wake structure for flow over a spinning disk at angle of attack.

BIBLIOGRAPHY

Auguste, F., Fabre, D., and Magnaudet, J. (2010). "Bifurcations in the wake of a thick circular disk". In: *Theoretical and Computational Fluid Dynamics* 24.1-4 (2010), pp. 305–313.

aus der Wiesche, S. (2002). "Heat transfer and thermal behaviour of a rotating disk passed by a planar air stream". In: *Forschung im Ingenieurwesen* 67.4 (2002), pp. 161–174.

Batchelor, G. (1964). "Axial flow in trailing line vortices". In: *Journal of Fluid Mechanics* 20.4 (1964), pp. 645–658.

Calvert, J. (1967). "Experiments on the flow past an inclined disk". In: *Journal of Fluid Mechanics* 29.4 (1967), pp. 691–703.

Chrust, M., Dauteuille, C., Bobinski, T., Rokicki, J., Goujon-Durand, S., Wesfreid, J., Bouchet, G., and Dušek, J. (2015). "Effect of inclination on the transition scenario in the wake of fixed disks and flat cylinders". In: *Journal of Fluid Mechanics* 770 (2015), pp. 189–209.

Chrust, M., Bouchet, G., and Dusek, J. (2010). "Parametric study of the transition in the wake of oblate spheroids and flat cylinders". In: *Journal of Fluid Mechanics* 665 (2010), p. 199.

Cochran, W. (1934). "The flow due to a rotating disc". In: *Mathematical Proceedings of the Cambridge Philosophical Society*. Vol. 30. 3. Cambridge University Press. 1934, pp. 365–375.

Crow, S. C. (1970). "Stability theory for a pair of trailing vortices". In: *AIAA Journal* 8.12 (1970), pp. 2172–2179.

Dorschner, B., Yu, K., Mengaldo, G., and Colonius, T. (2020). "A fast multi-resolution lattice Green's function method for elliptic difference equations". In: *Journal of Computational Physics* 407 (2020), p. 109270.

Eloy, C. and Le Dizès, S. (2001). "Stability of the Rankine vortex in a multipolar strain field". In: *Physics of Fluids* 13.3 (2001), pp. 660–676.

Gao, S., Tao, L., Tian, X., and Yang, J. (2018). "Flow around an inclined circular disk". In: *Journal of Fluid Mechanics* 851 (2018), pp. 687–714.

Ghaddar, N., Korczak, K., Mikic, B., and Patera, A. (1986). "Numerical investigation of incompressible flow in grooved channels. Part 1. Stability and self-sustained oscillations". In: *Journal of Fluid Mechanics* 163 (1986), pp. 99–127.

Goza, A. and Colonius, T. (2017). "A strongly-coupled immersed-boundary formulation for thin elastic structures". In: *Journal of Computational Physics* 336 (2017), pp. 401–411.

Higuchi, H., Goto, Y., Hiramoto, R., and Meisel, I. (2000). "Rotating flying disks and formation of trailing vortices". In: *18th AIAA Applied Aerodynamics Conference*. 2000, p. 4001.

Hubbard, M. and Hummel, S. (2000). "Simulation of Frisbee flight". In: *5th Conference on Mathematics and Computers in Sport, University of Technology, Sydney*. 2000, pp. 124–134.

Hummel, S. A. (2003). *Frisbee flight simulation and throw biomechanics*. University of California, Davis, 2003.

Humphries, W. and Vincent, J. (1976). "Near wake properties of axisymmetric bluff body flows". In: *Applied Scientific Research* 32.6 (1976), pp. 649–669.

Jiménez-González, J. I., Sevilla, A., Sanmiguel-Rojas, E., and Martínez-Bazán, C. (2014). "Global stability analysis of the axisymmetric wake past a spinning bullet-shaped body". In: *Journal of Fluid Mechanics* 748 (2014), pp. 302–327.

Kallemov, B., Bhalla, A., Griffith, B., and Donev, A. (2016). "An immersed boundary method for rigid bodies". In: *Communications in Applied Mathematics and Computational Science* 11.1 (2016), pp. 79–141.

Kang, S., Choi, H., and Lee, S. (1999). "Laminar flow past a rotating circular cylinder". In: *Physics of Fluids* 11.11 (1999), pp. 3312–3321.

Karabelas, S., Koumroglou, B., Argyropoulos, C., and Markatos, N. (2012). "High Reynolds number turbulent flow past a rotating cylinder". In: *Applied Mathematical Modelling* 36.1 (2012), pp. 379–398. ISSN: 0307-904X. DOI: https://doi.org/10.1016/j.apm.2011.07.032.

Keefe, L. (1997). "A normal vorticity actuator for near-wall modification of turbulent shear flows". In: *35th Aerospace Sciences Meeting and Exhibit*. 1997, p. 547.

Keefe, L. R. (1998). "Method and apparatus for reducing the drag of flows over surfaces". US Patent 5,803,409. Sept. 1998.

Kerswell, R. R. (2002). "Elliptical instability". In: *Annual Review of Fluid Mechanics* 34.1 (2002), pp. 83–113.

Kim, D. (2009). "Laminar flow past a sphere rotating in the transverse direction". In: *Journal of Mechanical Science and Technology* 23.2 (2009), pp. 578–589.

Kim, D. and Choi, H. (2002). "Laminar flow past a sphere rotating in the streamwise direction". In: *Journal of Fluid Mechanics* 461 (2002), pp. 365–386.

Lacaze, L., Birbaud, A.-L., and Le Dizès, S. (2005). "Elliptic instability in a Rankine vortex with axial flow". In: *Physics of Fluids* 17.1 (2005), pp. 017101–017101.

Lacaze, L., Ryan, K., and Le Dizès, S. (2007). "Elliptic instability in a strained Batchelor vortex". In: *Journal of Fluid Mechanics* 577 (2007), pp. 341–361.

Leweke, T., Le Dizès, S., and Williamson, C. H. (2016). "Dynamics and instabilities of vortex pairs". In: *Annual Review of Fluid Mechanics* 48 (2016), pp. 507–541.

Liska, S. and Colonius, T. (2014). "A parallel fast multipole method for elliptic difference equations". In: *Journal of Computational Physics* 278 (2014), pp. 76–91.

– (2016). "A fast lattice Green's function method for solving viscous incompressible flows on unbounded domains". In: *Journal of Computational Physics* 316 (2016), pp. 360–384.

– (2017). "A fast immersed boundary method for external incompressible viscous flows using lattice Green's functions". In: *Journal of Computational Physics* 331 (2017), pp. 257–279.

Lorenz, R. D. (2007). *Spinning flight: dynamics of frisbees, boomerangs, samaras, and skipping stones*. Springer Science & Business Media, 2007.

Meliga, P., Chomaz, J.-M., and Sipp, D. (2009). "Global mode interaction and pattern selection in the wake of a disk: A weakly nonlinear expansion". In: *Journal of Fluid Mechanics* 633 (2009), pp. 159–189.

Mittal, S. and Kumar, B. (2003). "Flow past a rotating cylinder". In: *Journal of Fluid Mechanics* 476 (2003), pp. 303–334.

Munday, P. M. and Taira, K. (2018). "Effects of wall-normal and angular momentum injections in airfoil separation control". In: *AIAA Journal* 56.5 (2018), pp. 1830–1842.

Nakamura, Y. and Fukamachi, N. (1991). "Visualization of the flow past a Frisbee". In: *Fluid Dynamics Research* 7.1 (1991), p. 31.

Olivucci, P., Ricco, P., and Aghdam, S. K. (2019). "Turbulent drag reduction by rotating rings and wall-distributed actuation". In: *Physical Review Fluids* 4.9 (2019), p. 093904.

Pereira, J. and Sousa, J. (1993). "Finite volume calculations of self-sustained oscillations in a grooved channel". In: *Journal of Computational Physics* 106.1 (1993), pp. 19–29.

Persson, P.-O. and Strang, G. (2004). "A simple mesh generator in MATLAB". In: *SIAM review* 46.2 (2004), pp. 329–345.

Pier, B. (2013). "Periodic and quasiperiodic vortex shedding in the wake of a rotating sphere". In: *Journal of Fluids and Structures* 41 (2013), pp. 43–50.

Pines, D. J. and Bohorquez, F. (2006). "Challenges facing future micro-air-vehicle development". In: *Journal of Aircraft* 43.2 (2006), pp. 290–305.

Poon, E. K., Ooi, A. S., Giacobello, M., and Cohen, R. C. (2010). "Laminar flow structures from a rotating sphere: Effect of rotating axis angle". In: *International Journal of Heat and Fluid Flow* 31.5 (2010), pp. 961–972.

Potts, J. and Crowther, W. (2001). "Flight control of a spin stabilised axi-symmetric disc-wing". In: *39th AIAA Aerospace Sciences Meeting and Exhibit*. 2001, p. 253.

Potts, J. and Crowther, W. (2002). “Frisbee (TM) aerodynamics”. In: *20th AIAA Applied Aerodynamics Conference*. 2002, p. 3150.

Potts, J. R. (2005). “Disc-wing aerodynamics”. PhD thesis. University of Manchester, 2005.

Ricco, P. and Hahn, S. (2013). “Turbulent drag reduction through rotating discs”. In: *Journal of Fluid Mechanics* 722 (2013), pp. 267–290.

Rigas, G., Oxlade, A., Morgans, A., and Morrison, J. (2014). “Low-dimensional dynamics of a turbulent axisymmetric wake”. In: *Journal of Fluid Mechanics* 755 (2014).

Roma, A. M., Peskin, C. S., and Berger, M. J. (1999). “An adaptive version of the immersed boundary method”. In: *Journal of Computational Physics* 153.2 (1999), pp. 509–534.

Ryan, K., Butler, C. J., and Sheard, G. J. (2012). “Stability characteristics of a counter-rotating unequal-strength Batchelor vortex pair”. In: *Journal of Fluid Mechanics* 696 (2012), pp. 374–401.

Ryan, K. and Sheard, G. (2007). “Non-linear growth of short-wave instabilities in a Batchelor vortex pair”. In: *16th Australasian Fluid Mechanics Conference*. School of Engineering, The University of Queensland, Brisbane, 2007.

Schmidt, O. T. and Towne, A. (2019). “An efficient streaming algorithm for spectral proper orthogonal decomposition”. In: *Computer Physics Communications* 237 (2019), pp. 98–109.

Stilley, G. and Carstens, D. (1972). “Adaptation of the Frisbee flight principle to delivery of special ordnance”. In: *2nd Atmospheric Flight Mechanics Conference*. 1972, p. 982.

Taira, K. and Colonius, T. (2009). “Three-dimensional flows around low-aspect-ratio flat-plate wings at low Reynolds numbers”. In: *Journal of Fluid Mechanics* 623 (2009), pp. 187–207.

Taira, K., Dickson, W., Colonius, T., Dickinson, M., and Rowley, C. (2007). “Unsteadiness in flow over a flat plate at angle-of-attack at low Reynolds numbers”. In: *45th AIAA Aerospace Sciences Meeting and Exhibit*. 2007, p. 710.

Thomson, W. (1880). “XXIV. Vibrations of a columnar vortex”. In: *The London, Edinburgh, and Dublin Philosophical Magazine and Journal of Science* 10.61 (1880), pp. 155–168.

Tian, X., Hu, Z., Lu, H., and Yang, J. (2017). “Direct numerical simulations on the flow past an inclined circular disk”. In: *Journal of Fluids and Structures* 72 (2017), pp. 152–168.

Towne, A., Schmidt, O. T., and Colonius, T. (2018). “Spectral proper orthogonal decomposition and its relationship to dynamic mode decomposition and resolvent analysis”. In: *Journal of Fluid Mechanics* 847 (2018), pp. 821–867.

Towns, J., Cockerill, T., Dahan, M., Foster, I., Gaither, K., Grimshaw, A., Hazlewood, V., Lathrop, S., Lifka, D., Peterson, G. D., Roskies, R., Scott, J., and Wilkins-Diehr, N. (2014). "XSEDE: Accelerating Scientific Discovery". In: *Computing in Science & Engineering* 16.05 (Sept. 2014), pp. 62–74. ISSN: 1558-366X. DOI: 10.1109/MCSE.2014.80.

von Kármán, T. (1921). "Über laminare und turbulente Reibung". In: *ZAMM-Journal of Applied Mathematics and Mechanics/Zeitschrift für Angewandte Mathematik und Mechanik* 1.4 (1921), pp. 233–252.

Widnall, S. E., Bliss, D. B., and Tsai, C.-Y. (1974). "The instability of short waves on a vortex ring". In: *Journal of Fluid Mechanics* 66.1 (1974), pp. 35–47.

Wise, D. J., Alvarenga, C., and Ricco, P. (2014). "Spinning out of control: Wall turbulence over rotating discs". In: *Physics of Fluids* 26.12 (2014), p. 125107.

Yang, X., Zhang, X., Li, Z., and He, G.-W. (2009). "A smoothing technique for discrete delta functions with application to immersed boundary method in moving boundary simulations". In: *Journal of Computational Physics* 228.20 (2009), pp. 7821–7836. ISSN: 0021-9991. DOI: https://doi.org/10.1016/j.jcp.2009.07.023.

Yasuda, K. (1999). "Flight and aerodynamic characteristics of a flying disk". In: *Journal of the Japan Society for Aeronautical and Space Sciences* 47.547 (1999), pp. 16–22.

Yu, K. (2021). "Multi-resolution Lattice Green's Function Method for High Reynolds Number External Flows". PhD thesis. California Institute of Technology, 2021.

Appendix A

IMMERSED BOUNDARY MESH FOR THE DISK

Figure A.1 shows the mesh used for the disk simulations at $Re = 500$. The mesh is generated by Distmesh (Persson and Strang, 2004). The vertices indicate the location of IB points. Measuring the length of the connective edges gives the IB spacing. This mesh has a total of 2585 points.

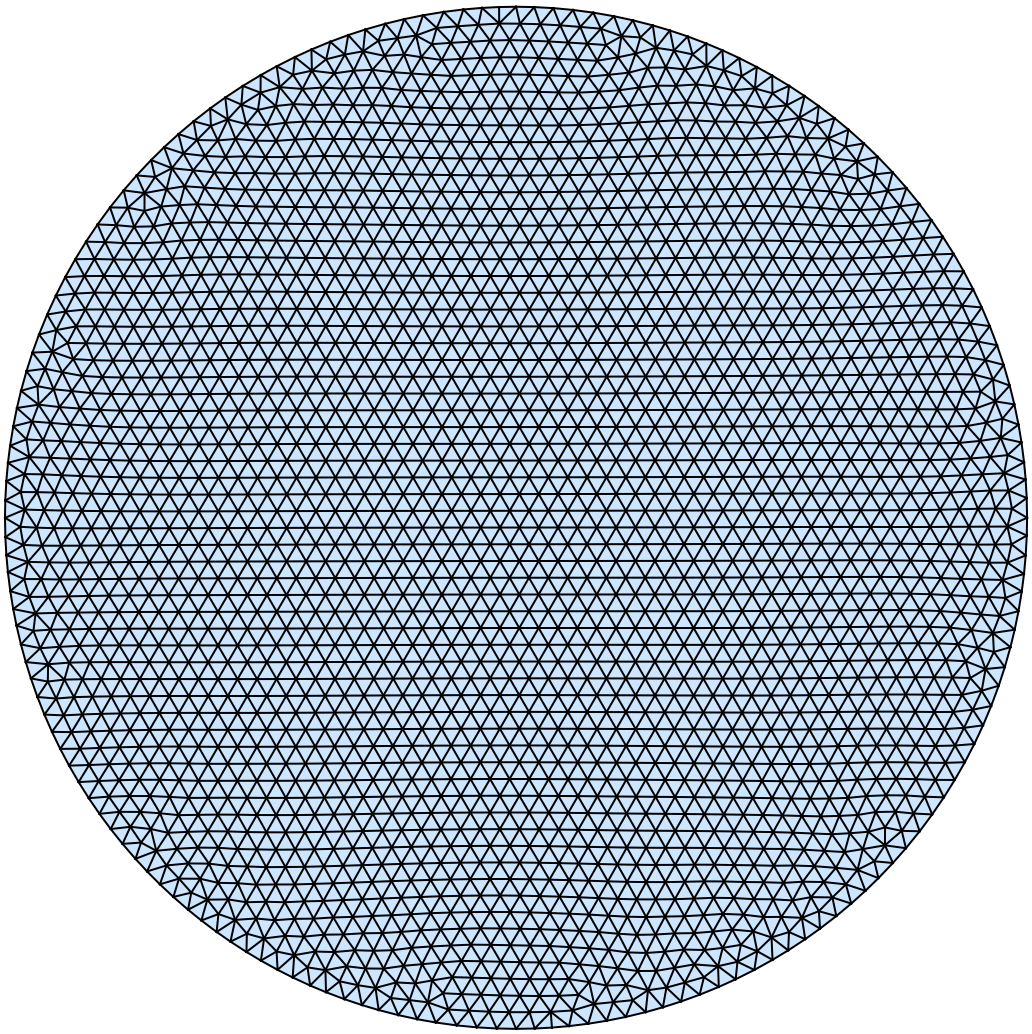

Figure A.1: Mesh used for disk immersed surface with $\overline{\Delta s} = 0.1875$, generated by Distmesh (Persson and Strang, 2004). Immersed boundary points are located at vertices while the edges represent the distance between IB points.

Appendix B

NON-SPINNING DISK AERODYNAMICS AND FLOW REGIMES

The lift and drag time series are shown for various α in figure B.1, while the corresponding wake visualization shown with isosurfaces of vorticity magnitude are shown in figure B.2. The angle of attack serves as a bifurcation parameter. For low α, the flow is steady and develops two tip vortices on either side of the disk. As angle of attack is increased to $\alpha = 30^{\circ}$, the flow undergoes a supercritical Hopf bifurcation and transitions to a periodic vortex shedding flow. At $\alpha = 40$, the flow is quasi-periodic with a low frequency modulation. The amplitude of lift and drag oscillation changes regularly, corresponding to a strengthening and weakening of the vortex shedding B.3. For even higher angle of attack, the flow becomes chaotic and loses its spanwise symmetry, shown visually and also by the non-zero side force that develops. These flow regimes have been characterized extensively by Tian et al. (2017).

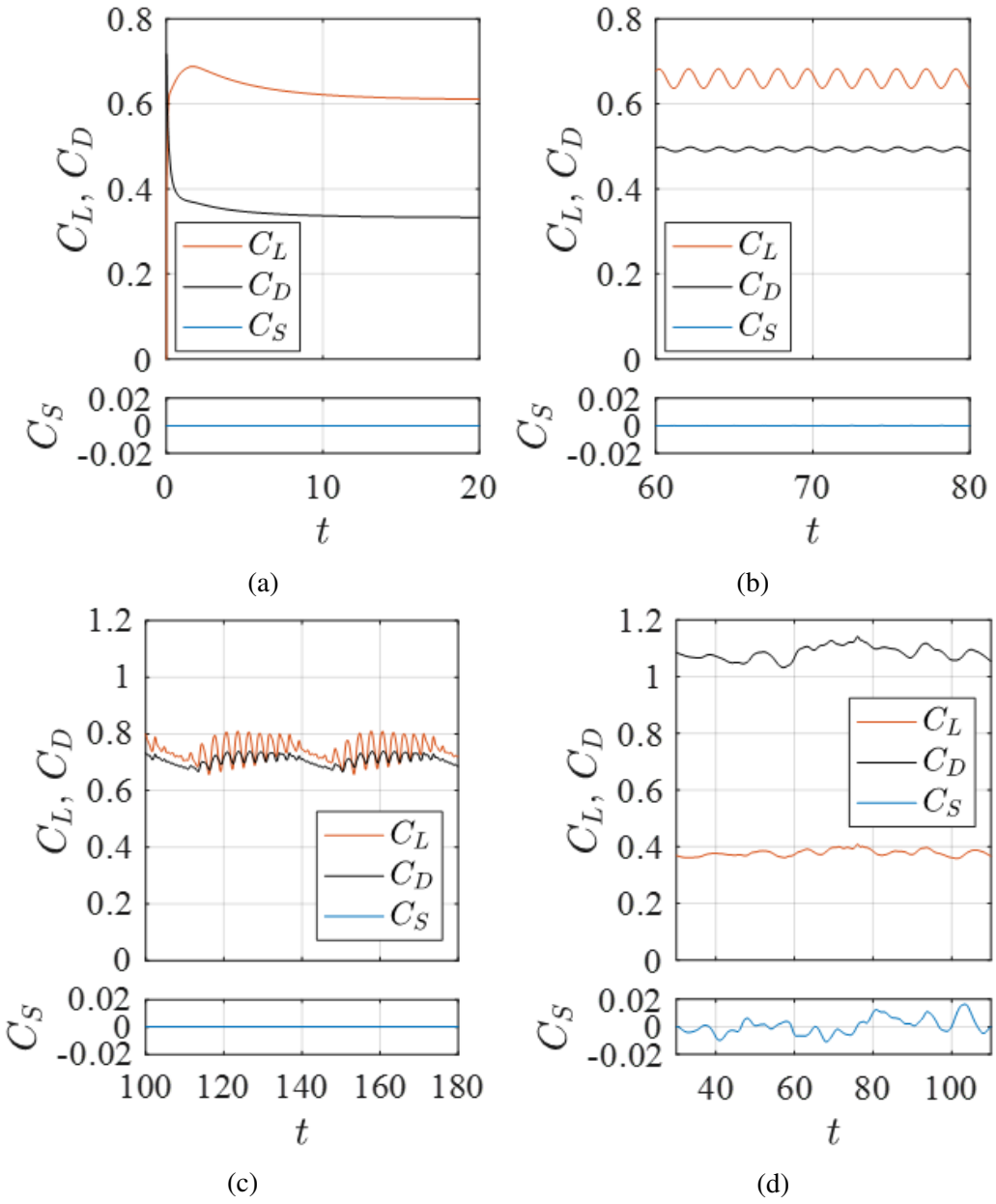

Figure B.1: Lift, drag and side force coefficients over time for the non-spinning disk at $Re = 500$ for (a) $\alpha = 20^{\circ}$, (b) $\alpha = 30^{\circ}$, (c) $\alpha = 40^{\circ}$, and (d) $\alpha = 70^{\circ}$.

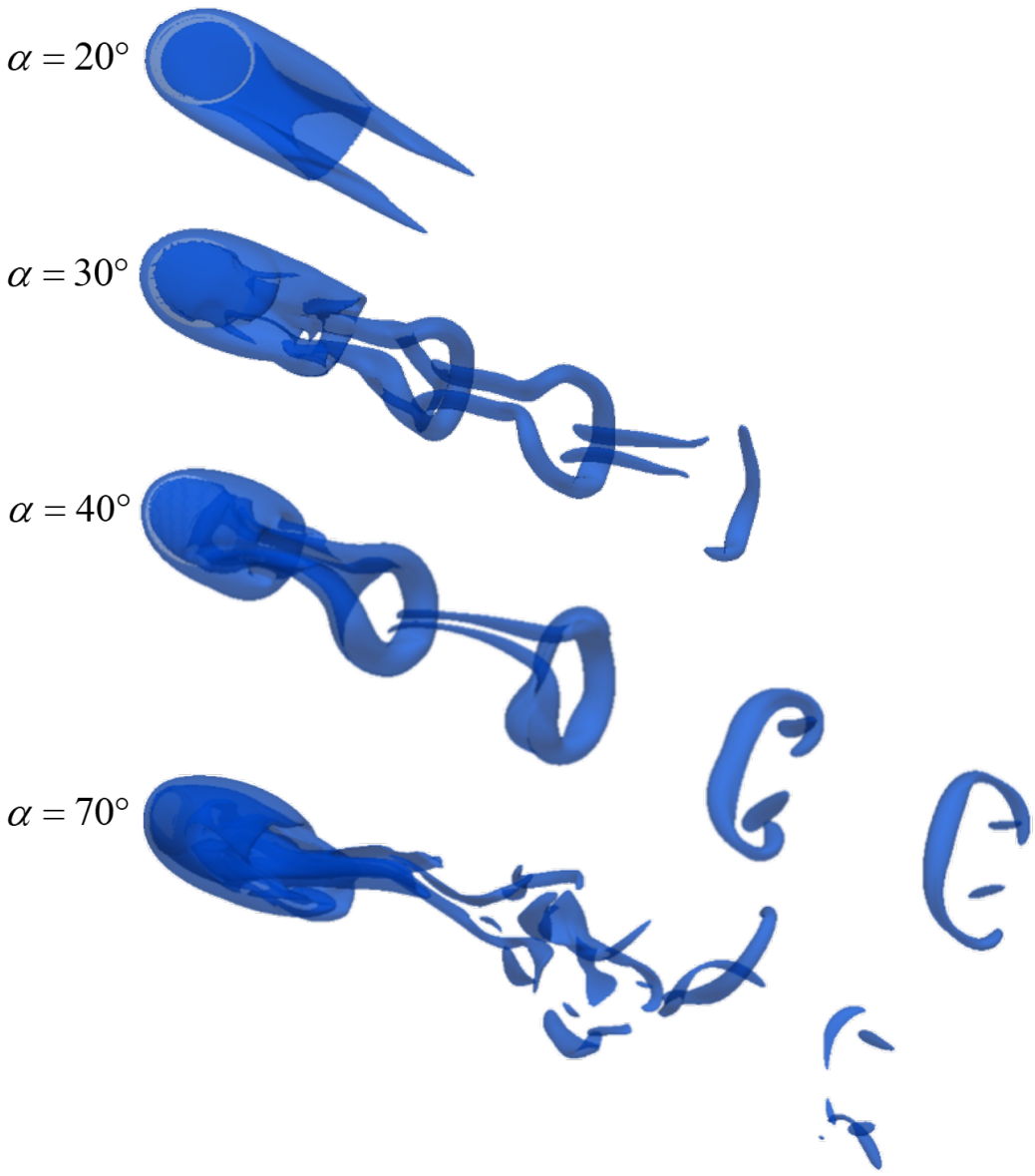

Figure B.2: Isosurfaces of vorticity magnitude ($|\omega|$ = 3 for the non-spinning disk at Re = 500 at various angles of attack.

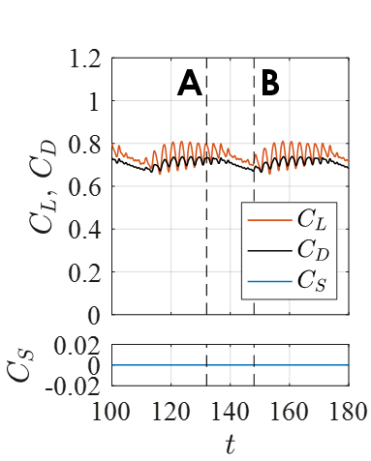

(a)

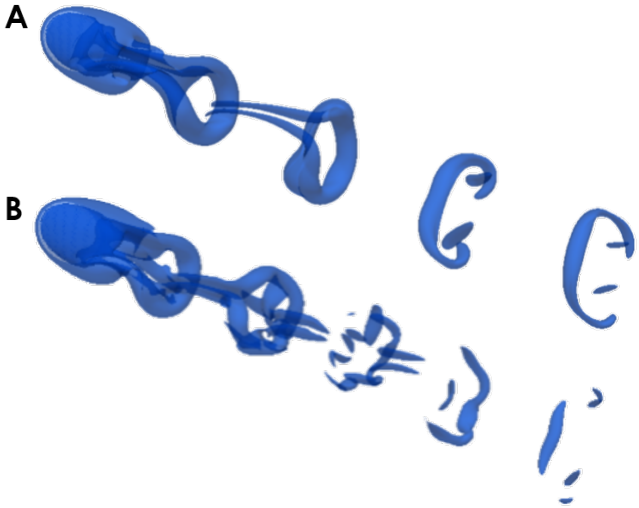

(b)

Figure B.3: (a) Time-varying force coefficients and (b) isosurfaces of vorticity magnitude ($|\omega| = 3$) for the non-spinning disk flow with periodic vortex shedding with a low frequency modulation, occurring at $Re = 500$ and $\alpha = 40°$. The two isosurface images correspond to (A) strengthened vortex-shedding and (B) weakened vortex-shedding, as marked on the time series plots.

Appendix C

VORTEX LINES FOR FLOW PARALLEL TO THE DISK

Because of the complexity of vortex line distribution in wakes, we provide some additional visualizations to help the reader understand how the arrangement of vortex lines change when spin is introduced. Figures C.1 and C.2 compare vortex lines from different parts of the disk for the spinning disk with and without streamwise flow. For the spinning disk without streamwise flow, vortex lines are axissymetric. Vortex lines start on one side of the disk, loop out and around back to the opposite side of the disk. Vortex lines starting closer to the center of the disk form larger loops than those started close to the disk edge.

When streamwise flow is added, the vortex lines tend near the leading edge are compressed, while those towards the trailing edge are stretched downstream. Those on the advancing side of the disk concentrate into a vortical structure on the advancing side, which contains negative streamwise vorticity. The vortical structure with positive streamwise vorticity on the receding side is more diffused.

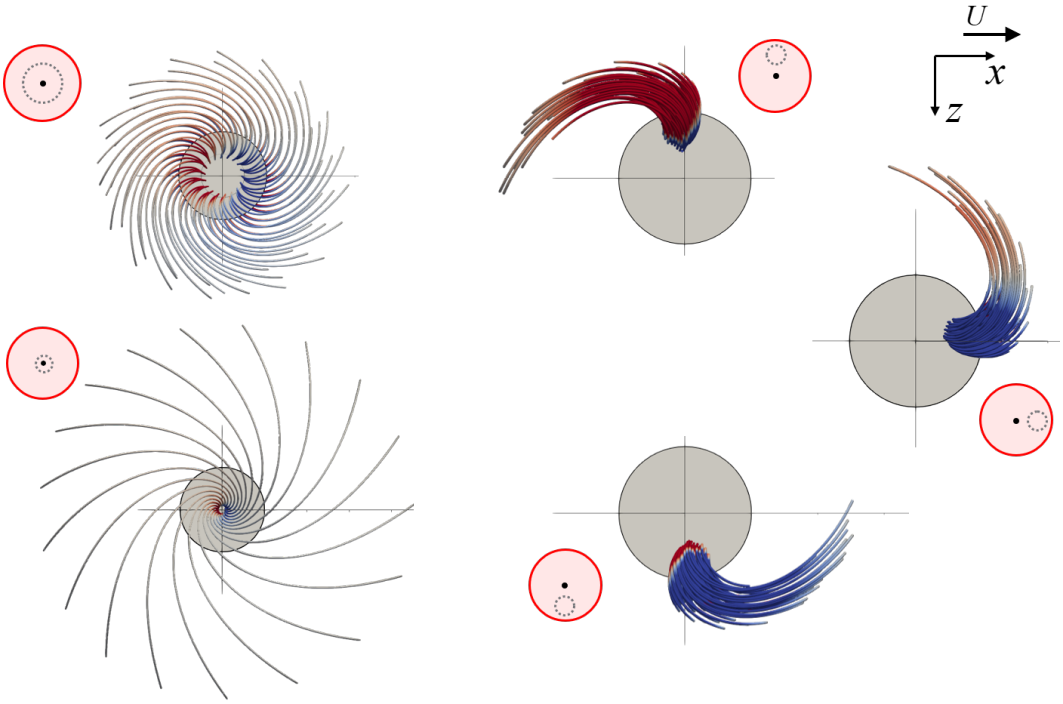

Figure C.1: Top view of various groups of vortex lines initialized in rings on the disk surface for $Re_\omega = 100$. Vortex lines are colored by streamwise vorticity, red for positive and blue for negative.

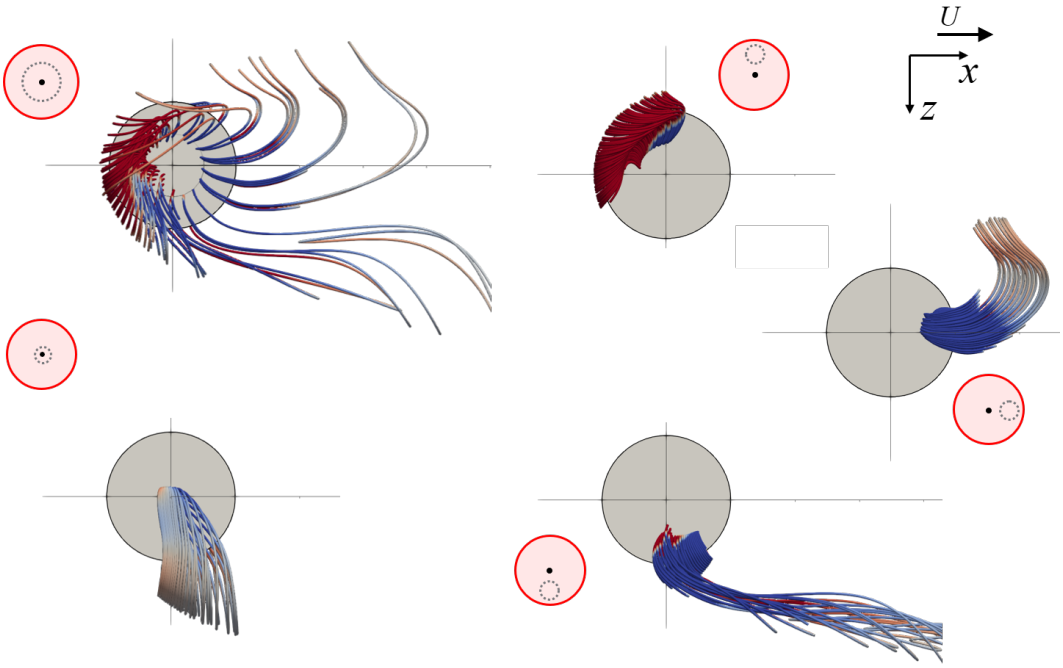

Figure C.2: Top view of various groups of vortex lines initialized in rings on the disk surface for $Re = 100$, $Re_\omega = 400$ (or $\lambda = 4$) and $\alpha = 0^\circ$. Flow is in the $+x$ direction and disk rotation is clockwise. Vortex lines are colored by streamwise vorticity, red for positive and blue for negative